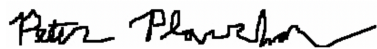


RETRIEVAL AND APPLICATIONS OF PRECISE RADIAL VELOCITIES  
TO DETECT EXOPLANETS

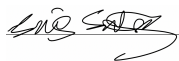
by

Bryson Cale  
A Dissertation  
Submitted to the  
Graduate Faculty  
of  
George Mason University  
in Partial Fulfillment of  
The Requirements for the Degree  
of  
Doctor of Philosophy  
Physics

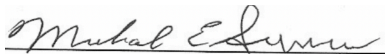
Committee:



Dr. Peter Plavchan, Committee Chair



Dr. Shobita Satyapal, Committee Member



Dr. Michael Summers, Committee  
Member



Dr. Angelle Tanner, Committee Member



Dr. Paul So, Department Chairperson



Dr. Donna M. Fox, Associate Dean,  
Office of Student Affairs & Special  
Programs, College of Science



Dr. Fernando R. Miralles-Wilhelm, Dean,  
College of Science

Date: July 6, 2021

Summer Term 2021  
George Mason University  
Fairfax, VA

Retrieval and Applications of Precise Radial Velocities to Detect Exoplanets

A dissertation submitted in partial fulfillment of the requirements for the degree of  
Doctor of Philosophy at George Mason University

By

Bryson L. Cale  
Bachelor of Arts  
Grinnell College, 2012

Director: Dr. Peter Plavchan, Professor  
Department of Physics and Astronomy

Summer Term 2021  
George Mason University  
Fairfax, VA



Copyright © 2021 by Bryson L. Cale  
All Rights Reserved

## Acknowledgments

I would like to thank my entire dissertation committee and committee chair, Dr. Peter Plavchan, for providing comments and guiding me through the research and writing process.

I would also like to thank several collaborators who mentored me over the course of my Ph.D., including Dr. Jonathan Gagné, Dr. Peter Gao, Dr. Angelle Tanner, Dr. Charles Beichman, Dr. Johanna Teske, and Dr. Sharon Wang.

I would like to thank all of the undergraduate and graduate students who aided me with my research.

All data processed with `pyche11` (iSHELL & CHIRON) were run on ARGO, a research computing cluster provided by the Office of Research Computing, and the exo computer cluster, both at George Mason University, VA.

I would like to thank all support astronomers, observers, and engineers from all astronomical facilities in helping enable the collection of the data presented in this thesis.

I wish to recognize and acknowledge the very significant cultural role and reverence that the summit of Maunakea has always had within the indigenous Hawaiian community, where many of the observations presented in this thesis were recorded. I am most fortunate to have the opportunity to conduct observations from this mountain.

The authors also wish to thank the California Planet Search (CPS) collaboration in particular for carrying out the HIRES observations of AU Mic recorded in 2020 and presented in this thesis.

This thesis includes data collected by the NASA *TESS* mission that are publicly available from the Mikulski Archive for Space Telescopes (MAST). Funding for the *TESS* mission is provided by NASA's Science Mission Directorate. We acknowledge the use of public *TESS* data from pipelines at the *TESS* Science Office and at the TESS Science Processing Operations Center (1).

# Table of Contents

	Page
List of Tables . . . . .	vi
List of Figures . . . . .	viii
Abstract . . . . .	xiii
1 Introduction . . . . .	1
1.1 The Radial Velocity Technique . . . . .	1
1.2 History, Success, & Limitations . . . . .	2
1.2.1 Instrumental Calibration . . . . .	2
1.2.2 Telluric Contamination . . . . .	2
1.2.3 Not All Stars Are Created Equal . . . . .	3
1.2.4 Wavelength of the Observations . . . . .	4
1.3 This Work . . . . .	5
2 Process and Analysis of Echelle Spectra with . . . . .	6
2.1 Echelle Gratings . . . . .	7
2.2 Observations with iSHELL . . . . .	8
2.3 Spectral Reduction . . . . .	13
2.3.1 Order Tracing . . . . .	14
2.3.2 Flat-field Artifacts . . . . .	14
2.3.3 Spectral Extraction . . . . .	16
2.4 Measuring Radial Velocities . . . . .	21
2.4.1 Choice of Numerical Solver . . . . .	21
2.4.2 Spectral Forward Model . . . . .	22
2.4.3 Stellar Template Retrieval . . . . .	27
2.4.4 RV Calculations . . . . .	29
2.4.5 Weighted Statistics . . . . .	30
2.4.6 Detrending Minimization . . . . .	31
2.5 Results . . . . .	34
2.5.1 RVs . . . . .	35
2.5.2 Error Analysis . . . . .	42
2.5.3 Stellar Template Generation . . . . .	45

2.5.4	Model Parameters . . . . .	53
2.6	Discussion . . . . .	59
2.6.1	Wavelength Solution . . . . .	59
2.6.2	LSF Model . . . . .	64
2.6.3	Other NIR Precise RV Instruments & Methodologies . . . . .	65
2.6.4	Prospects for iSHELL Planet Confirmation . . . . .	66
2.7	Summary & Future Improvements . . . . .	67
3	Chromatic Radial Velocities of the Young AU Mic Planetary System . . . . .	68
3.1	Introduction . . . . .	68
3.2	Observations . . . . .	70
3.2.1	RVs . . . . .	70
3.2.2	Photometry from <i>TESS</i> . . . . .	74
3.3	Radial Velocity Fitting . . . . .	75
3.3.1	Bayesian Inference for Radial-Velocities . . . . .	75
3.3.2	Two Chromatic Gaussian Processes . . . . .	75
3.3.3	Primary RV Analyses . . . . .	77
3.4	Results . . . . .	87
3.4.1	Evidence For Additional Candidates? . . . . .	89
3.5	Discussion . . . . .	96
3.5.1	Constraints on Eccentricity . . . . .	96
3.5.2	Sensitivity to Kernel Hyperparameters . . . . .	96
3.5.3	Planet Injection and Recovery . . . . .	97
3.5.4	Utility of RV-Color . . . . .	100
3.5.5	Additional Caveats and Future Work . . . . .	102
3.6	Conclusion . . . . .	104
A	Appendix 1 . . . . .	105
B	Appendix 2 . . . . .	106
C	Appendix 3 . . . . .	112
D	Appendix 4 . . . . .	130
	Bibliography . . . . .	134

## List of Tables

Table		Page
2.1	Summary of Observed Targets. . . . .	10
2.2	The obtained $S/N$ per detector pixel for all iSHELL observations. . . . .	11
2.3	Table 2.2 continued. . . . .	12
2.4	A summary of the spectral forward model parameters used to compute precise RVs from the iSHELL spectrograph. . . . .	26
2.5	The best single-order long-term RV precisions (unweighted standard deviation) for each of the four runs, and the corresponding best iteration. We only include the first 10 nights for 61 Cyg A in the calculation. . . . .	38
2.6	The best multi-order RVs for each target obtained through a powerset. The unweighted standard deviation $\sigma$ and value of $\chi^2_{red}$ of the measurements is noted. . . . .	39
3.1	A summary of the RV datasets used in this work. The nightly-binned measurements are provided in appendix C. $N_{tot}$ and $N_{nights}$ refers to the number of individual and per-night epochs, respectively. The median intrinsic error bars $\sigma_{RV}$ consider all observations. . . . .	74
3.2	The model parameters and prior distributions used in our primary fitting routines. $\blacksquare$ indicates the parameter is fixed. Parameters with multiple priors are We run models utilizing $\mathbf{K}_{J1}$ and $\mathbf{K}_{J2}$ . We list the radii of AU Mic b and c measured in M20 which we use to compute the corresponding densities of each planet. . . . .	87
3.3	The best-fit parameters and corresponding Keplerian variables for our primary two-planet fits using joint-kernels $\mathbf{K}_{J1}$ (eq. 3.2) and $\mathbf{K}_{J2}$ (eq. 3.3). The MCMC values correspond to the 15.9 <sup>th</sup> , 50 <sup>th</sup> , and 84.1 <sup>th</sup> percentiles. Planet masses, densities, and semi-major axes are computed by propagating the appropriate MCMC chains. We also add in quadrature the uncertainties in $M_\star$ and planetary radii from Table 3.2 where relevant. . . . .	90

3.4	Here we report the reduced chi-squared for each spectrograph from our nominal two-planet model using kernel $\mathbf{K}_{\mathbf{J1}}$ . Unlike when using quasi-disjoint kernels (Section 3.3.3), we find the model is overall significantly under-fit with the disjoint kernel. We suspect this is primarily due to an inadequate stellar-activity (i.e., a scaling relation is insufficient between spectrographs) and/or the exclusion of per-spectrograph jitter terms, and discuss these details further in Section 3.5.5. . . . .	91
3.5	Model information criterion for AU Mic b and c using kernel $\mathbf{K}_{\mathbf{J1}}$ (eq. 3.2) to model the stellar activity. . . . .	95
3.6	MCMC results with different assumptions for the mean spot lifetime $\eta_\tau$ and $\eta_\ell$ using kernel $\mathbf{K}_{\mathbf{J1}}$ (eq. 3.2). For each row, we fix the values of $\eta_\tau$ and $\eta_\ell$ . All other model parameters take on the initial values and priors from Table 3.2 for a two-planet model. We perform a MAP fit followed by MCMC sampling for each case. We report the nominal values and uncertainties for the semi-amplitudes of AU Mic b and c from the MCMC fitting, as well as the reduced chi-square statistic, $\chi^2_{red}$ using the MAP-derived parameters. Uncertainties reported here for $K_b$ and $K_c$ are the average of the upper and lower uncertainties. . . . .	98
C.1	Nightly HARPS RVs analyzed in this work. . . . .	112
C.2	Nightly HIRES RVs analyzed in this work. . . . .	113
C.3	Nightly NIRSPEC RVs analyzed in this work. . . . .	115
C.4	Nightly CSHELL RVs analyzed in this work. . . . .	116
C.5	Nightly TRES RVs analyzed in this work. . . . .	117
C.6	Nightly iSHELL RVs analyzed in this work. . . . .	120
C.7	Nightly IRD RVs analyzed in this work. . . . .	121
C.8	Nightly CARMENES-NIR RVs analyzed in this work. . . . .	122
C.9	Nightly CARMENES-Vis RVs analyzed in this work. . . . .	124
C.10	Nightly MINERVA-Australis RVs analyzed in this work. . . . .	126
C.11	Nightly CHIRON RVs analyzed in this work. . . . .	127
C.12	Nightly SPIRou RVs analyzed in this work. . . . .	128

## List of Figures

Figure	Page
1.1 Telluric spectrum . . . . .	3
2.1 Echellogram . . . . .	8
2.2 Flat fields . . . . .	16
2.3 Reduced Spectrum . . . . .	19
2.4 Spectral Templates . . . . .	20
2.5 pyhell schematic . . . . .	33
2.6 Spectral fit to Barnard's Star . . . . .	35
2.7 RV Precision vs. Orders Used . . . . .	37
2.9 Multi-order RVs for Barnard's Star 2 . . . . .	37
2.8 Multi-order RVs for Barnard's Star 1 . . . . .	40
2.10 Multi-order RVs for GJ 15 A . . . . .	40
2.11 Multi-order RVs for 61 Cygni A . . . . .	41
2.12 Barnard's Star RV precision . . . . .	43
2.13 GJ 15 A RV precision . . . . .	44
2.14 61 Cygni A RV precision . . . . .	44
2.15 Reduced $\chi^2$ of RVs . . . . .	46
2.16 Barnard's Star template iteration 1 . . . . .	47
2.17 Barnard's Star template iteration 2 . . . . .	48
2.18 GJ 15 A template iteration . . . . .	49
2.19 61 Cygni A template iteration . . . . .	50
2.20 Stellar templates across seasons 1 . . . . .	52
2.21 Stellar templates across seasons 2 . . . . .	53
2.22 Telluric depths . . . . .	54
2.23 Telluric shifts . . . . .	55
2.24 Parameter correlations . . . . .	57
2.25 Parameter correlations subset 1 . . . . .	58
2.26 Parameter correlations subset 2 . . . . .	59
2.27 Wavelength Splines 1 . . . . .	61

2.28	Wavelength Splines 2 . . . . .	62
2.29	Wavelength Splines 3 . . . . .	63
2.30	LSF Hermite Order . . . . .	64
3.1	The <i>TESS</i> PDCSAP light curves of AU Mic from Sectors 1 (top) and 27 (bottom). The lower right plot shows both Sectors phased to 4.836 days. Although the two seasons exhibit nearly identical periodic signals, Sector 27 exhibits moderate evolution. The least-squares cubic spline fit for each Sector is shown in pink. . . . .	81
3.2	Posterior distributions from fits to the predicted RV variability from the $FF'$ technique (eq. 3.5). . . . .	82
3.3	RVs of AU Mic zoomed in on a window with high-cadence, multi-wavelength observations from 2019. Here, we use a disjoint QP GP kernel (eq. 3.1) to model the stellar activity. Each plotted dataset is only corrected according to the best-fit zero points. Data errors are computed by adding the intrinsic errors in quadrature with the GP uncertainty. Although each GP makes use of the same parameters, each still exhibits unique features. This indicates either an insufficient activity model with our cadence or yet-to-be characterized chromatic effects of activity from different wavelength regimes not consistent with a simple scaling relation. . . . .	84
3.4	Here we show the 2019 RVs using kernel $\mathbf{K}_{J1}$ (eq. 3.2) to model the stellar activity. Although there is only one HIRES observation in early 2019, we are still able to make predictions for the HIRES GP for the entire baseline by using joint kernels. . . . .	85
3.5	Same as fig. 3.4, but for our 2020 observations which overlap with the <i>TESS</i> Sector 27 photometry. In red we show the generated $FF'$ curve for spot-induced activity signals (eq. 3.5, arbitrarily scaled) generated from the <i>TESS</i> light-curve (section 3.3.3). . . . .	86
3.6	The best-fit GP amplitudes and uncertainties from kernels without enforcing any dependence with wavelength. We consider cases which let $\eta_\tau$ and $\eta_\ell$ float as well as and our fixed values (see Table 3.2). The solid line is a least-squares solution to the amplitudes for kernel $\mathbf{K}_{J2}$ (eq. 3.3) for the joint-kernel fixed case (pink markers). Horizontal bars correspond to the adopted spectral range for each instrument. . . . .	88



- 3.7 The phased RVs for AU Mic b (left column), and c (right column), and the corresponding best fit Keplerian models, generated from our nominal two-planet model. For each spectrograph, we subtract the unique zero-points, all other planet signals, and the appropriate GP. Corresponding data errors are computed by adding the intrinsic error and GP uncertainty in quadrature. The dark red points are generated by binning the phased RVs using a window size of 0.1, weighted by  $1/\sigma_{RV}^2$  where  $\sigma_{RV}$  are the data errors. In the top row we plot all data used in the fit. In the bottom row, we only show HIRES, iSHELL, and SPIRou. Although the HIRES cadence in 2020 was relatively dense with respect to the activity timescales  $\eta_\tau$  and  $\eta_P$ , the data still appears to be over-fit. . . . . 91
- 3.8 GLS periodograms for AU Mic. Rows 1–4 are generated from our nominal two-planet MAP fit result using  $\mathbf{K}_{J1}$  (eq. 3.2) to model the stellar activity. From top to bottom, with each step applying an additional “correction”: 1. zero-point corrected RVs, 2. activity-filtered RVs, 3. planet b-filtered RVs, 4. planet c-filtered RVs. Annotated from left to right in green are the periods for AU Mic c and b. In the top row, we also annotate in orange (from left to right) potential aliases of the stellar rotation period  $3\eta_P$ ,  $2\eta_P$ , and  $3\eta_P/2$ , followed by the first three harmonics. In the bottom row, we compute a periodogram from an activity-filtered and trend-corrected zero-planet model to indicate how power from planets is absorbed by the GP. In each periodogram, we also identify the false alarm probability (FAP) power levels corresponding to 0.1% (highest), 1%, and 10% (lowest). The clear alias present in all periodograms is caused from the large gap between the two seasons of observations. In the bottom panel, we also plot in pink a Lomb-Scargle periodogram (arbitrarily scaled) of our window function (i.e, identical yet arbitrary RVs at each observation). . . . . 93

3.9	“Brute-force” periodograms for AU Mic with different assumptions for planetary models, but all making use of kernel $\mathbf{K}_{\mathbf{J1}}$ (eq. 3.2) to model the stellar activity. In each row, we perform a MAP fit for a wide range of fixed periods for a particular “test”-planet. In row 1, we include no other planets in our model, and allow for the test-planet’s $TC$ to float. In row 2, we perform the same search but fixing $TC$ to the nominal value for AU Mic b (Table 3.2). In row 3, we include a model for AU Mic b (with $K_b \sim \mathcal{N}(8.5, 2.5)$ , see K21), and search for a second planet again letting $TC$ float. In rows 4–6, we perform the same search but fix the test-planet’s $TC$ to one of the three times of transit for AU Mic c from <i>TESS</i> (in chronological order). In the bottom row, we include nominal models for AU Mic b and c ( $K_b \sim \mathcal{N}(8.5, 2.5)$ , $K_c > 0$ ). We also annotate the same potential aliases with the stellar-rotation period (orange) and planetary periods (green) as in fig. 3.8. . . . . .	94
3.10	Here we plot the mass vs. radius for all exoplanets with provided radii and masses from the NASA Exoplanet Archive (4). For AU Mic b and c, we plot (maroon markers) the masses determined from our two-planet model with kernel $\mathbf{K}_{\mathbf{J1}}$ . We also indicate with an arrow the $5\sigma$ upper limit to the mass of AU Mic c determined from the posterior of $K_c$ . The radii for b and c are those reported in M20. In blue, we plot a piece-wise Chen-Kipping mass-radius relation (5). We also annotate (cyan markers) the masses and radii for a sample of young planets (stellar-age estimated $\lesssim 400$ Myr). . . . .	95
3.11	Histograms depicting our injection and recovery-test results. In the top row, we show the relative confidence interval of the recovered semi-amplitudes ( $K_{\text{rec}}$ ) derived from the MCMC analysis in the case of letting the ephemeris ( $P$ , $TC$ ) float (left) and fixing the ephemeris to the injected values (right). In the bottom row, we compare the recovered semi-amplitude to the injected value ( $K_{\text{inj}}$ ). . . . .	99
3.12	Histograms depicting the recovery of planetary signals without having injected any into the data. In panels 1 and 2, we show the relative confidence interval of the recovered semi-amplitudes ( $K_{\text{rec}}$ ) derived from the MCMC analysis in the case of letting the ephemeris ( $P$ , $TC$ ) float (left) and fixing the ephemeris to arbitrary the arbitrary $TC=2457147.36589$ (middle). On the right, we show the recovered semi-amplitudes for each case. . . . .	99

3.13	Here we plot the observed “RV-color” = $RV(t, \lambda) - RV(t, \lambda')$ ( $\lambda' > \lambda$ ) from our 2019 and 2020 nights with nearly simultaneous measurements at unique wavelengths. These are plotted against the same RV-color difference predicted by our chromatic GP model using kernel $\mathbf{K}_{J2}$ . Pairs consisting of CARMENES-Vis and CARMENES-NIR measurements are nearly transparent to make other pairs more visible. We do not plot pairs of SPIRou and iSHELL because they are tightly centered near zero. A dashed one-to-one line is also shown. The weighted coefficient of determination (R2) is $\approx 0.68$ .	102
B.1	Posterior distributions using disjoint QP kernels (eq. 3.1) for each spectrograph to model the stellar activity, including a two-planet model for the transiting planets b and c. The derived values for $\eta_r$ suggests a more dynamic activity model than the $FF'$ curve prediction suggests. . . . .	107
B.2	Same as fig. B.1 but fixing $\eta_r = 100$ days. . . . .	108
B.3	Posterior distributions for a two-planet fit to the RVs using $\mathbf{K}_{J1}$ (eq. 3.2) to model the stellar activity. . . . .	109
B.4	Same as fig. B.3 but using $\mathbf{K}_{J2}$ to model the stellar activity. . . . .	110
B.5	Same as fig. B.3 but using less restrictive priors for $e_b$ or $\omega_c$ . . . . .	111
D.1	Here we show a subset of the 2019 RVs using kernel $\mathbf{K}_{J2}$ (eq. 3.2) to model the stellar activity and including the full RV dataset. Although we do not include the MINERVA-Australis or IRD RVs in our primary fits in section 3.3, we find they are generally consistent with our stellar activity model. We do not show the phased CHIRON RVs due to their larger residuals. . . . .	131
D.2	Same as fig. D.1, but showing the phased RVs. . . . .	132
D.3	Posterior distributions for a two-planet fit to the full RV dataset using $\mathbf{K}_{J2}$ to model the stellar activity. Blue lines correspond to the 50 <sup>th</sup> percentile of the distribution. Upper and lower uncertainties correspond to the 15.9 <sup>th</sup> and 84.1 <sup>st</sup> percentiles, respectively. The semi-amplitude $K_b$ is $\approx 30\%$ smaller than the subset of 2019-2020 data yields (Table 3.3), however $K_c$ is relatively unchanged. . . . .	133

# **Abstract**

## **RETRIEVAL AND APPLICATIONS OF PRECISE RADIAL VELOCITIES TO DETECT EXOPLANETS**

Bryson L. Cale, PhD

George Mason University, 2021

Dissertation Director: Dr. Peter Plavchan

The radial velocity (RV) technique has proven to be one of the most successful methods to search for extra-solar planets. RV measurements are necessary to independently confirm and determine the masses of orbiting bodies, and thus begin to probe their density and therefore compositions. In this thesis, we develop a set of novel routines to precisely measure the relative velocities of stellar sources with the RV technique by measuring the Doppler shift from high resolution stellar spectra. We demonstrate the applications of our codes to detect and characterize extra-solar planets with a variety of modern spectrographs.

**In chapter 1**, we introduce the radial velocity technique, its success, and current limitations in the modern era.

**In chapter 2**, we introduce the concepts of echelle spectroscopy, and develop techniques (pipelines) in the *IDL* and *Python* programming languages to process the spectra and compute corresponding precise radial velocities of stellar sources. We demonstrate first applications of our codes with the near-infrared iSHELL spectrograph with observations of RV standards.

**In chapter 3**, we perform a case-study on AU Mic. AU Mic is a young & early M dwarf which hosts an edge on debris disk as well as at least two transiting planets. Attempts to detect planets orbiting AU Mic have historically been plagued by the large rotationally modulated stellar-activity signals present in both photometric and radial-velocity observations primarily due to spots (cooler regions) and plages & facula (hotter regions), ultimately driven by the dynamic magnetic fields AU Mic produces. In order to characterize the masses of the recently identified transiting planets, we exploit the wavelength dependence of stellar-activity present in our multi-wavelength RV dataset. Since the RV signal from a planet is achromatic, this helps us to isolate activity from Keplerian signals. We develop chromatic Gaussian process (GP) kernels and introduce methods to aid in isolating chromatic activity signals larger than the Keplerian components. We demonstrate the validity of our RV model through injection and recovery analyses, and ultimately use our model to characterize the AU Mic planetary system.

# Chapter 1: Introduction

## 1.1 The Radial Velocity Technique

Planets do not orbit a stationary host star, but rather the entire system orbits about the center of mass of the system. For single star systems, the star is responsible for the majority of the mass<sup>1</sup>, and therefore kinematically experiences only minor perturbations thanks to Newton's second law. While small, these perturbations are not negligible, and can be measured to determine the existence of orbiting bodies with modern instruments and techniques. To measure these changes in the velocity of the star, we utilize the Doppler method. As a planet gravitationally influences the host-star, the stellar spectrum will be Doppler shifted according to the projected velocity along our line of sight. Significant periods observed in changes to the velocity of the star as a function of time correspond to the period of a planet's orbit, while the amplitude of these velocity changes correspond to the relative mass of the orbiting body. Specifically, the semi-amplitude of the observed velocity signal is given by (6):

$$K = \left( \frac{28.4329 \text{ m s}^{-1}}{\sqrt{1 - e^2}} \right) \left( \frac{M_p}{1 M_J} \right) \left( \frac{M_p + M_\star}{1 M_\odot} \right)^{-2/3} \left( \frac{P}{1 \text{ yr}} \right)^{-1/3} \quad (1.1)$$

Here,  $M_p$  and  $M_\star$  are the masses of the planet and star, respectively.  $P$  is the period of the orbit, and  $e \in [0, 1)$  is the eccentricity of the orbit where  $e = 0$  corresponds to a circular orbit, while for  $e \in (0, 1)$  the orbit is an ellipse.  $e \geq 1$  corresponds to unbounded orbits, and thus not periodic nor typically considered in precise RV work. The factor of  $28.4329 \text{ m s}^{-1}$  corresponds to the semi-amplitude for a  $1 M_J$  planet in a one year orbit around a  $1 M_\odot$  star.

---

<sup>1</sup>>99.5% of the mass in our own solar system is within the Sun.

## 1.2 History, Success, & Limitations

Measuring the minuscule changes in the velocity of a star caused by planet-mass companions has long been a notoriously difficult and delicate craft. To provide a scale of the measurements being recorded, a  $1 \text{ m s}^{-1}$  change in the velocity of a star corresponds to a shift on the detector of approximately  $10^{-3}$  of one pixel. For scale, the Earth induces a measly semi-amplitude of  $\approx 10 \text{ cm s}^{-1}$  on the Sun, while Jupiter induces a signal of  $\approx 12.5 \text{ m s}^{-1}$

### 1.2.1 Instrumental Calibration

Performing Doppler measurements are first complicated by the environmental stability of the spectrograph. In order to measure the stellar RV, one must use a reference spectrum with Doppler stability at least as good as the desired precision (and preferably much better). In particular, the “calibrator” must both provide a means to convert detector pixels to wavelength, and constrain the intrinsic line profile (the shape of a monochromatic light) of the spectrograph. Historically, the two most widely-used calibrators are emission lamps and absorption gas cells. Typically, gas cells are inserted directly into the “science” (stellar) beam, superimposing a forest of absorption lines onto the recorded science spectrum. In the case of lamps, thousands of emission lines are produced over the appropriate spectral range, but these calibration exposures will typically bridge the science images (opposed to simultaneous). Both methods have achieved long-term Doppler stability of  $1\text{-}2 \text{ m s}^{-1}$  (e.g., HARPS, HIRES). Newer techniques leveraging nearly continuous, high signal-to-noise ( $S/N$ ) interference patterns produced by Fabry-Pérot etalons or laser frequency combs are used to provide an even more robust calibrator, and will serve as the “gold-standard” calibrators for next-generation spectrometers (e.g., NEID, ESPRESSO, EXPRES).

### 1.2.2 Telluric Contamination

The process is further complicated by relatively unstable atmospheric (“telluric”) features that contaminate all ground-based data (Fig. 1.1). Light recorded at the spectrograph will

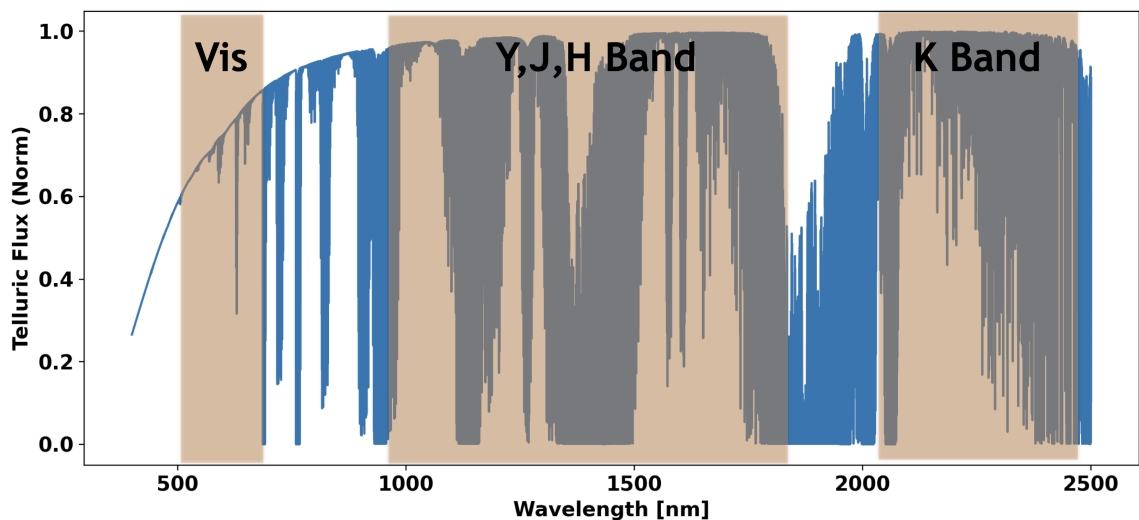


Figure 1.1: Absorption features caused by Earth’s atmosphere. Relevant molecular species are water, methane, carbon dioxide, nitrous oxide, oxygen, & ozone. Highlighted in orange are the three primary wavelength regimes modern echelle spectrographs operate at.

pick up absorption features from Earth’s atmosphere, while telluric emission features will naturally illuminate the entire viewing apparatus. Ironically, these features may be used to calibrate the spectrograph, however their precision is limited to  $> 5 \text{ ms}^{-1}$  due to the changing line profile and atmospheric winds (e.g., 7). Therefore, regions of even moderate telluric contamination must be either flagged or modeled in order to accurately measure the stellar RV at the few  $\text{ms}^{-1}$  level.

### 1.2.3 Not All Stars Are Created Equal

As delicate as these measurements are, the RV technique has been successfully applied to reveal hundreds of systems around solar-type (FGK dwarf) stars since the discovery of 51 Pegasi b in 1995 (8)<sup>2</sup>. Observations are usually performed at visible wavelengths where these stars are brightest and telluric lines are relatively scarce (9; 10).

RV observations of M dwarfs, especially mid- to late-type M dwarfs (M4+), are more

---

<sup>2</sup>The Nobel Prize in Physics 2019 was awarded to Michel Mayor and Didier Queloz for “the discovery of an exoplanet orbiting a solar-type star.”



challenging than those of solar-type stars. M dwarfs are intrinsically faint and require long integration times per epoch to acquire sufficient  $S/N$ , especially for spectroscopic observations where light is dispersed. Late M dwarfs are also more magnetically active (11; 12). Star spots and other sources of activity can introduce RV noise and spurious signals at periods corresponding to the stellar rotation period  $P_{\text{rot}}$  and harmonics  $P_{\text{rot}}/n$  where  $n > 0$  is a small integer (13). A further realization for M1–M4 dwarf stars is the stellar rotation period overlaps with the range in periods of habitable zone worlds (14; 15).

RV follow-up of hotter stars is challenged by their lack of stellar features; their photospheres are hot enough such that most atoms and molecules become fully ionized, and thus emit primarily black-body radiation instead of exhibiting discrete atomic and molecular transitions. Such systems are largely ignored by the RV community due to the significant amount of time needed to achieve adequate precision with so few spectral features.

#### 1.2.4 Wavelength of the Observations

Due to the difficulties of RV observations of M dwarfs in the optical, interest has grown in the last decade in developing near-infrared (NIR) spectrographs for these observations. M dwarfs are brightest at near-infrared (NIR) wavelengths, and the flux contrast between star spots and the surrounding chromosphere is reduced (16; 17; 18; 19; 20). To first order in wavelength, the flux contrast (and thus RV signal) from activity is expected to follow a  $\lambda^{-1}$  relationship, although additional challenges arise from the wavelength dependence of limb-darkening and convective blue-shift (21). NIR RV efforts have made rapid progress in precision (and thus mass detection) capabilities. NIRSPEC on Keck (K-band,  $R \sim 25000$ ) obtained  $45 \text{ m s}^{-1}$  precision observing late M dwarfs (22). CSHELL (K-band,  $R \sim 46,000$ ) on IRTF obtained  $35 \text{ m s}^{-1}$  observing GJ 15 A (23). NIR RV efforts have gained traction both with absorption gas cells (e.g., 24) and the use of fiber-feeds to stabilized environments for instruments. As a recent example, the Habitable Zone Planet Finder (HPF) on the 10 meter Hobby-Eberly Telescope ( $R \sim 50,000$ , Y- and J-bands) has shown  $< 3 \text{ m s}^{-1}$  precision

on Barnard’s Star, sufficient to detect rocky worlds in the habitable zone of M dwarfs (25; 26).

Most NIR RV instruments exploited the  $Y$ ,  $J$ , and  $H$  regions of the spectrum, although RV information content in the Y- and J-band is found to be lower than expected from synthetic spectra (27). The K-band spectra of M dwarfs also contains deep sharp lines of CO at  $\lambda > 2.29 \mu\text{m}$  suitable for RV measurements. However, observations in this wavelength region are also plagued with telluric lines of water and methane as well as other trace molecules that complicate the data analysis (28).

### 1.3 This Work

In this thesis, we develop and apply a set of novel routines to accurately measure the Doppler-shifts in stellar spectra. In chapter 2, we introduce `pychell`, a Python library to process the raw stellar spectra recorded at the telescope and precisely measure the corresponding RVs. We carry-out our first applications and demonstrations with data from the near-infrared iSHELL spectrograph on the NASA Infrared Telescope Facility (IRTF). In chapter 3, we leverage the chromaticity (wavelength) of stellar activity present in RV datasets, introduce methods to mitigate these effects, and apply them to RV follow-up of the young, active, and planet bearing AU Mic system.

## Chapter 2: Process and Analysis of Echelle Spectra with

In this chapter, we introduce our process and analyses of high-resolution echelle spectra to generate precise RVs. At the heart of these analyses is **pychell**, a set of routines to process high-resolution echelle spectra with a focus on applications to precise radial velocities. While it was not our initial goal, **pychell** has become a robust tool for a wide variety of spectrographs. Early versions of **pychell** (formerly PySHELL) were split into *Python* & *IDL* (Interactive Data language) sub-packages, and developed with only the iSHELL spectrometer in mind. Although the current version of **pychell** is fully in *Python* with updated algorithms and now supports a variety of spectrometers, we only describe our first working version of **pychell** made specifically for the iSHELL spectrograph in this chapter. We delegate appropriate sections in the remaining chapters of this thesis to discuss more recent adaptations and modification to **pychell**.

In Section 2.1, we first briefly discuss echelle gratings, the fundamental instrument in precise Doppler work. In Section 2.2, we discuss iSHELL observations of Barnard’s Star (GJ 699), GJ 15 A, and 61 Cygni A, all previously used in RV searches and suitable as RV standards. In Sections 2.3 and 2.4, we discuss the spectral processing and forward modeling tools, respectively, which are used to carefully measure the precise RVs. We present the results in Section 2.5. We analyze the fidelity of our stellar template retrieval in Section 2.5.3, and forward model parameter distributions in section 2.5.4. In Section 2.6 we discuss our particular choice of forward model and how our obtained iSHELL RV precision compares to other precise NIR spectrographs, as well as prospects for planet confirmation. A summary of this work is provided in Section 2.7.

## 2.1 Echelle Gratings

Echelle gratings are the instrument at the heart of precise Doppler work. Recording a continuous spectrum with a large spectral range compared to the resolution of the spectrograph is not efficient with square imaging detectors. Single order echelle spectrographs pick out one order from the diffracted signal to be incident on the detector, centered on a small spectral window surrounding the “blaze-wavelength” (wavelength of max-transmission) of one order. By utilizing a second diffraction element (grating or prism) called a cross-disperser which is aligned perpendicularly to the echelle diffraction axis, different orders can be “stacked” on a square detector. Since the blaze wavelength for each order will gradually change according to the grating equation, each order contains a unique spectral window, although there is typically overlap at the edges of orders in the detector plane. A full description of echelle gratings for precise Doppler work is provided in (29). An example multi-order echelle image (“echellogram”) is shown in figure 2.1.

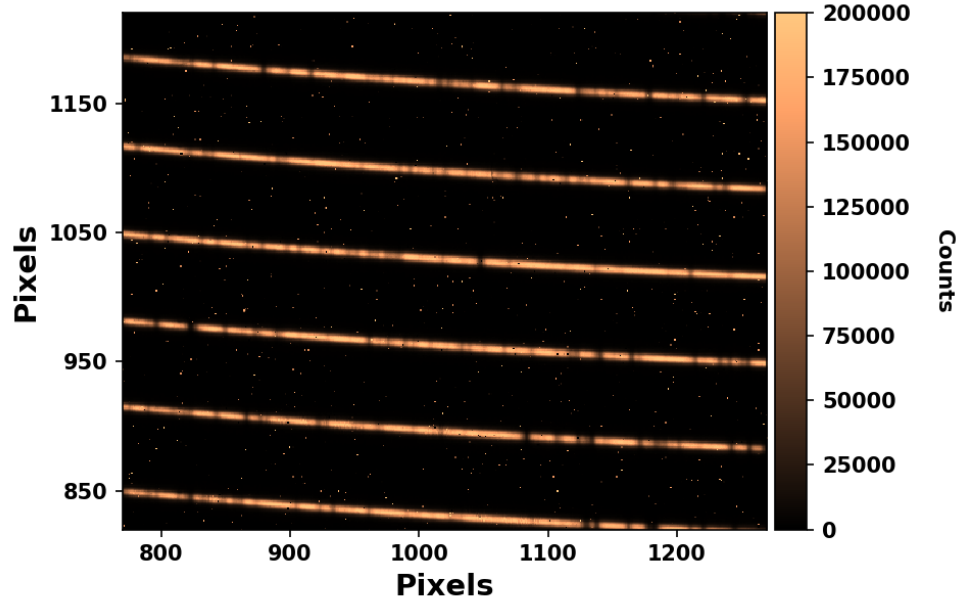


Figure 2.1: A sub-frame of an unprocessed multi-order spectral image of 61 Cygni A from Oct. 16 observed with iSHELL. The full frame contains 29 orders with dimensions 2048 x 2048. Numerous “bad” pixels appearing on the stellar trace as dark values, and between traces as bright values, are flagged during data processing, but can be missed if the  $S/N$  is not sufficient to properly identify them as outliers.

## 2.2 Observations with iSHELL

We obtained echelle spectra with the iSHELL spectrograph on the 3 meter NASA Infrared Telescope Facility (IRTF) between October 2016 and October 2017, with the majority of observations taking place during the first half of this period. Table 2.2 provides the estimated  $S/N$  (per detector pixel) of each observation as well as the number of observations ( $N_{\text{obs}}$ ) obtained each night. Spectra are recorded with iSHELL in *KGAS* mode (2.18–2.47  $\mu\text{m}$ ) with a 0.375” slit at  $R \approx 80,000$ . A Hawaii 2RG array records 29 cross-dispersed echelle

orders ( $m = 212 - 240$ ) spanning this spectral range. A methane isotopologue ( $^{13}\text{CH}_4$ ) gas cell in the calibration unit with 90% continuum throughput is used to provide a common optical path wavelength reference and to constrain the variable line spread function ( $LSF$ ) of the spectrograph (30; 31). To minimize errors in the barycenter correction<sup>1</sup> and telluric optical depths of individual spectra, integration times are limited to 5 minutes. The exposure midpoint (opposed to flux-weighted) is used to determine the barycentric correction since iSHELL does not have an exposure meter as is common in visible precise RV instruments (32). Unfortunately, the error in barycenter correction scales with square of the exposure time (33), so doubling an exposure time will quadruple our barycenter velocity uncertainty. Various factors can further contribute to a non-constant photon rate, particularly changes in airmass and atmospheric transparency. The telluric content (particularly water) can be variable on time-scales of an hour or less along with the changing airmass of our target (34), so we limit our maximum exposure time to avoid any errors that could potentially be introduced in the telluric modeling, although we do not characterize this. We further limit integration times to avoid the nonlinear detector regime of the detector for brighter targets. After every target is observed, a set of five flat-fields is obtained before slewing the telescope to the next target. An example of a raw unprocessed two-dimensional fits image is shown in Fig. 2.1. All data are publicly available online at the NASA/IPAC Infrared Science Archive.<sup>2</sup>

We choose three bright RV standards to evaluate the RV precision obtainable with iSHELL using `pychell` routines. These targets have already been observed to show RV stability at or below the expected iSHELL precision, and are summarized in table 2.1. Barnard’s Star (GJ 699) shows no RV variations down to  $2 \text{ ms}^{-1}$  over several years using data sets from Keck/HIRES and Lick/Hamilton after accounting for the observed secular

---

<sup>1</sup>Barycentric corrections account for the motion of Earth around the Sun and the rotation of Earth at the location of the observatory which bias the measured RVs.

<sup>2</sup>Available at <https://irsa.ipac.caltech.edu/applications/irtf/>. All IRTF data has a proprietary period of 18 months starting at the end of that observing semester.

acceleration of  $4.515 \text{ ms}^{-1} \text{ yr}^{-1}$  (35). More recent efforts have found a low-amplitude periodic signal at 233 days with  $K = 1.2 \text{ ms}^{-1}$  (36). 61 Cygni is a binary system of two comparatively bright K dwarfs with an orbital period of 653 years, neither of which are known to host any planets. GJ 15 A is suspected to host a single planet with  $K = 2.9 \text{ ms}^{-1}$  and a period of 11.44 days (37).

Table 2.1: Summary of Observed Targets.

Star	R.A./Decl.	Spec. Type	$K_{\text{mag}}$	Planets	Reference
GJ 699	17:57:48.5 +04:41:36.1	M4V	4.52	b: $K_{\text{amp}} = 1.2 \text{ ms}^{-1}$ , P=233 days	(38) (36)
GJ 15 A	00:18:22.9 +44:01:22.6	M2V	4.02	b: $K_{\text{amp}} = 2.9 \text{ ms}^{-1}$ , P=11.4 days	(38) (37)
61 Cygni A	21:06:53.9 +38:44:57.9	K5V	2.68	No known planets	(39)

Table 2.2: The obtained  $S/N$  per detector pixel for all iSHELL observations.

UT Date	$N_{\text{obs}}$	Int. Time	$S/N_{\text{i}}^{\text{a}}$	$S/N_{\text{tot}}^{\text{b}}$
—Barnard’s Star—				
2016 Oct. 16	4	5 min	139	277
2016 Oct. 23	7	5 min	159	420
2016 Nov. 06	8	5 min	146	413
2016 Nov. 07	4	5 min	201	402
2017 Apr. 06	9	5 min	132	397
2017 Jun. 18	6	5 min	164	402
2017 Jun. 26	6	5 min	160	392
2017 Jul. 05	7	5 min	152	402
2017 Jul. 29	10	5 min	133	420
2017 Oct. 20	16	20 sec	41 <sup>c</sup>	164 <sup>c</sup>
2017 Oct. 21	16	20 sec	41 <sup>c</sup>	164 <sup>c</sup>
2017 Oct. 22	16	20 sec	41 <sup>c</sup>	164 <sup>c</sup>
2017 Oct. 23	16	20 sec	41 <sup>c</sup>	164 <sup>c</sup>
—GJ 15 A—				
2016 Oct. 16	7	2.5 min	198	525
2016 Oct. 17	12	2.5 min	150	521
2016 Oct. 22	8	2.5 min	179	505
2016 Oct. 23	17	2.5 min	122	503
2016 Nov. 06	16	1.5 min	127	506
2016 Nov. 07	11	2.5 min	158	524



Table 2.3: Table 2.2 continued.

UT Date	N <sub>obs</sub>	Int. Time	$S/N_i^a$	$S/N_{\text{tot}}^b$
—61 Cygni A—				
2016 Oct. 16	10	30 sec	170	537
2016 Oct. 17	12	1 min	152	525
2016 Oct. 22	23	15 sec	105	502
2016 Oct. 23	10	1 min	162	513
2016 Nov. 06	6	1 min	127	506
2016 Nov. 07	16	15 sec	126	502
2017 Apr. 06	7	1.5 min	194	514
2017 Apr. 12	6	1.5 min	210	515
2017 Jun. 18	5	1.5 min	258	577
2017 Jun. 26	6	1.5 min	223	546
2017 Jul. 05	11	1.5 min	154	510

<sup>a</sup>  $S/N_i$  represents the  $S/N$  per spectral pixel for an individual spectrum measured by summing the area of a Gaussian PSF model to the data near the blaze peak with no spectral features with the iSHELL observing user interface. Contamination from the background sky noise is not considered in this estimation.

<sup>b</sup>  $S/N_{\text{tot}}$  represents the total (co-added)  $S/N$  per spectral pixel for a consecutive series of observations, with  $S/N_{\text{tot}} = \sqrt{N_{\text{Obs}}} S/N_i$ .

<sup>c</sup>  $S/N$  was not recorded during the last four observations for Barnard’s Star and are an estimation from the previous nights assuming a relationship of  $S/N \propto \sqrt{t_{\text{exp}}}$ .

## 2.3 Spectral Reduction

“Data reduction” (spectral reduction here) can imply a variety of different steps for different astronomers. For `pychell`, we consider reduction to include at most the following steps:

- Bias, flat-field, and dark frame calibration.
- Mapping of the individual echelle orders on the detector, commonly referred to as “order tracing.”
- Extraction of the desired spectra by converting the two-dimensional spectrum into one-dimension by summing over the spatial axis.
- Telluric, spectral line profile, wavelength, or normalization calibrations/corrections.

Carrying out the first step is a fairly standardized process. Given data-cubes of individual darks, bias, and flat-field images, each of shape  $(N_{\text{img}}, N_y, N_x)$ , we compute the standard master calibration frames as follows, where `*` represents a wildcard character to consider all indices in that dimension, and `MED` represents the median of its argument.

$$M_B(y, x) = \text{MED}(\text{BiasCube}(*, y, x)) \quad (2.1)$$

$$M_D(y, x) = \text{MED}(\text{DarkCube}(*, y, x) - M_B(y, x)) \quad (2.2)$$

$$M_F(y, x) = \text{MED}(\text{FlatCube}(*, y, x) - M_B(y, x) - M_D(y, x)) \quad (2.3)$$

A master dark image is computed for each unique set of exposure times. For slit-fed or fiber-fed flat-field images,  $M_F$  is also re-normalized according to the 75<sup>th</sup> percentile to ensure the science counts are not artificially increased. The corresponding science frame calibrations are applied as:

$$\text{Sci}_{\text{cal}}(y, x) = \frac{\text{Sci}(y, x) - M_B(y, x) - M_D(y, x)}{M_F(y, x)} \quad (2.4)$$

The exposure of each master dark frame  $M_D$  must match the corresponding science (or flat-field) image it is calibrating. The remaining steps in reduction are not as trivial (nor standardized), and are left to the subsections that follow. For iSHELL observations, we briefly explored the use of dark frames during calibration and qualitatively found nearly identical results, so we choose to ignore dark frame calibration for iSHELL data in particular.

### 2.3.1 Order Tracing

Here we seek to determine the approximate locations of the echelle orders on the detector,  $y_m(x)$  where  $m \in \mathbb{N}$  indexes the echelle order, and  $x \in [1, N_{\text{pix}}]$  are the (sub) detector pixels. For simplicity, we assume echelle orders are approximately aligned with detector rows, as is commonly the case<sup>3</sup>. `pychell` requires the use of a featureless, high  $S/N$  spectrum (e.g, master flat-field images) to first approximate  $y_m(x)$ . We isolate individual orders by comparing the master flat field image with a version which is vertically shifted by one pixel. The spatial (vertical) profile of a flat field resembles a top-hat function, and therefore the arithmetic difference between the original image and its shifted version will be nearly zero, except for the edges of orders. With the two isolated edges (top and bottom), we identify and compute the corresponding midpoints of each order, which are then modeled with independent second-degree polynomials. These midpoints provide reasonable starting points for the science images, and will be refined in the remaining steps.

### 2.3.2 Flat-field Artifacts

With iSHELL spectra, we also choose to isolate and remove the sinusoidal fringing from the flat-field images. The fringing in iSHELL is not stable in phase and amplitude, nor is

---

<sup>3</sup>If aligned with detector columns, the image may be transposed before further processing.

the slit-illumination function identical between flat-field (quartz lamp) and stellar (point) sources, and thus does not perfectly divide out if left in the flat-fields. By removing the fringing from the flat-fields, we can then directly model the original fringing signal present in the science spectra simultaneously with other spectral features.

For each flat-field order, we straighten the order into a rectangular array by linear interpolation in the spatial direction determined by the initial trace position,  $y_m(x)$ . We smooth in the spectral direction using a 45-pixel rolling median. We then divide the straightened flat by the spectrally-smoothed flat to isolate instrumental fringing in the flat-field (See Section 2.4.2). A one-dimensional version of the fringing is then obtained by taking the vertical median in the spatial direction, and smoothing the resulting 1-dimensional array with a three-pixel rolling median. We then explicitly model this signal with a modified sinusoid determined by an amplitude, phase, and period. The period is further parametrized to vary linearly over the detector for a given order due to the fact the fringing period gradually changes with wavelength and we are still working in detector-pixel space (opposed to wavelengths). A two-dimensional fringing pattern is then generated by copying the one-dimensional pattern across detector rows. We finally divide the two-dimensional order image by the model fringing pattern in each order to finally remove the fringing present in the flat-fields (Fig. 2.2).

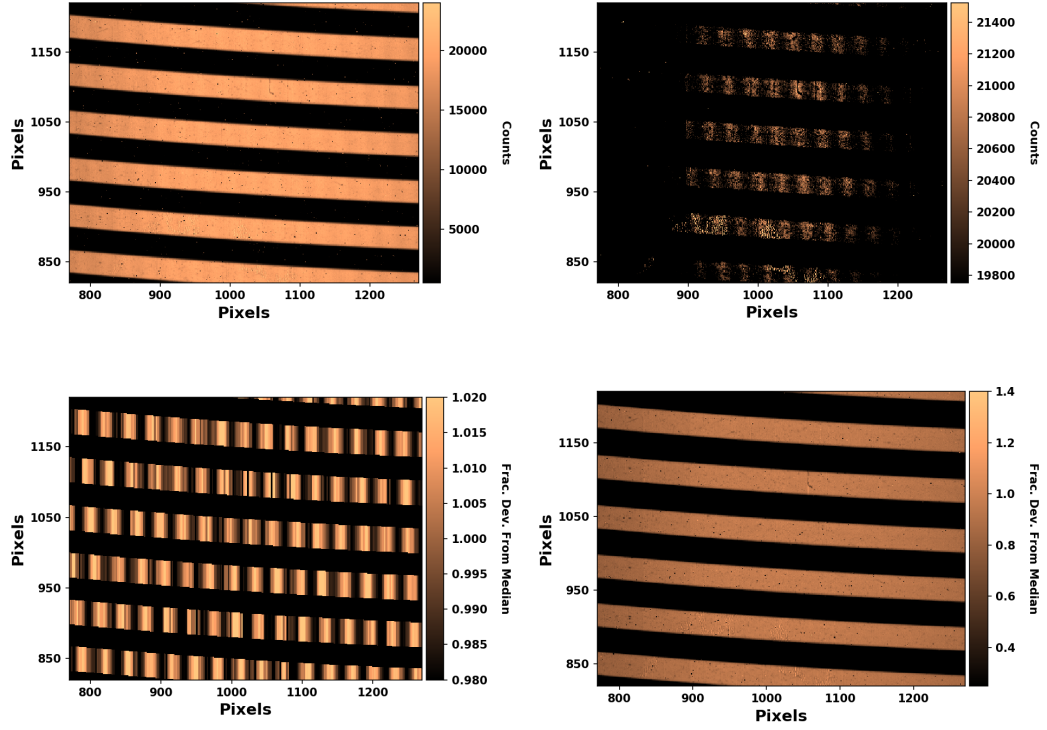


Figure 2.2: *Top Left*: A sub-frame of a raw flat-field image. *Top Right*: The same image and region as the top left but with a high resolution color scaling (narrow range in counts) centered around the fringing signal. *Bottom Left*: The fringing present in the flat-fields isolated through a rolling median with a window comparable to the dominant period in wavelength of  $\Delta\lambda \sim 0.3$  nm. iSHELL fringing is further discussed in Section 2.4.2. *Bottom Right*: A median combined flat-field to be used to correct the science data. Fringing shown in panels 2 and 3 are removed from this image.

### 2.3.3 Spectral Extraction

Spectral extraction is the process of converting a two-dimensional spectrum to one-dimension by summing over the spatial axis, resulting in a single flux value for each wavelength (detector row). To extract a given trace, we must also more precisely determine 1. the location

of the trace on the detector, 2. the illumination profile (also called the seeing profile, point-spread-function - PSF), and 3. a background signal induced from scattered light in Earth's atmosphere and/or atmospheric emission lines.

To extract the spectra, we use a multi-step iterative process. First, we straighten the individual spectral orders of each science exposure with the corresponding order's central position polynomial (from the flat-fields). For each order, an initial PSF is constructed using a median filter in the dispersion (wavelength) direction. A first spectral extraction is performed by using the estimated point spread function as an extraction weight on the rectified order. A cross-correlation of the estimated profile with the straightened data is next performed at each spectral position where the estimated spectral flux density is above half of a cutoff value, set at the 80% quartile value of the spectral flux density. This results in a more precise trace position of the data within each order, which is next modeled with a second-degree polynomial.

We next create a curved two-dimensional spectral profile from the spatial point spread function and refined second-degree polynomial of the science trace position. We obtain a better estimate of the spectral flux density and avoid interpolation by using this two-dimensional profile as an extraction weight on the non-straightened science order. Significant outliers in the resulting spectral flux density are also masked iteratively by flagging large deviations taking place within less than three spectral pixels.

Next, this cleaned up version of the spectral flux density is used in combination with the two-dimensional trace to build a clean version of the two-dimensional science trace. Dividing the science trace by this resulting image allows us to flag bad pixels directly in the two-dimensional data by looking at significant outliers in flux deviations that happen within three pixels. This allows us to mask the deviant pixels directly in the two-dimensional image and to refine our best estimate of the spectral flux density by performing an optimal (maximum  $S/N$ ) extraction (40) using the masked two-dimensional spectral trace and the curved two-dimensional point spread function. The background signal  $B(x)$  is estimated by computing the median of the 8 pixels with the least counts within each vertical aperture

(sub column). We summarize these equations below.

$$F_{opt}(x) = \frac{\sum_y w(y, x) [S(y, x) - B(x)]}{\sum_y w(y, x) \sum_y w(y, x) P(y, x)} \quad (2.5)$$

$$\text{where} \quad (2.6)$$

$$w(y, x) = \left( \frac{P(y, x)}{\sigma(y, x)} \right)^2 \quad (2.7)$$

$$\sigma(y, x) = S(y, x) + \text{RON} + \sigma_B(x) \quad (2.8)$$

$$\sigma_B(x) = \sqrt{\frac{B(x)}{N-1}} \quad (2.9)$$

$$\sigma_F(x) = \frac{\sqrt{\sum_y \sigma(y, x)}}{\sum_y w(y, x) P(y, x)} \quad (2.10)$$

Here, RON is the effective read noise,  $N$  is the number of rows used to compute the background signal with corresponding uncertainty  $\sigma_B(x)$ , and  $\sigma_F(x)$  is the error in the extracted spectrum. For each column, the trace profile  $P$  is normalized such that it integrates to unity. For the analyses presented in 2.5, we had incorrectly normalized our spatial profile such that the maximum value is unity. With discretely sampled pixels, this incorrect normalization injected a sampling alias we incorrectly interpreted as a second fringing signal.

As a final step to refine the spectral flux density, we allow the width of the spatial line profile to vary linearly in the spectral direction within each order. To do this required modeling the spatial point spread function; we found that a Gaussian profile represents the data adequately. A Gaussian profile is fit at each spectral position of the masked two-dimensional science trace, and the resulting Gaussian profile width versus spectral pixel position is fit with a first-degree polynomial. This is used to build a final version of the curved two-dimensional extraction profile, and a last optimal extraction is performed with

this profile to obtain our final extracted spectral flux density. Examples of reduced spectra are shown in Figs. 2.3 & 2.4.

From here, a variety of post-extraction calibrations are typically performed for any spectroscopic work, including wavelength calibration, telluric correction, and/or continuum corrections. `pychell` offers none of this functionality directly, but are all appropriately performed simultaneously when computing RVs in the following section (2.4).

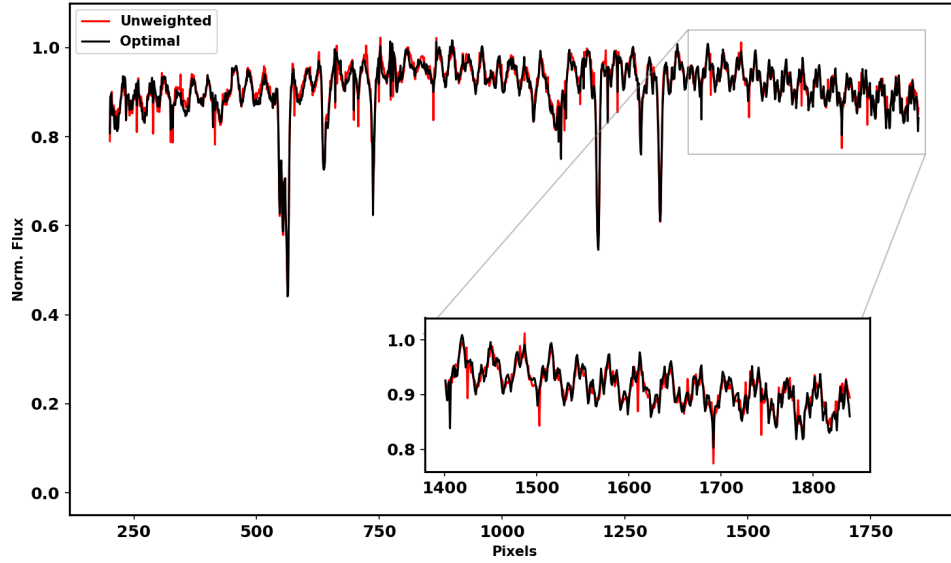


Figure 2.3: A reduced spectrum as a function of pixels (blue to red in wavelength) for 61 Cygni A from Oct. 16, 2016 for order 28 ( $m = 239$ ,  $\lambda = 2.18 - 2.194 \mu\text{m}$ ). The optimally (weighted) extracted spectrum used in RV calculations is shown in black, and the unweighted is shown in red. Inversely weighing pixels by their distance from the center of the trace mitigates sky noise resulting in fewer outliers and an overall smoother spectrum. Order 28 is relatively free of tellurics, gas cell, and stellar lines, so the OS fringing (see Section 2.4.2) and now correctly identified sampling alias are clearly seen with overall peak-to-peak amplitudes of  $\approx 10\%$ .



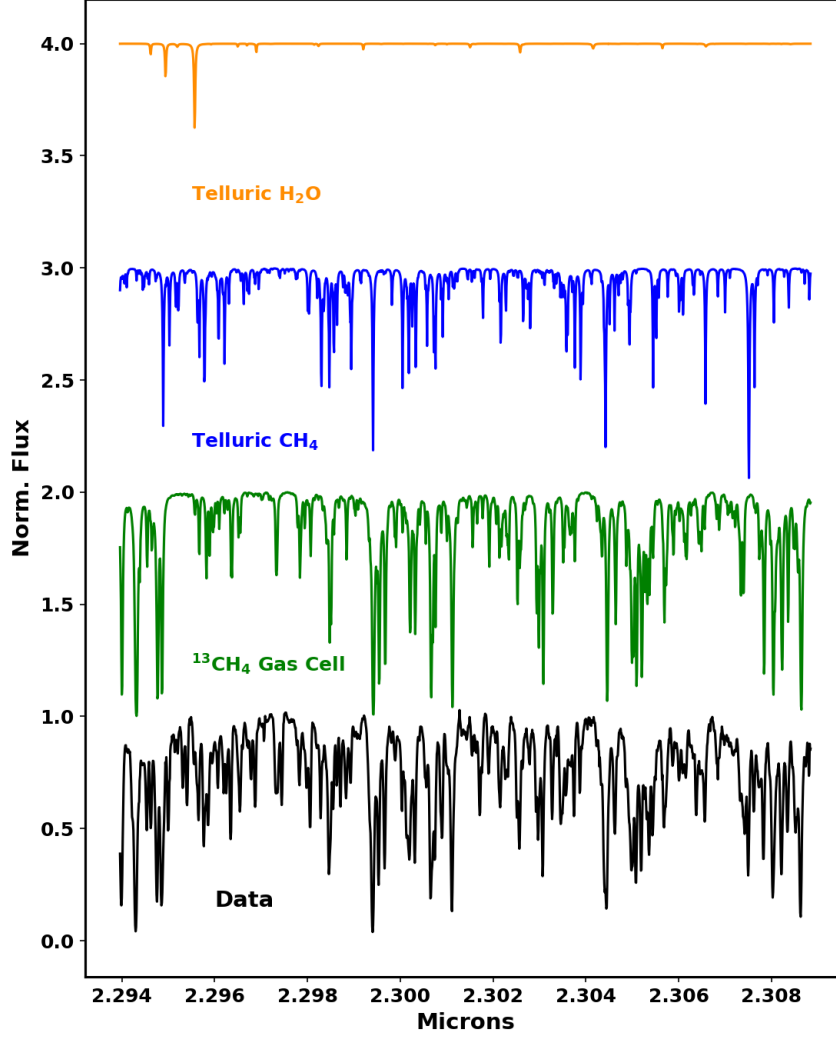


Figure 2.4: A reduced spectrum for 61 Cygni A from Oct. 16, 2016 for order 16 ( $m = 227$ ). The wavelength grid was generated with the initial guess parameters to the RV pipeline (see Section 2.4). The unmodified input templates for the methane gas cell, telluric water, & telluric methane for this order are also shown.

## 2.4 Measuring Radial Velocities

In this section, we describe the methods used to extract RVs by forward modeling single-order extracted (one-dimensional) science spectra (2.4.1–2.4.3), then compute nightly RV measurements and finally optimize multi-order RVs in Section 2.4.4. We adapt the RV pipeline for CSHELL spectra described in (23). We have rewritten the CSHELL code in a *Python* script `pychell` taking into account iSHELL’s larger spectral grasp with multiple orders. Due to variability in the blaze function and due to the lower  $S/N$ , we choose to ignore the first and last 200 pixels at the edges of the extracted spectra. Utilizing the remaining pixels is a subject of future work. Our radial velocity pipeline represents a significant departure from traditional analyses with iodine cell calibrated data. Rather than splitting orders into smaller chunks and introducing discontinuities at the boundaries, we model entire orders as a single “chunk”. This necessitates a more complex forward model than is used with traditional iodine cells (e.g. (41)).

### 2.4.1 Choice of Numerical Solver

To fit a model to the extracted one-dimensional spectra, we have implemented a custom downhill Nelder-Mead algorithm that performs simplex calls for the entire parameter space followed by consecutive two-dimensional subspace calls for all neighboring pairs of parameters to better handle large dimensional spaces, as standard Nelder-Mead algorithms fail to converge. A similar approach that we did not test would be to: first use `SciPy`’s `minimize` routine with `method=Nelder-Mead` a single time for the entire parameter space; second use `minimize` for each consecutive pair of parameters keeping others constant  $((1, 2), (2, 3), \dots, (N_{\text{pars}} - 1, N_{\text{pars}}), (N_{\text{pars}}, 1))$ ; and finally third, repeat the first two steps for the number of parameters in the model. The fit quality is continuously improved with each call to `minimize` as the parameters converge. Our algorithm is therefore dependent on the parameter ordering, and we do not explore the impact of parameter ordering

in this work. However, the RMS of the residuals typically converges before  $\sim N_{\text{pars}}/2$  iterations of the algorithm. Our specific Nelder-Mead algorithm in *Python* for a given simplex is based on that used for CSHELL given by (42) but with stricter convergence requirements. Specifically, the largest fractional difference in the RMS for the current simplex must be less than  $10^{-5}$  three times in a row for the solver to be considered successfully converged.

### 2.4.2 Spectral Forward Model

For a given echelle order, we define the normalized forward model intensity as

$$I_M(\lambda) = B(\lambda)F_{\text{AR}}(\lambda)LSF(\lambda) * [I_{\star}(\lambda_{\star}) T_g^{\tau_g}(\lambda) T_t^{\tau_t}(\lambda_t) F_{\text{OS}}(\lambda)] \quad (2.11)$$

where  $*$  represents a convolution. We describe each of the forward model terms in turn.  $I_{\star}(\lambda_{\star})$  is the Doppler shifted stellar spectrum derived iteratively and described in detail in Section 2.4.3.  $T_g$  is our gas cell spectrum, obtained with a Fourier Transform Spectrometer (FTS) at the NASA Jet Propulsion Laboratory (JPL) at  $R \sim 500,000$  (30; 31). Like (23), we find the gas cell optical depth  $\tau_g = 0.97$  (vs. unity) because of the off-axis angle the gas cell was placed in the FTS, as opposed to CSHELL & iSHELL where the path length is minimized.  $T_t(\lambda_t)$  corresponds to the Doppler shifted telluric absorption spectrum with optical depth  $\tau_t$ . For *KGAS* mode, the relevant telluric components are water ( $\text{H}_2\text{O}$ ), methane ( $\text{CH}_4$ ), nitrous oxide ( $\text{N}_2\text{O}$ ), and carbon dioxide ( $\text{CO}_2$ ). Each component is obtained from *Transmissions of the AtmosPhere for AStronomical data, (TAPAS)* (43). We use realistic temperature-pressure profiles for Maunakea corresponding to the zenith and date of April 12, 2018 at midnight (arbitrarily chosen). The telluric shift is common to all species, but each can have different optical depths to account for variable atmospheric content. The stellar and telluric shifts are computed on a logarithmic grid keeping  $\Delta \ln \lambda = v/c = \text{constant}$ . If a telluric component has no absorption features  $> 1\%$  prior to convolution, it is excluded from the fit for that order. The effective sampling of the gas cell and telluric templates in

our spectral model are approximately 5 and 15 times that of the data, respectively.

$B(\lambda)$  is the residual blaze function left over after the flat division in data reduction. The residual blaze is relatively consistent across orders for a sequence of observations, and is approximately quadratic. While the deviations from the quadratic are not well-modeled with an analytic function, they are relatively small in flux ( $< 10\%$ ). We first model the blaze with a quadratic to approximate the general curvature of the continuum, then use 14 cubic splines as an additive correction. A wavelength grid for the blaze function spline correction is generated by first starting from an initial guess for the wavelength solution. The corresponding  $\lambda_j$  grid for each spline point  $bs_j$  is then generated using a linearly spaced array with endpoints corresponding to the estimated wavelengths of pixels 200 and 1848 (the cropped data) with an extra padding of 0.1 nm to account for the error in the initial wavelength solution, ensuring that all points are bridged by at least two spline knots.

$LSF$  represents the line spread function (line profile) of the spectrograph and is constructed using a sum of Gaussians with Hermite polynomial coefficients (44). These are derived iteratively using

$$\psi_k(x) = \sqrt{\frac{2}{k}} \left( x\psi_{k-1}(x) - \sqrt{\frac{k-1}{2}} \psi_{k-2}(x) \right) \quad (2.12)$$

$$\text{with } \psi_0(x) = \pi^{-\frac{1}{4}} e^{-\frac{1}{2}x^2} \text{ and } \psi_1(x) = \sqrt{2}x\psi_0(x) \quad (2.13)$$

where  $x = \lambda/a_0$  with  $a_0$  being the Gaussian width of  $\psi_0$ . The  $LSF$  is then constructed by summing over  $\psi_k$ ,

$$LSF(x) = \psi_0(x) + \sum_{k=1}^{N_H} a_k \psi_k(x) \quad (2.14)$$

where  $N_H$  is the highest order of the Hermite function series. We use  $N_H = 6$  (up to  $a_5$ ), and explore other *LSF* models in Section 2.6.2. The *LSF* is area-normalized as a final step. Further, the convolution is only performed within a window of  $\pm 0.17$  nm for the model pixel as convolution is computationally expensive, and the LSF quickly goes to zero near the edges of this window.

Like the residual blaze function, we compute the wavelength grid of the data,  $\lambda(P_i)$  for pixels  $\{P_i\}$ , via a main quadratic component, plus a cubic spline correction for small local deviations. Unlike the blaze, a need for splines here is not initially obvious. As discussed further in Section 2.6.1, however, inclusion of a spline correction in the wavelength solution improves the resulting RVs. To obtain the main quadratic component for the wavelength solution, pixel  $P_i \in \{1, 1024.5, 2048\}$  (from blue to red) is mapped to a window  $\lambda_i \pm 0.05$  nm. An initial guess for the zero points  $\lambda_i$  are predetermined from modeling several nights of Vega data with no stellar lines. From here, the polynomial coefficients are determined through a matrix inversion and a quadratic wavelength solution is obtained for all pixels. While  $\lambda_i$  are not orthogonal parameters, we find that polynomial coefficients yield similar RV precision, and opt to use set-points for their simple behavior. Wavelength splines are placed on top of the quadratic by first choosing evenly spaced pixels (for the cropped data) equal to the number of splines plus one. Each pixel gets mapped to the range  $\pm 0.0125$  nm and are interpolated onto the data pixel grid using cubic spline interpolation. The sum of the quadratic and spline correction yields the final wavelength solution for a given spectrum.

## Fringing

In (45), we discuss two sources of fringing present in iSHELL spectra:  $F_{OS}(\lambda)$  &  $F_{AR}(\lambda)$ . After a closer inspection of our spectral extraction codes, we learned that  $F_{AR}(\lambda)$  is caused by a sampling alias and injected into the data during spectral extraction (Section 2.3). We briefly discuss the  $F_{OS}(\lambda)$  term. We leave the description of the model and corresponding parameters used for the injected signal  $F_{AR}$  to (45).

We initially attributed  $F_{OS}(\lambda)$  to the order selection (OS) filter (45), before the light

is diffracted at the echelle grating. However, upgrades to iSHELL in late 2019 including a wedged version did not eliminate this source of fringing. This yet to be identified low amplitude interference signal is present in raw, unprocessed iSHELL data, so we are certain it is not introduced during data-processing (see fig. 2.2). The sinusoidal-like pattern is modeled by:

$$F_{\text{os}}(\lambda) = 1 - A_{\text{os}} \left[ \frac{2}{\mathcal{F}_{\text{os}}} \left( \frac{1 + \mathcal{F}_{\text{os}}}{1 + \mathcal{F}_{\text{os}} \sin^2(\delta_{\text{os}}/2)} - 1 \right) - 1 \right], \quad (2.15)$$

$$\text{where } \delta_{\text{os}} = \frac{2\pi D_{\text{os}}}{\lambda} \text{ and } \mathcal{F}_{\text{os}} = \frac{4R}{(1 - R)^2}. \quad (2.16)$$

Here,  $A_{\text{os}}$  is the amplitude of the signal and  $D_{\text{os}}$  traces the optical path length through the cavity.  $\mathcal{F}_{\text{os}}$  corresponds to the finesse of the cavity, where  $R$  is the reflectance (46). A large finesse manifests as sharper downward cavity absorption spikes for the sinusoid, but we don't see significant evidence for a large cavity finesse for  $F_{\text{os}}(\lambda)$  in our data. Varying  $\mathcal{F}_{\text{os}}$  reveals no obvious preference for any particular value and solutions settle at both upper and lower bounds (0.1, 2) and shows no significant improvement in RVs, so we force  $\mathcal{F}_{\text{os}} = 1$ . A summary of all forward model parameters is given in table 2.4.

Table 2.4: A summary of the spectral forward model parameters used to compute precise RVs from the iSHELL spectrograph.

Num.	Description [units]	Symbol	Value/Bounds
1	Stellar Doppler Shift [ $\text{ms}^{-1}$ ]	$v_{\star}$	unbounded
2	Gas Cell Optical Depth	$\tau_g$	0.97
3	Telluric Doppler Shift [ $\text{ms}^{-1}$ ]	$v_t$	(-200, 200)
4	H <sub>2</sub> O Optical Depth	$\tau_{t1}$	(0.02, 4.0)
5	CH <sub>4</sub> Optical Depth	$\tau_{t2}$	(0.1, 3.0)
6	N <sub>2</sub> O Optical Depth	$\tau_{t3}$	(0.05, 3.0)
7	CO <sub>2</sub> Optical Depth	$\tau_{t4}$	(0.05, 3.0)
8	OS Filter Fringing Amplitude	$A_{\text{OS}}$	(0.015, 0.043)
9	OS Filter Fringing Cavity Length Scale [nm]	$D_{\text{OS}}$	$(1.8390 \times 10^7, 1.8393 \times 10^7)$
10	OS Filter Fringing Finesse	$\mathcal{F}_{\text{AR}}$	1.0
11-13	Wavelength Solution Lagrange Points (3 total) [nm]	$\lambda_i$	$\pm 0.05$
14	Blaze Function Quadratic Term	$b_2$	$(-5 \times 10^{-5}, 1 \times 10^{-8})$
15	Blaze Function Linear Term	$b_1$	$(-5 \times 10^{-4}, 5 \times 10^{-4})$
16	Blaze Function 0 <sup>th</sup> Order Term	$b_0$	(0.98, 1.08)
17	<i>LSF</i> Width [Model pixels]	$a_0$	(5.5, 12)
18-23	<i>LSF</i> Hermite Terms (6 total)	$a_j$	$\pm 0.4$
24-38	Blaze Spline Lagrange Point (15 total)	$bs_j$	$\pm 0.135$
39-45	Wavelength Solution Spline Lagrange Points (7 total) [nm]	$ws_j$	$\pm 0.0125$

### 2.4.3 Stellar Template Retrieval

The derivation of the unconvolved stellar spectrum  $I_\star$  has consistently proven to be a difficult step in forward modeling spectra, particularly in the NIR (24). One approach is to use synthetic model spectra instead. Models of stellar atmospheres can produce synthetic stellar spectra given the effective temperature, metallicity, and surface gravity (22; 47; 48; 49). Due to their lower effective temperatures, atmospheres of late M dwarfs (and brown dwarfs) contain molecular ro-vibrational transitions which can which can significantly contribute to the opacity and affect the emitted spectrum at certain wavelengths (50). While the addition and refinement of molecular opacities and full 3D radiation transfer in newer models (such as the BT-Settl PHEONIX models) are providing a better match with observations (51), there are still some deficiencies.

A second approach is to deconvolve spectra of A or B stars with little to no stellar spectral features observed through an absorption gas cell (e.g iodine). Spectral lines from the gas cell (and tellurics) provide a means of obtaining the line profile ( $LSF$ ) of the spectrograph, and this can be used to deconvolve the spectrum of a science target taken just before or soon after at a similar airmass and direction in the sky. However this approach presumes the  $LSF$  remains stable between observations. This may be true for instruments relying on stabilization, but may not be the case for iSHELL as it slews with the telescope at the Cassegrain focus.

We therefore choose to rely on the target observations themselves to extract the stellar spectrum using an iterative deconvolution method described in (52). If  $I_\star$  is the only unknown variable in the model, then the residuals from a model using an imperfect stellar template correspond to the missing (or extra) features of the stellar template, up to a convolution and Doppler shift. Furthermore, by averaging together many spectra, the coadded signal-to-noise is much higher than in individual spectra. In the limit of iteratively adding the residuals back to the stellar template, the template approaches the unconvolved spectrum. This iterative deconvolution method does have its own limitations. First, sufficient sampling at multiple barycenter velocities with high combined  $S/N$  are necessary



(e.g. two RV data points are not enough). Second, residual correlated noise can gradually get repeatedly added into the stellar template from missed bad pixels, or from non-stellar spectral features that are not well fit.

In our work, we start with a flat guess for  $I_\star$  and forward model all spectra. We choose a forward model wavelength grid resolution that is about 8 times the data spectral resolution to oversample the data and  $LSF$ . Higher resolution models yield similar RV precision and RMS values. To compare the model to the observed spectrum (compute an RMS), the high resolution model is linearly interpolated onto the lower-resolution data grid. We shift each set of residuals to a pseudo rest frame of the star according to the barycenter corrections ( $v_{\text{BC}}$ ) obtained from *barycentric\_vel.pro*<sup>4</sup> (32), decoupling stellar features from any coherent features in the rest frame of the gas cell. We interpolate residuals onto the high resolution model wavelength grid using cubic splines and then median combine across spectra, weighted by  $\text{RMS}^{-2}$  of the residuals from the forward model fit. We add the median values to the previous template, and re-fit the spectra. We repeat this process until the RVs stabilize, which happens anywhere between 5-40 iterations for orders low in RV content, but typically at later iterations for orders high in RV content. We run all targets through 41 iterations to assess convergence and RV precision.

Furthermore, we run the flat template twice on the “first” iteration, where we attempt to minimize the effect of the deep stellar CO lines on the solver by masking values deeper than  $4\sigma$  in the residuals of the first attempt. The blaze function splines in particular are not well-constrained in the presence of poorly fit stellar lines, and are not included in the first iteration. We do not assess the impact of the initial error in the blaze on the RVs and stellar template generation at later iterations. We also force  $\max\{I_\star\} \leq 1$ , as the continuum is not well-constrained in early iterations. This requirement may be loosened at later iterations, although this is not explored in this work. Lastly, on iteration 10 and each iteration thereafter, we flag the worst 5 pixels in each set of residuals (see Fig. 2.6). After 41 iterations, this flags nearly 10% of all originally used pixels (150 of  $\sim 1648$ ), but

---

<sup>4</sup>Available at <http://astrutils.astronomy.ohio-state.edu/exofast/>

improves RV precision at later iterations. Each iteration produces a Doppler shift  $v_\star$  for each individual spectrum (and order). To calculate an individual relative RV, we “subtract” off the barycenter correction from the full Doppler shift,  $RV_\star = v_\star + v_{\text{BC}}$ . An outline of the forward model is given in Fig. 2.5.

After each iteration for a given order, we output text files and corresponding figures for the:

- Best fit model to the data and corresponding parameters.
- Wavelength solution to the data.
- Flagged (ignored) pixels.
- The stellar template used for this iteration.
- Individual and co-added nightly RVs.
- Residuals between the data and models with flagged pixels marked as zeros and the corresponding RMS values and number of target function calls.

To forward model our spectra in a timely manner, we use the ARGO cluster provided by the Office of Research Computing at George Mason University, VA, which can designate 280 cores to a single user, and the exo cluster at George Mason University with 216 cores at the time of this work. Forward modeling a single-order spectrum takes 5-15 minutes at early iterations per core, but only 1-5 minutes at later iterations as parameters have already converged from their updated initial guess.

#### 2.4.4 RV Calculations

We explore two methods for computing one radial velocity measurement for each night averaged across echelle orders. The first extends on (23) utilizing a series of weighted statistical formulas (Section 2.4.5). We also explore a second approach which numerically solves for the relative “zero-points” for each echelle order (Section 2.4.6).

### 2.4.5 Weighted Statistics

In the equations that follow,  $i$ ,  $j$ ,  $k$ , &  $m$  correspond to the  $i^{\text{th}}$  night,  $j^{\text{th}}$  individual observation,  $k^{\text{th}}$  data pixel, and  $m^{\text{th}}$  echelle order, respectively. In order to minimize our RV error per epoch, individual observations at  $S/N_i$  are co-added to obtain a measurement at  $S/N_{\text{tot}}$  (see table 2.2), weighted by  $\text{RMS}^{-2}$  from the forward model fit:

$$RV_{i,m} = \frac{\sum_j^{N_{\text{Obs}}^i} RV_{m,j} w_{m,j}}{\sum_j^{N_{\text{Obs}}^i} w_{m,j}}, \quad (2.17)$$

$$\text{where } w_{m,j} = \frac{N_{\text{pix}}^{m,j}}{\sum_k^{N_{\text{pix}}^{m,j}} [I_{\text{Obs}}(\lambda_k) - I_M(\lambda_k)]^2} \quad (2.18)$$

where  $RV_{m,j}$  and  $w_{m,j}$  are the  $j^{\text{th}}$  individual RVs and weights for order  $m$ , respectively.  $N_{\text{Obs}}^i$  corresponds to the number of observations for the  $i^{\text{th}}$  night.  $I_{\text{Obs}}$  and  $I_M$  are the observed and model spectra, respectively, computed at the  $k^{\text{th}}$  data pixel.  $N_{\text{pix}}^{m,j}$  is the number of used pixels for the  $j^{\text{th}}$  observation for order  $m$  (e.g.  $N_{\text{pix}}^{m,j} \sim 1648$ —flagged pixels). Deviant pixels flagged during data reduction or forward modeling are not included in the sum.

Nightly error bars are computed via an unbiased weighted standard deviation, divided by the square root of the number of spectra used for that night,  $N_{\text{Obs}}^i$ .

$$\delta RV_{i,m} = \sqrt{\frac{\frac{\sum_j^{N_{\text{Obs}}^i} w_{m,j}}{(\sum_j^{N_{\text{Obs}}^i} w_{m,j})^2 - \sum_j^{N_{\text{Obs}}^i} w_{m,j}^2} \sum_j^{N_{\text{Obs}}^i} w_{m,j} [RV_{m,j} - RV_{i,m}]^2}{N_{\text{Obs}}^i}} \quad (2.19)$$

Before RVs from different echelle orders are combined, the weighted average RV  $\overline{RV_m}$  of each order is subtracted off. Combined nightly RVs are then computed through a second weighted average,

$$\overline{RV_m} = \frac{\sum_i^{N_{\text{nights}}} w_{i,m} RV_{i,m}}{\sum_i^{N_{\text{nights}}} w_{i,m}} \quad (2.20)$$

$$RV_i = \frac{\sum_m^{N_{\text{Ord}}} w_{i,m} [RV_{i,m} - \overline{RV_m}]}{\sum_m^{N_{\text{Ord}}} w_{i,m}} \quad (2.21)$$

$$\delta RV_i = \sqrt{\frac{\frac{\sum_m^{N_{\text{Ord}}} w_{i,m}}{(\sum_m^{N_{\text{Ord}}} w_{i,m})^2 - \sum_m^{N_{\text{Ord}}} w_{i,m}^2} \sum_m^{N_{\text{Ord}}} w_{i,m} [RV_{i,m} - \overline{RV_m} - RV_i]^2}{N_{\text{Ord}}}} \quad (2.22)$$

$$\text{with } w_{i,m} = 1/\delta RV_{i,m}^2 \quad (2.23)$$

where  $N_{\text{Ord}}$  is the number of echelle orders used.

#### 2.4.6 Detrending Minimization

Second, to better constrain the intrinsic order dependent characteristic RVs (assumed to be  $\overline{RV_m}$  above), we utilize a version of the Trend Filtering Algorithm (TFA) (53) which is frequently used to remove systematics and detrend light curves (54; 55). We implement and minimize a modified weighted formula from (56) akin to the weighted implementation of TFA in (57):

$$\sum_{i,m} w_{i,m} [RV_{i,m} - \overline{RV_m} - RV'_i - \overline{RV'_m}]^2 \text{ where } w_{i,m} = 1/\delta RV_{i,m}^2 \quad (2.24)$$

$RV_{i,m}$  are the nightly RVs from Eq. 2.17,  $\overline{RV'_m}$  are the new order offsets, and  $RV'_i$  are the “detrended” RVs for the  $i^{\text{th}}$  night.  $\overline{RV'_m}$  and  $RV'_i$  are sets of free parameters with lengths  $N_{\text{Ord}}$  and  $N_{\text{nights}}$ , respectively. The weighted average  $\overline{RV_m}$  of each order from Eq. 2.20 is still subtracted from  $RV_{i,m}$  before optimizing. Values of  $\overline{RV'_m}$  and  $RV'_i$  are set to zero as an initial guess with bounds  $\pm 5 \text{ ms}^{-1}$  and  $\pm 50 \text{ ms}^{-1}$ , respectively. Final error bars are computed using Eq. 2.22 with the detrended orders,  $RV_{i,m} - \overline{RV_m} - \overline{RV'_m}$ . The parameters are optimized using the same Nelder-Mead algorithm described in Section 2.4.1. To lift the degeneracy between offsets and RVs, we lock the offset value of the first used order.

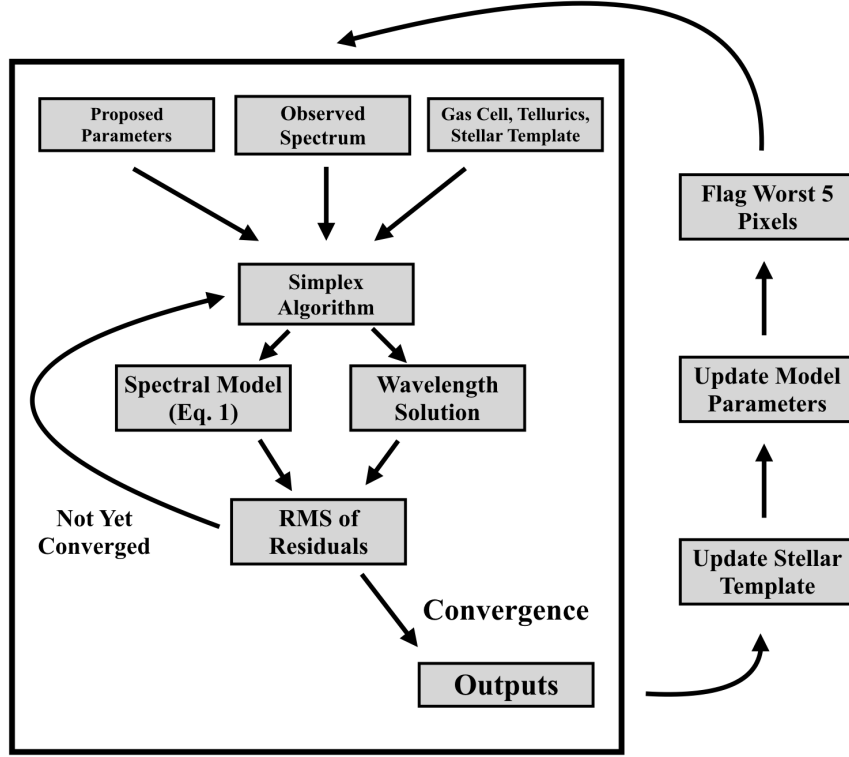


Figure 2.5: A schematic of the RV pipeline. The proposed parameters for the first iteration are given in table 2.4. After each iteration, a new stellar template is generated by co-adding the barycenter shifted residuals, and the new proposed parameters are set to the previous iteration’s converged values. The worst 5 pixels are only flagged on iteration 10 and each iteration thereafter.

## 2.5 Results

For each of the three stars, we run orders 5–26 ( $m = 216–237$ ) through 41 iterations. Order numbers 1–4 ( $m = 212–215$ ) contain sufficient stellar and gas cell RV information content, but are also higher in water absorption and haven’t yielded comparable RV precision ( $>30 \text{ m s}^{-1}$  long-term). We aim to explore a more sophisticated telluric model for these orders in future work. Higher order numbers shortward of the CO band ( $< 2.29 \mu\text{m}$ ,  $m > 229$ ) are relatively low in stellar RV content and have fewer gas cell lines for a precise wavelength calibration (see Section 2.5.2).

For Barnard’s Star, we also compute RVs separately from the first nine nights for orders 6–17 ( $m = 217–228$ ), which we refer to as the “high  $S/N$  run” in the rest of this chapter. Barnard’s Star has historically been shown to have the highest long-term RV stability with precisions below our expected noise floor, so we use it to assess multi-order RV precision (Section 2.5.1), forward model parameter distributions (Section 2.5.4) and alternative forward model implementations (Section 2.6). This also shows the impact of including lower  $S/N$  observations in the stellar template generation. Fig. 2.6 shows example fits of the model spectrum to a high and low  $S/N$  observation of Barnard’s Star. The residuals (and thus RMS) for the low  $S/N$  observations are typically twice as large compared to the high  $S/N$  observations ( $\sim 2\%$  vs.  $1\%$ ), and are therefore weighted less in generating the stellar template.

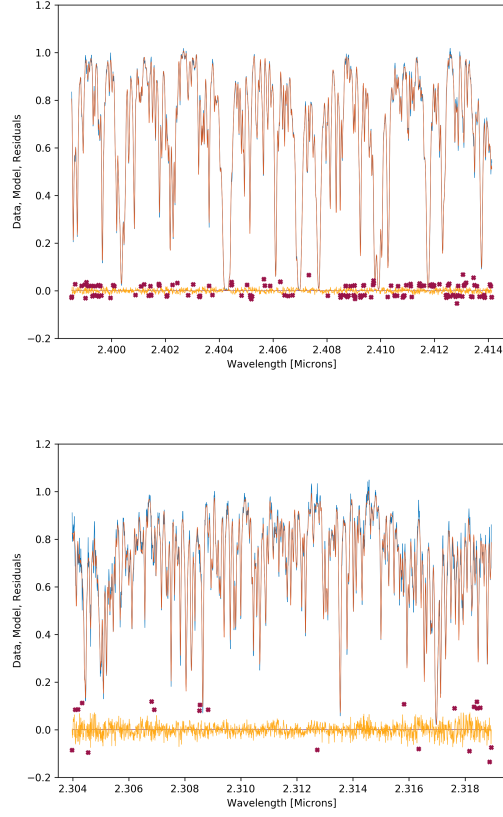


Figure 2.6: *Top*: An example fit to a spectrum of Barnard’s Star from July 29, 2017, for order 6 ( $m = 217$ ) from iteration 41 (last) from the high  $S/N$  run. The data is in blue and the model in red. The deep and wide absorption lines with near zero transmission correspond to water in Earth’s atmosphere. The worst pixels flagged between iterations 10-41 are marked as red X’s. *Bottom*: A lower  $S/N$  example fit from Oct. 20, 2017, to a spectrum of Barnard’s Star for order 15 ( $m = 226$ ) and iteration 15. The data is in blue and the model in red. Any major stellar features will have visually converged at this point.

### 2.5.1 RVs

To assess our combined order precision, we utilize a powerset (all possible subsets of a given set) to analyze the RV precision as a function of orders used and look for orders that



statistically yield lower combined RV precision. We do so using the weighted statistical approach given by eqs. 2.17–2.23. Using Eq. 2.25 (see Section 2.5.2), we take our RV precision  $\sigma_{\text{RV}} \propto N_{\text{Ord}}^{-1/2}$ , and find the long-term RV precision follows this relationship (Fig. 2.7). Lastly, for Barnard’s Star, we subtract off from each individual (single spectrum) RV the secular acceleration of  $4.515 \text{ m s}^{-1} \text{ yr}^{-1}$  given by (35) before any multi-order or nightly RVs are computed. We don’t perform this for other targets as their relative spatial motion is not significant enough to produce a detectable acceleration. Orders that yielded the lowest long-term precision are then optimized through eq. 2.20, and typically reproduce RVs from the weighted formulation (Fig. 2.9). The long-term RV precisions for each individual order are presented in table 2.5. We present the best combined order precision in table 2.6 and corresponding figures 2.8–2.11. We obtain best case long-term RV precisions of  $4.3 \text{ m s}^{-1}$  for Barnard’s Star,  $2.7 \text{ m s}^{-1}$  for GJ 15 A, and  $3.8 \text{ m s}^{-1}$  for 61 Cyg A. For 61 Cyg A, the RV is a large outlier for the last night ( $+ 1 \text{ km s}^{-1}$ ). This outlier has a typical multi-order RV uncertainty, and survived numerous modifications to the code during development. We suspect this is an observational error where we mistakenly observed 61 Cygni B, or a flare event on the surface of the star. We therefore disregard this night from any long-term RV calculations.

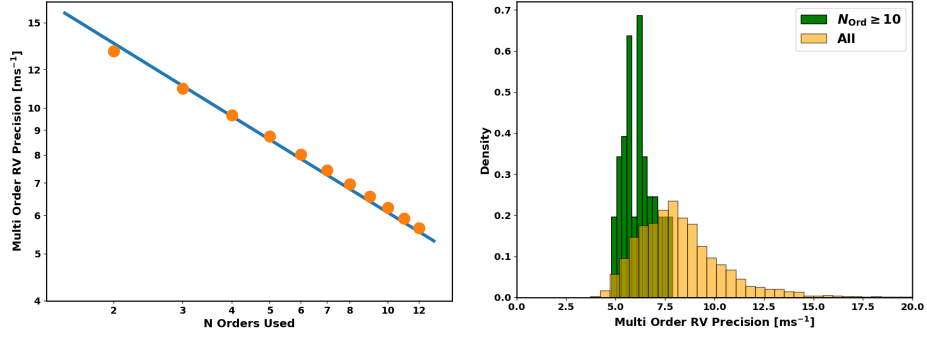


Figure 2.7: *Left*: The orange circles correspond to the average long-term RV RMS obtained for all possible combinations of  $N$  orders. The trend is obtained by fitting a function  $AN_{\text{Ord}}^{-1/2}$  where  $A$  is a constant parameter. On average our multi-order velocities are consistent with averaging out random noise. *Right*: A histogram of long-term RV precisions obtained trying all possible order combinations for the 12 orders (6–17,  $m = 217 - 228$ ) for the high  $S/N$  Barnard’s run. In yellow, we show all order combinations of 2–12 orders (e.g. there is only one 12-order combination, 12 11-order combinations, etc.), and in green order combinations with 10–12 combined orders. The total number of order combinations are 4083 and 79, respectively. For the latter green histogram with 10 or more combined orders, the 5th percentile is  $5.0 \text{ m s}^{-1}$ , while the 10th percentile is  $5.2 \text{ m s}^{-1}$ , and the 20<sup>th</sup> is  $5.4 \text{ m s}^{-1}$ .

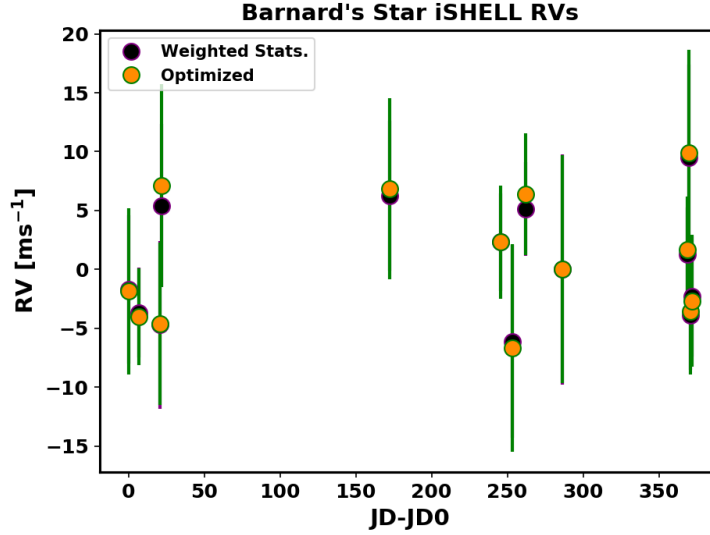


Figure 2.9: The best case multi-order RV combination that yielded the lowest RMS for Barnard’s Star for the full dataset. The unweighted standard deviation is  $5.13 \text{ m s}^{-1}$  for the optimized set. The weighted statistics formulation (Section 2.4.5) agrees well with the optimized RVs (Section 2.4.6). Hidden error bars are of similar size.

Table 2.5: The best single-order long-term RV precisions (unweighted standard deviation) for each of the four runs, and the corresponding best iteration. We only include the first 10 nights for 61 Cyg A in the calculation.

Image Order	Echelle Order	Barnard's Star (High $S/N$ ) [ $\text{ms}^{-1}$ ]	Iter	Barnard's Star (All) [ $\text{ms}^{-1}$ ]	Iter	GJ 15 A [ $\text{ms}^{-1}$ ]	Iter	61 Cyg A [ $\text{ms}^{-1}$ ]	Iter
5	216	-	-	19.02	10	50.07	32	16.68	31
6	217	15.87	28	13.68	33	32.39	15	32.92	40
7	218	13.95	9	16.25	12	3.61	32	13.17	15
8	219	11.66	20	10.68	23	7.39	32	9.48	16
9	220	18.05	7	14.50	40	6.59	13	15.14	39
10	221	16.53	27	17.15	21	8.36	18	19.32	32
11	222	15.10	23	14.93	24	4.81	40	10.95	26
12	223	21.11	40	16.59	6	17.38	34	11.99	12
13	224	12.99	40	27.16	25	9.39	12	11.88	20
14	225	29.20	19	33.23	33	13.38	6	24.46	18
15	226	16.17	17	11.19	21	9.07	15	30.22	19
16	227	16.22	40	15.44	16	20.88	6	27.24	6
17	228	31.07	14	28.14	15	7.34	26	26.85	34
18	229	-	-	28.91	40	127.77	18	488.75	6
19	230	-	-	25.14	23	49.54	17	475.78	6
20	231	-	-	27.34	24	48.82	11	96.62	7
21	232	-	-	20.17	22	67.97	14	895.76	6
22	233	-	-	49.28	40	89.55	40	240.85	6
23	234	-	-	46.82	40	90.12	18	124.50	9
24	235	-	-	41.13	15	42.95	6	60.39	14
25	236	-	-	68.48	27	132.62	40	195.59	6
26	237	-	-	45.51	40	95.76	16	67.75	21

Table 2.6: The best multi-order RVs for each target obtained through a powerset. The unweighted standard deviation  $\sigma$  and value of  $\chi^2_{red}$  of the measurements is noted.

JD-2457677	Nightly RV [ $\text{m s}^{-1}$ ]	Unc. [ $\text{m s}^{-1}$ ]
—Barnard’s Star (high $S/N$ ) (Orders 7-9, 11, 13), $\sigma = 4.33 \text{ m s}^{-1}$ , $\chi^2_{red} = 0.81$ —		
0.76914091	5.26	3.55
7.72960279	-1.70	5.17
21.71375211	-6.50	4.78
22.69412594	-1.20	5.43
173.07680052	4.89	7.68
246.08399455	-1.35	5.32
253.97949511	0.69	11.04
262.9147927	8.16	5.84
286.90298491	-2.39	8.42
—Barnard’s Star (All) (Orders 6-10, 14, 17, 20), $\sigma = 5.13 \text{ m s}^{-1}$ , $\chi^2_{red} = 0.61$ —		
0.76914091	-1.94	7.06
7.72960279	-4.02	4.11
21.71375211	-4.68	6.92
22.69412594	7.09	8.61
173.07680052	6.86	7.70
246.08399455	2.30	4.81
253.97949511	-6.65	8.81
262.9147927	6.35	5.19
286.90298491	-0.04	9.68
369.6983861	1.65	4.47
370.68776439	9.96	8.76
371.69478571	-3.60	5.38
372.68679116	-2.62	5.60
—GJ 15 A (Orders 8, 9, 10), $\sigma = 2.72 \text{ m s}^{-1}$ , $\chi^2_{red} = 0.50$ —		
0.82538026	2.81	5.93
1.83099163	-0.980	3.43
6.88132949	0.71	6.57
7.88033167	0.13	6.29
21.8549003	-5.16	3.80
22.86261265	2.92	4.24
—61 Cyg A <sup>1</sup> (Orders 8-9, 11-12, 17), $\sigma = 3.77 \text{ m s}^{-1}$ , $\chi^2_{red} = 0.71$ —		
0.79182255	-3.28	10.66
1.7336577	-0.65	11.27
6.8404918	-0.570	2.34
7.80991716	6.21	2.38
21.79603189	3.44	5.67
22.7468759	3.97	8.79
173.15354752	1.02	15.35
179.14649648	-0.10	23.62
246.12869699	-7.58	12.27
254.07051542	-2.45	4.30
263.01044249	1403.12	17.50

<sup>1</sup> Only the first ten nights are considered in any calculations for 61 Cyg A.

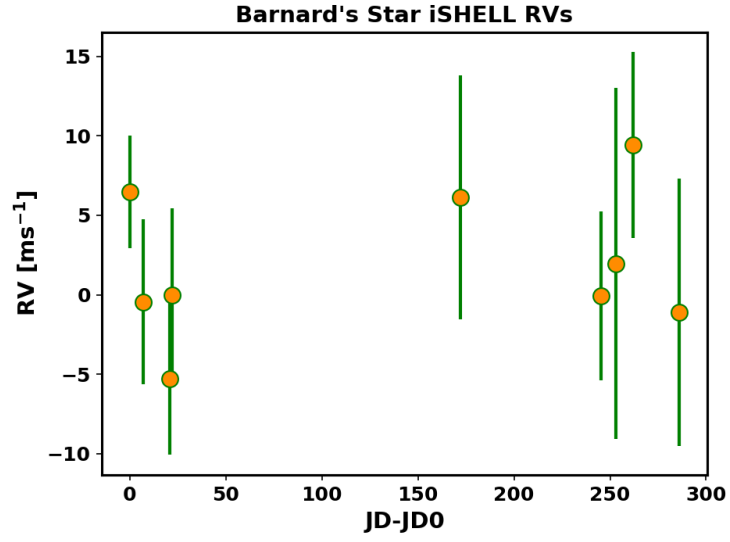


Figure 2.8: The best case multi-order RV combination that yielded the lowest RMS for Barnard's Star from the high  $S/N$  run. The unweighted standard deviation is  $4.33 \text{ m s}^{-1}$ . JD0 corresponds to the first nightly JD for each target given in table 2.6.

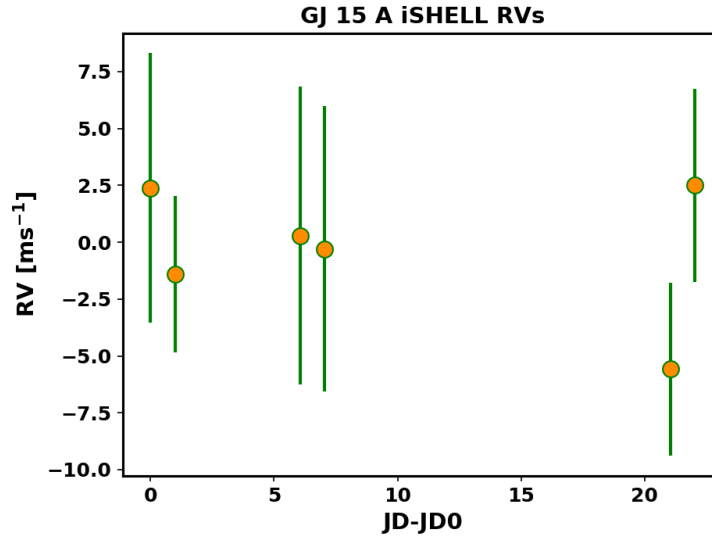


Figure 2.10: The best case multi-order RV combination that yielded the lowest RMS for GJ 15 A. The unweighted standard deviation is  $2.72 \text{ m s}^{-1}$ .

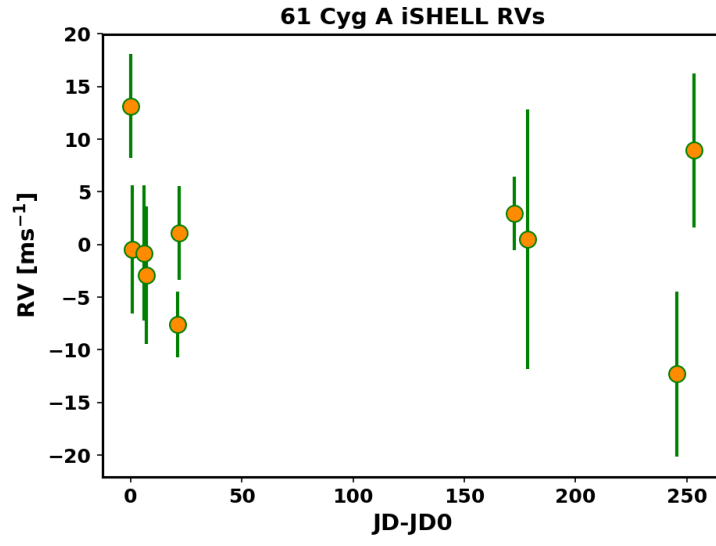


Figure 2.11: The best case multi-order RV combination that yielded the lowest RMS for 61 Cyg A. The unweighted standard deviation is  $3.77 \text{ m s}^{-1}$ . The last data point is not shown.

### 2.5.2 Error Analysis

We compare our obtained RV precisions with the expected analytic precision in the optimistic photon noise limit. Following (58), we compute a photon noise model precision:

$$\sigma_{\text{RV}} = c \left[ \sum_i \frac{(\lambda_i dA_i / d\lambda_i)^2}{A_i} \right]^{-1/2} \quad (2.25)$$

for both the convolved stellar template and gas cell used in our forward model, which we then add in quadrature to obtain a photon noise estimated RV precision. We do this for each order.  $A_i$  is the signal at pixel  $i$  given in photo-electrons (PEs). We adopt a peak  $S/N$  of 300 (per detector pixel) and gain of 1.8 to convert  $S/N$  to PEs<sup>5</sup>. This is performed on the data grid, ignoring cropped pixels. A  $\text{sinc}^{\sim 1.6}$  models the observed blaze function prior to flat-fielding sufficiently well, so we modulate the templates to approximately account for the lower  $S/N$  near the edges of the orders. We also convolve both templates with a Gaussian  $LSF$  with  $a_0 = 8$ , which is a representative  $LSF$  width in our model grid, and is roughly equal to one data pixel.

For GJ 15 A and 61 Cyg A, our nightly RV precision,  $\delta RV_{i,m}$ , is comparable to the photon noise estimate (Figs. 2.13, 2.14). Nightly scatter in RVs for Barnard’s Star are a few  $\text{ms}^{-1}$  above the photon noise estimate, even when ignoring the lower  $S/N$  data (Fig. 2.12).

Achieving this precision over long timescales is challenging due to other standard and non-standard sources in the RV error budget unaccounted for in the photon noise approximation. Known sources of external error arise from the fact that iSHELL is mounted at Cassegrain focus, and thus mechanically flexes as the telescope moves. Finally, iSHELL has a fringing source that will induce errors of  $> 10 - 20 \text{ ms}^{-1}$  if not modeled sufficiently, and  $> 50 \text{ ms}^{-1}$  if not modeled at all (23). Determining telluric induced error on RVs is the

---

<sup>5</sup>[http://irtfweb.ifa.hawaii.edu/~ishell/iSHELL\\_observing\\_manual.pdf](http://irtfweb.ifa.hawaii.edu/~ishell/iSHELL_observing_manual.pdf)

subject of a future investigation, but regions of large residuals are not found to be correlated with regions of high telluric absorption. We find that order 14 ( $m = 225$ ) is an outlier for all three targets, and suggests that the gas cell spectrum or telluric template is in error for this order.

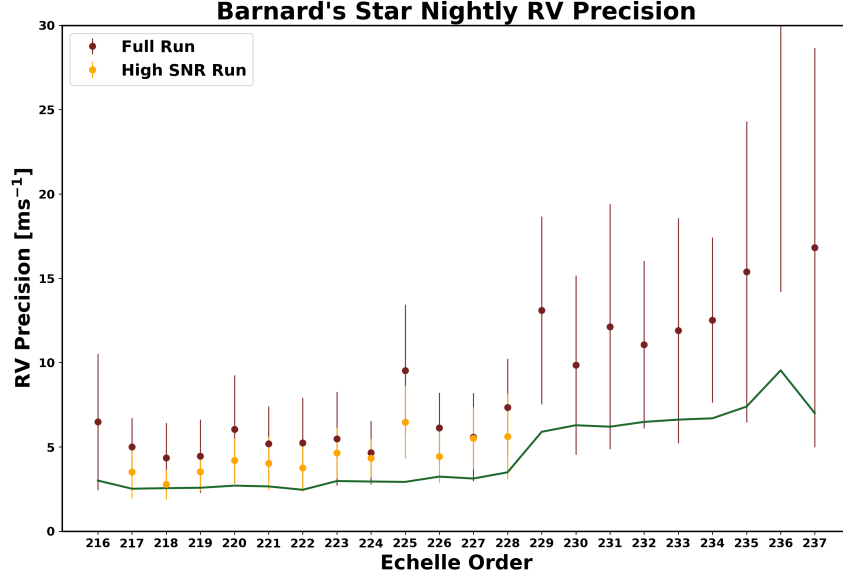


Figure 2.12: The nightly Barnard’s Star RV uncertainties for each order (markers), averaged over nights, alongside the estimated photon noise limit (solid line). Nights from the full data set are in red, and the high  $S/N$  run are shown in orange. The lower  $S/N$  data (last 4 nights) are ignored in generating this plot. Error bars represent a  $1\sigma$  spread of the uncertainties in the nightly RVs. Barnard’s Star nightly RV uncertainties are above the noise floor, unlike GJ 15 A and 61 Cyg A. Including lower  $S/N$  measurements can still impact nights at higher  $S/N$ s due to the common stellar template generation. The CO bandhead for cool stars starts at  $2.29 \mu\text{m}$  ( $m \leq 228$ ).



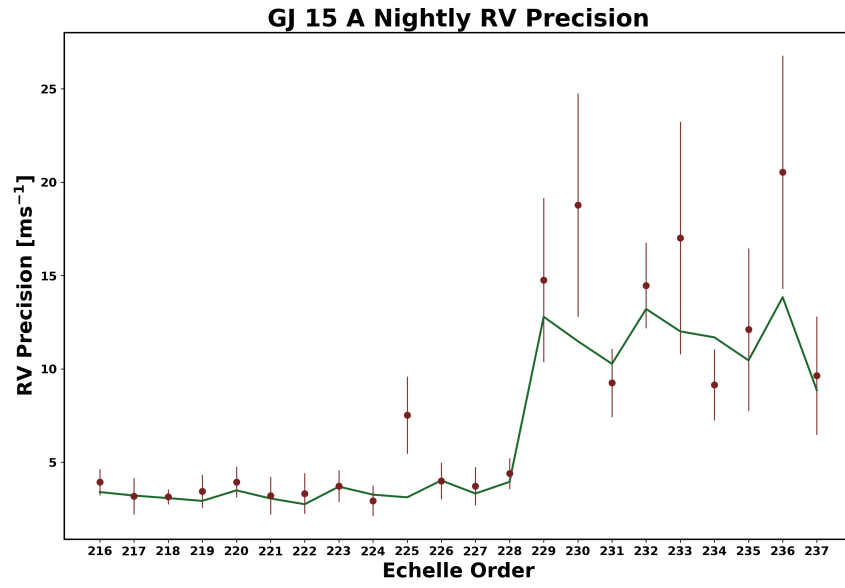


Figure 2.13: Same as Fig. 2.12, but for GJ 15 A.

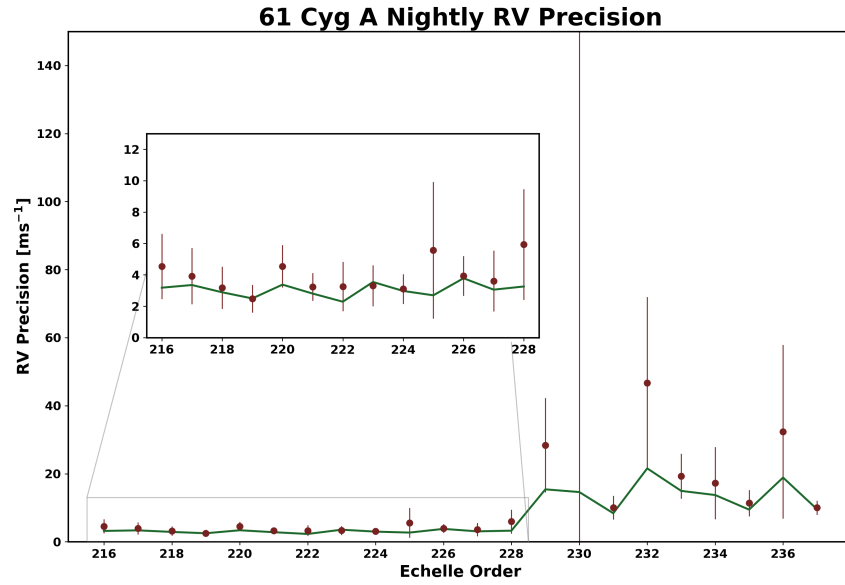


Figure 2.14: Same as Fig. 2.12, but for 61 Cyg A.

For our optimized multi-order RVs, we also compute the reduced chi-squared statistic given by:

$$\chi_{red}^2 = \frac{1}{\nu} \sum_i^{N_{\text{nights}}} \left( \frac{RV_i - \overline{RV_i}}{\delta RV_i} \right)^2 \quad (2.26)$$

where  $\nu = N_{\text{nights}} - 1$  corresponds to the largest possible degrees of freedom (59),  $\overline{RV_i}$  is the average RV of all nights weighted by  $1/\delta RV_i^2$ , and  $\delta RV_i$  is the uncertainty given by Eq. 2.22. By looking at all possible values of  $\sigma_{\text{RV}}$  from the powerset, we find for the high  $S/N$  Barnard’s run,  $\chi_{red}^2 = 1$  corresponds to approximately 4–6  $\text{ms}^{-1}$  (Fig. 2.15). When observing stars with unknown RVs, we do not have this freedom of picking the orders that lead to the lowest long-term  $\sigma_{\text{RV}}$ . However, when using at least 8 orders, less than 1 percent of  $\chi_{red}^2$  are less than 1. So, we can be confident in obtaining long-term multi-order precision of 5–7  $\text{ms}^{-1}$ , so long as we are using a sufficient number of orders and if the RV content allows for it, which will be the case for most K & M dwarfs, and late G dwarfs as well.

### 2.5.3 Stellar Template Generation

For each star and each order, a high resolution (8 times the data) deconvolved stellar template is obtained. For all orders, after a large number of iterations, randomly coherent noise eventually begins to accumulate in the stellar template, particularly for values near the continuum where the RV content is less, and especially near the edges where the  $S/N$  is relatively low. Additionally, the empirically derived template wavelength grid is still Doppler shifted by the unknown absolute RV of the star relative to the Solar system barycenter. This can be estimated by cross-correlating our empirically-derived template to a synthetic template. Examples of retrieved stellar templates are shown in figures 2.16–2.19.

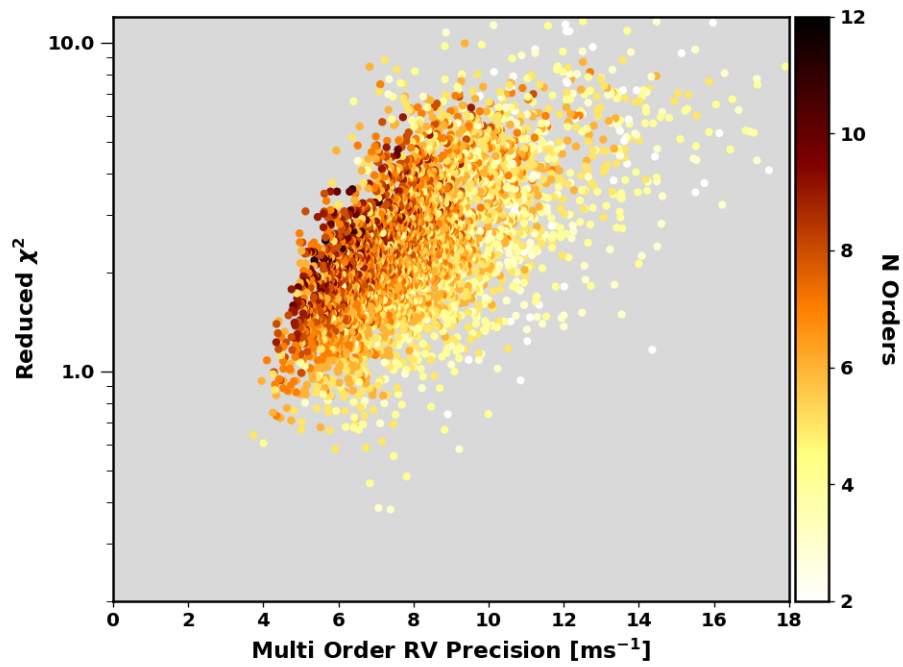


Figure 2.15: The corresponding values of  $\chi_{red}^2$  from all possible combinations of multi-order RVs. Points are colored according to the number of orders used for that combination, showing the expected improvement in RV precision by using increasing numbers of orders.

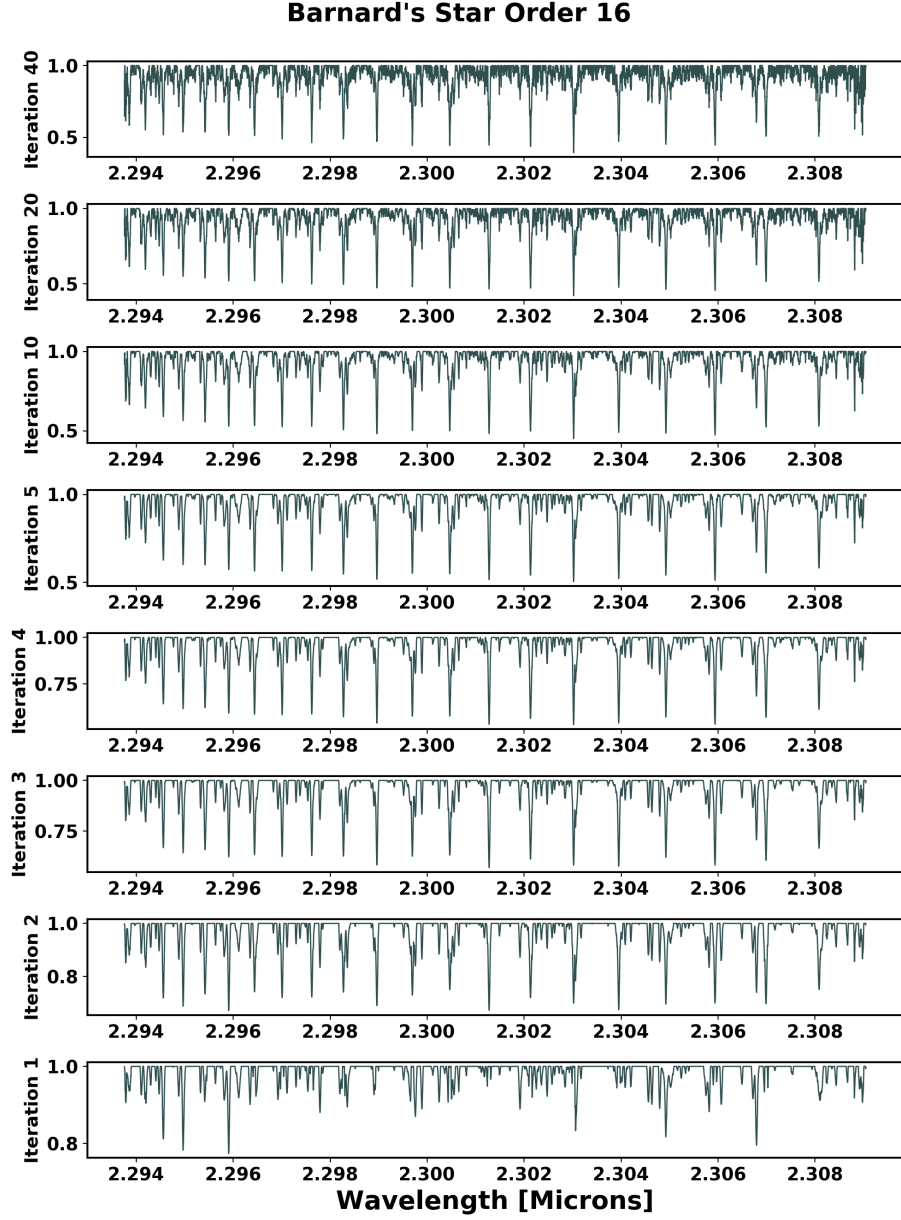


Figure 2.16: The generation of the stellar template for Barnard's Star for order 16 ( $m = 227$ ) for the high  $S/N$  run. Stellar features continue to get added to the template through early iterations, but a noisy continuum develops at later iterations, although RVs continue to improve.

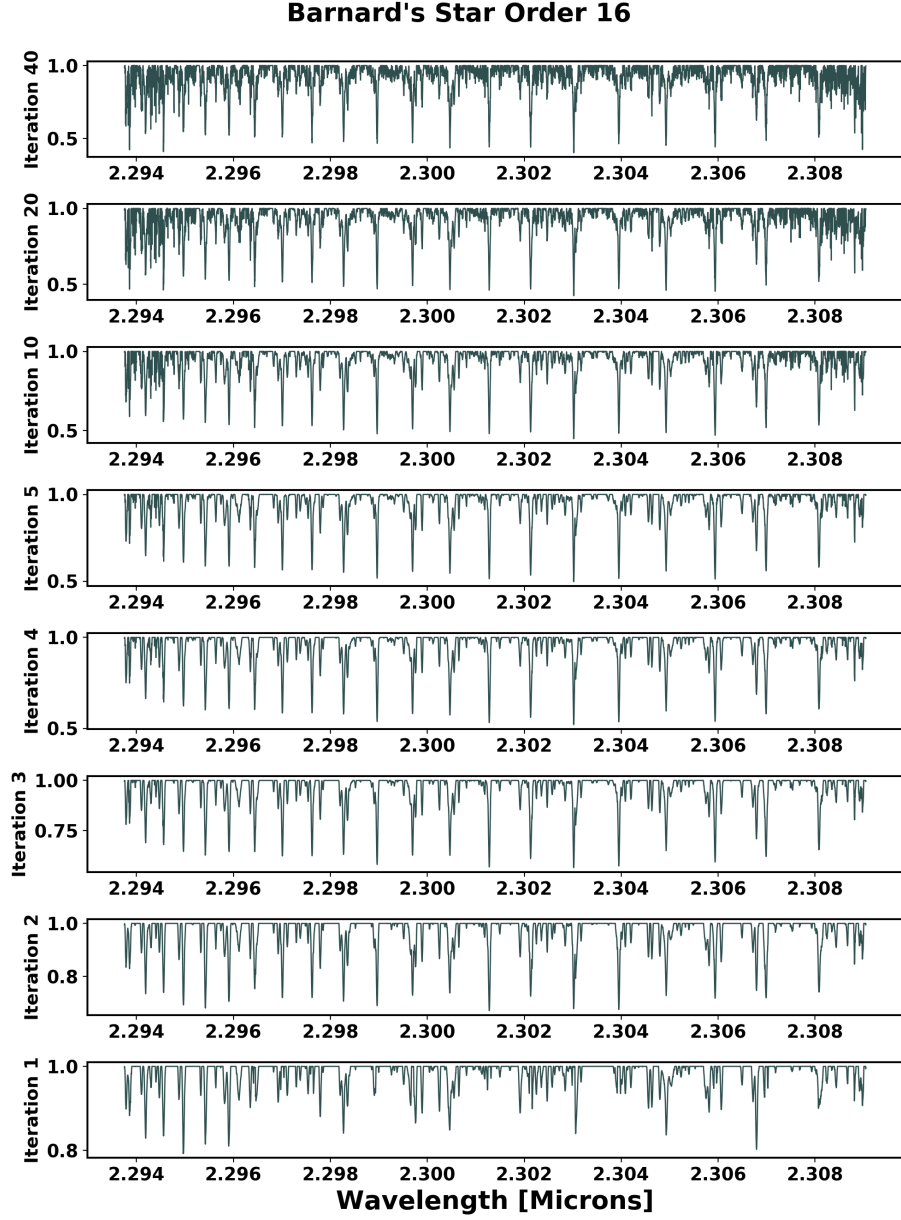


Figure 2.17: Same as Fig. 2.16, but using the full data set. The noisy continuum that develops at later iterations is worse at the edges compared to the high  $S/N$  run, because relatively lower  $S/N$  data is being used to generate the template, even though they are down-weighted.

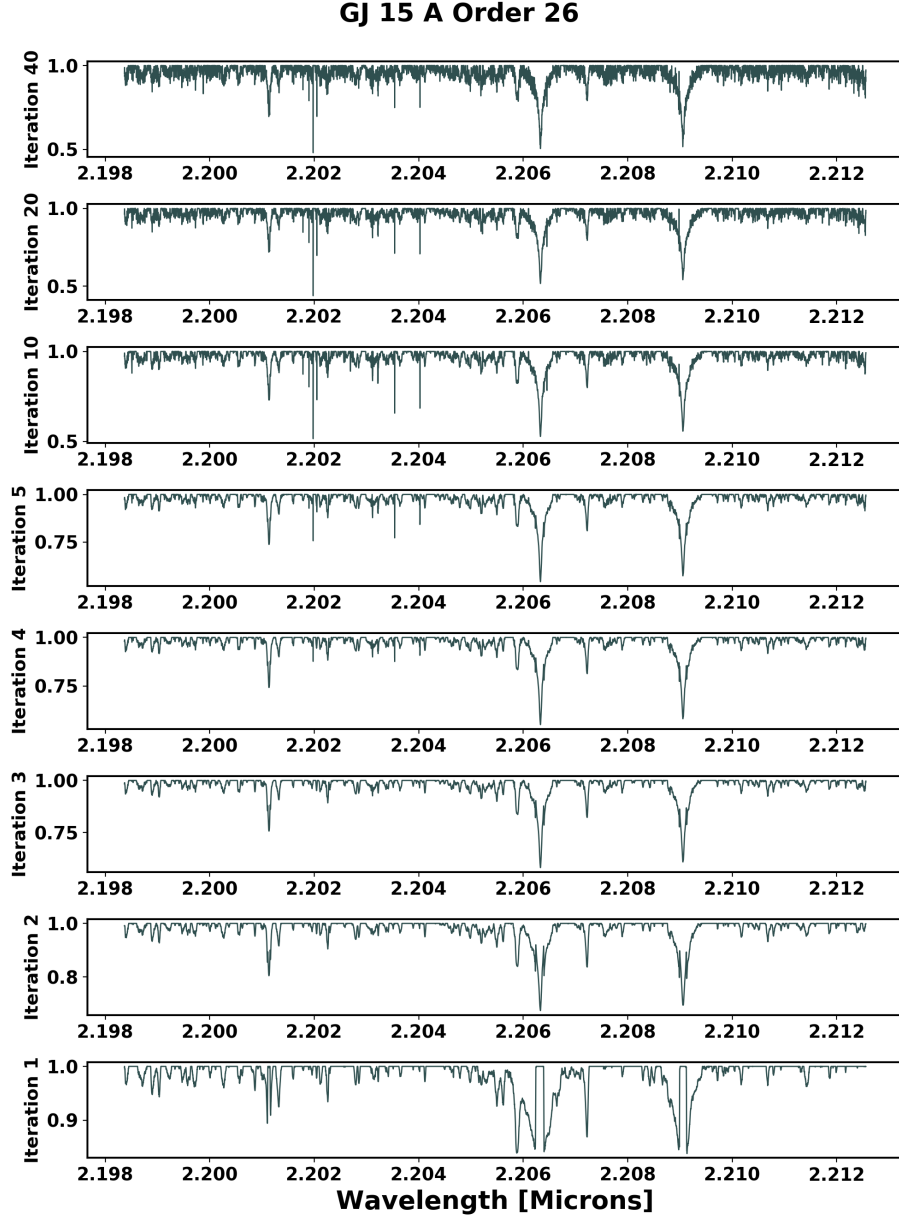


Figure 2.18: The generation of the stellar template for GJ 15 A for order 26 ( $m = 237$ ). The stellar RV information is less shortward the CO bandhead ( $< 2.29 \mu\text{m}$ ), but there are still broad lines from other molecules that can provide nightly RV precisions of  $10\text{--}20 \text{ m s}^{-1}$  (see fig. 2.13). Sharp lines like those found at  $2.202 \mu\text{m}$  are bad pixels.

### 61 Cyg A Order 13

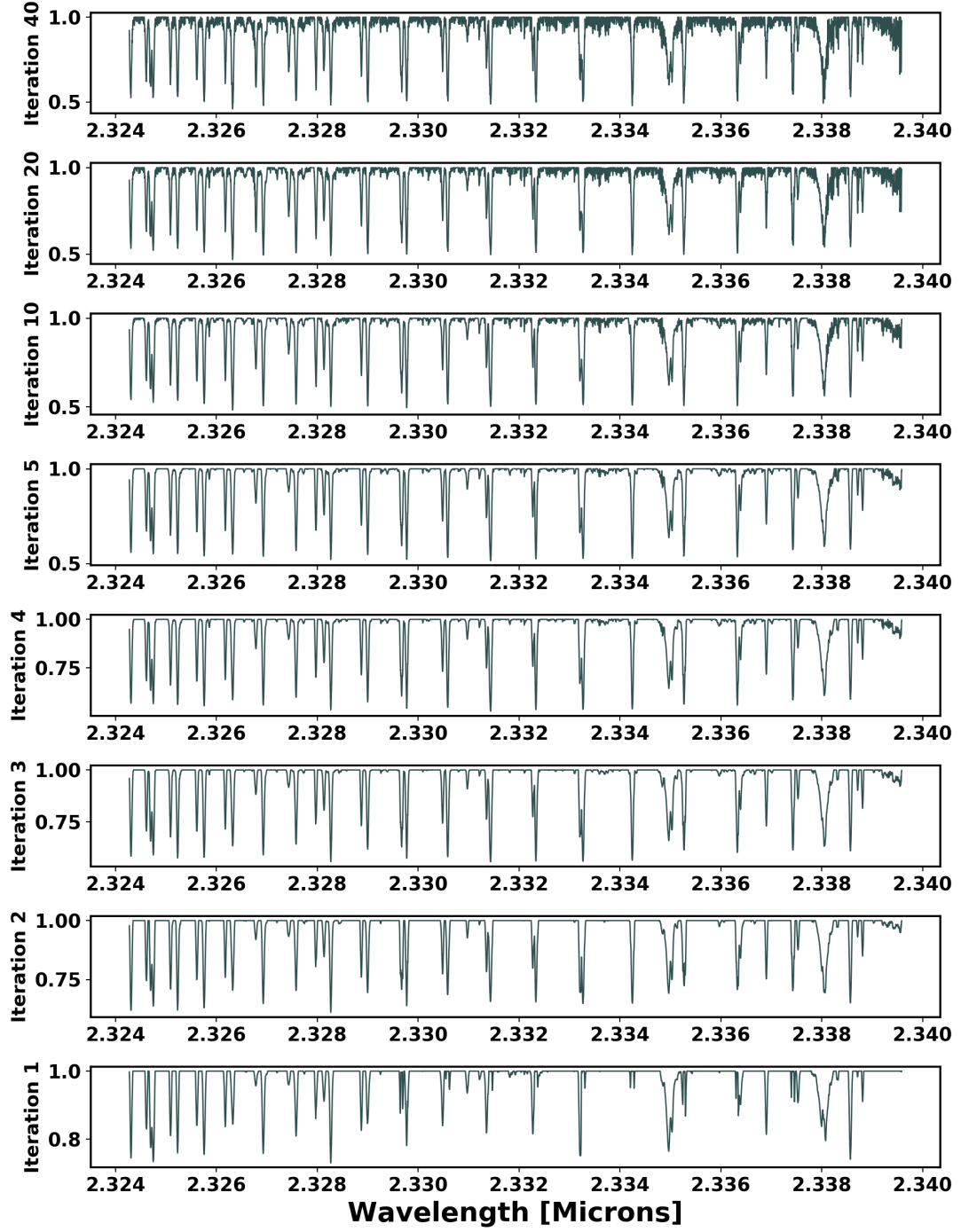


Figure 2.19: The generation of the stellar template for 61 Cyg A for order 16. K dwarfs also exhibit a strong CO bandhead past  $2.29 \mu\text{m}$ .

In our approach to extract heliocentric RVs, all spectra are compared to a common empirically-derived stellar template, and therefore we must be concerned whether or not our RV errors are caused by inherent astrophysical RV variability or internal errors in the stellar template spectrum itself. We do not quantitatively investigate the RV precision as a function of the number of epochs used in the analysis to identify a minimum number of epochs required for adequate barycenter velocity sampling in the stellar template derivation. Instead, in order to test how robust our stellar template retrieval is, we run two seasonal data sets of Barnard’s Star and compare the generated templates. We choose only the high  $S/N$  data set taken in October–November 2016 and the following high  $S/N$  data set taken from April–July 2017. We do this for order 13 which is high in stellar and gas RV content.

Qualitatively, we find that using fewer spectra in the analysis allow bad pixels to increasingly affect the template (Fig. 2.20). We find that it is critical in our analysis to flag bad pixels in the data or in the residuals on the data wavelength grid, because a single bad pixel gets spread out into many on the template grid due to the high resolution of the model. Additionally, we find that deep lines with high RV content are fairly consistent between the two seasons and the mismatches are typically found for values near the continuum (Fig. 2.21).



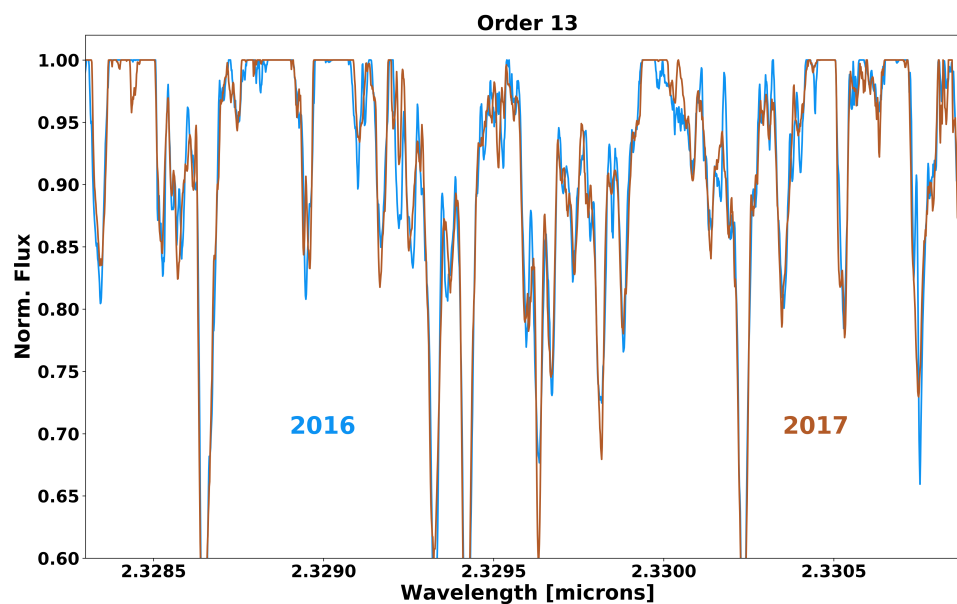


Figure 2.20: Two separately retrieved stellar templates for Barnard's Star (fall 2016, spring-summer 2017).

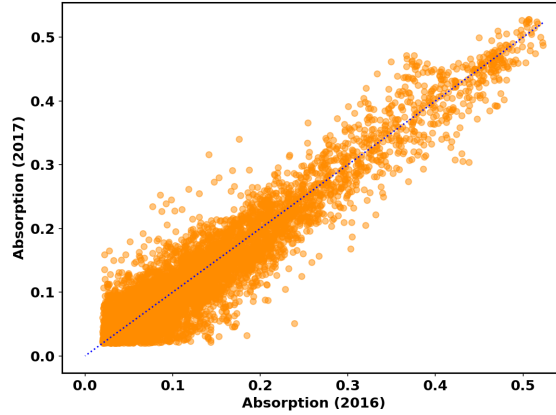


Figure 2.21: An absorption vs. absorption plot for two separately retrieved stellar templates for Barnard’s Star (fall 2016, spring-summer 2017). Only features deeper than 2% in both templates are shown. A one-to-one line corresponding to perfect agreement between the separately retrieved templates is shown in blue. The disagreement is slightly larger for values with less absorption (near the continuum).

## 2.5.4 Model Parameters

### Multi-Order Consistencies

The same set of forward model parameters are used for all orders (see table 2.4). We forward model all orders independently - e.g. the parameters derived from one order are not used to constrain the parameters for other neighboring orders, when in principle some parameters should be identical across orders or related by simple analytic approximations. Thus, we can investigate parameters that are consistent across orders as a sanity check on our analysis. For this Section, we use the high  $S/N$  Barnard’s Star run results. We find the telluric water and methane optical depths are consistent across orders (Fig. 2.22). Order 15 tends to require a systematically higher water optical depth compared to the other orders, indicating error in the synthetic telluric template at that wavelength.

The fringing parameters are not well-behaved across orders, but show clear nightly consistency (Fig. 2.23). The telluric shift shows a large scatter order to order relative to our RV precision, and is relatively more consistent intra-order across all nights (Fig. 2.23). This could be used in future work to refine our telluric template.

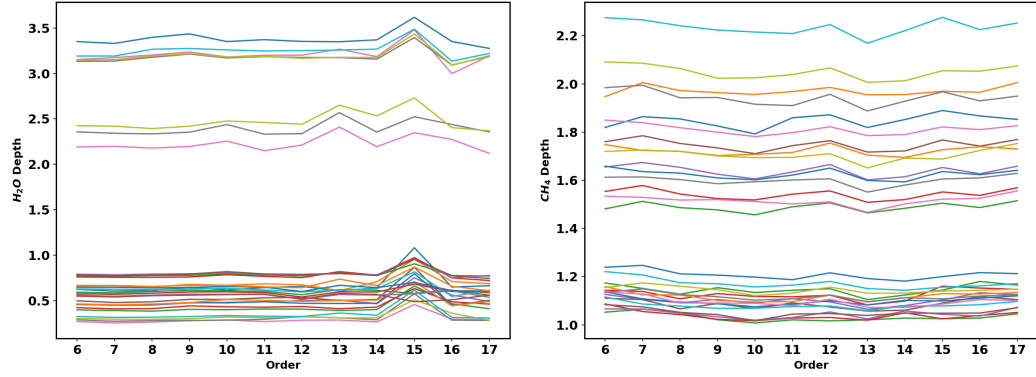


Figure 2.22: *Left*: The water optical depth for multiple orders from the high  $S/N$  run. *Right*: Same, but for telluric methane. Only every other observation is plotted. The water and methane depths are also unique supporting our hypothesis of variable atmospheric content.

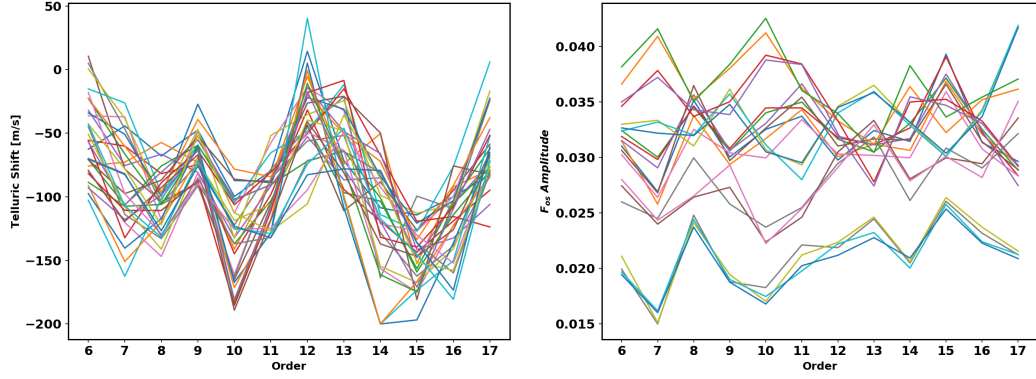


Figure 2.23: *Left*: Same as Fig. 2.22 but for the telluric shift. Nights within an order show less scatter in the fit telluric shifts than the scatter between orders. This implies that there is room for improvement in our telluric model components. *Right*: Same, but for the fringing amplitude. There is little inter-order agreement, but intra-night stability still allows for nights to cluster together.

## Correlations

Our choice of forward model implementation for the work presented here uses 48 parameters. We investigate parameters that are highly correlated with RVs or other parameters. Some parameters are expected to be correlated without concern. The quadratic wavelength solution Lagrange points are not orthogonal parameters, and are indeed strongly correlated with one another. We also find neighboring spline points to be correlated for the blaze and wavelength corrections and are not further discussed as they are also not orthogonal. Other correlated parameters are found through computing the Pearson linear correlation coefficient  $\rho$  defined in (60) for all pairs of parameters and for each order. Significant linear correlation or anti-correlation corresponds to  $\rho \rightarrow \pm 1$ . We calculate  $\rho$  for all pairs of parameters, including  $RV_\star$  for each spectrum. We flag all pairs of parameters such that  $|\rho| > 0.5$  for all orders (6-17) using the high  $S/N$  Barnard’s Star results. We find that the  $LSF$  width

$a_0$  is degenerate with even *LSF* Hermite terms  $a_j$  (odd terms are usually zero), despite being an orthogonal basis. We also find that the water optical depth is correlated with several parameters, but only consistently with the base (quadratic) wavelength solution points  $\lambda_i$  across multiple orders (Figs. 2.24, 2.25). Most of the water depth correlations are due to two nights with relatively high water vapor content/airmass. Otherwise, we find no other parameters with  $|\rho| > 0.5$  consistently across orders. A full correlation plot is shown in Fig. 2.24, and several examples of correlated parameters are shown in Fig. 2.25. We also check for correlation in the single-order nightly (co-added) RVs. We find neighboring orders are moderately correlated or anti-correlated, which is expected with the large spectral region of overlap, but find no other strong correlation (Fig. 2.26).

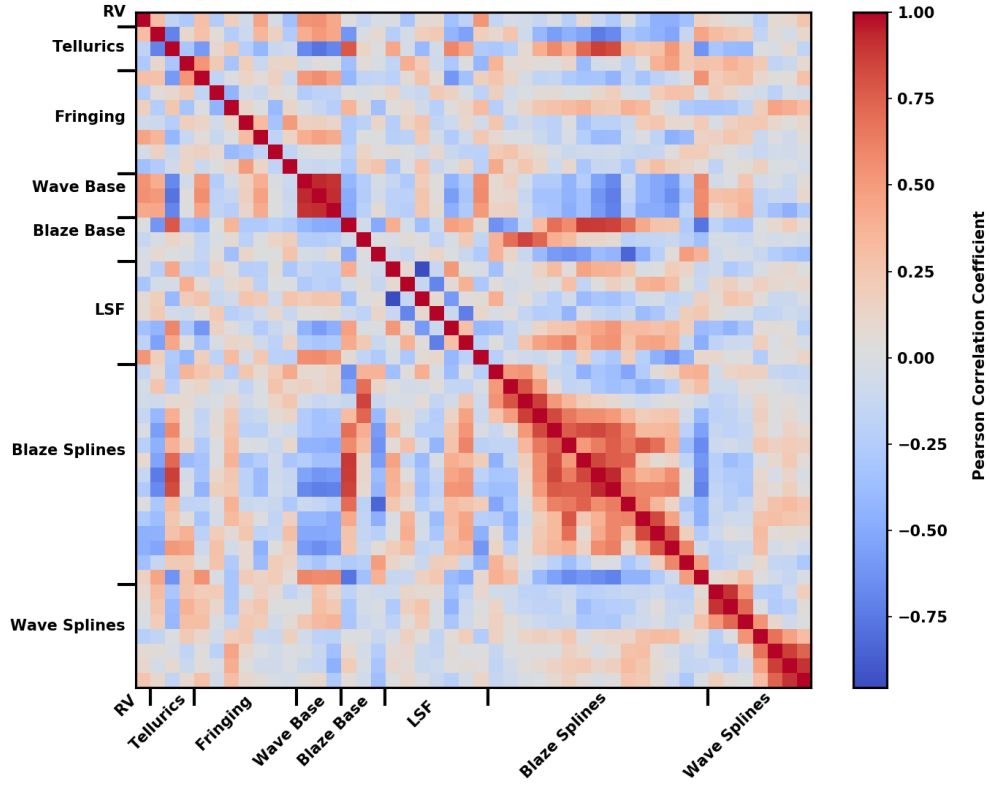


Figure 2.24: A correlation plot for all forward model parameters from order 8 ( $\text{CO}_2$  and  $\text{N}_2\text{O}$  are not considered here). Parameters are in the same order as given in table 2.4. Neighboring spline points for the blaze and wavelength solution are heavily correlated. Other orders exhibit qualitatively similar correlation plots. The first three parameters in the fringing block correspond to the OS fringing, while the remaining fringing parameters are used to model the originally misidentified sampling alias.

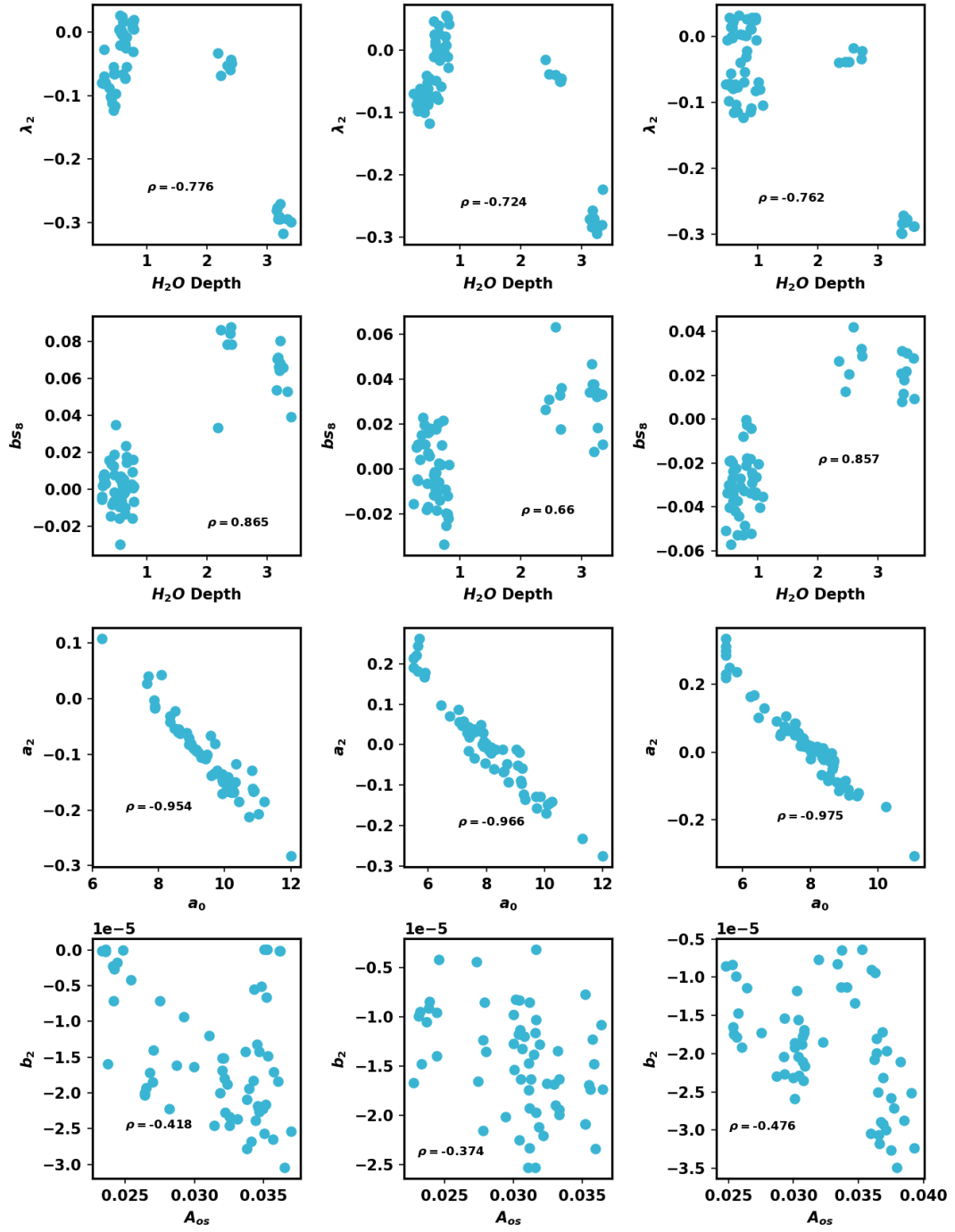


Figure 2.25: A series of correlation plots for orders 8, 13, & 15 (from left to right) highlighting strongly correlated parameters. Parameter symbols are defined in 2.4.

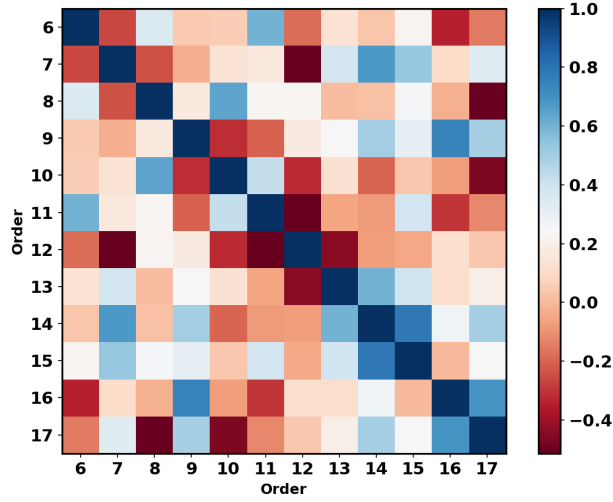


Figure 2.26: A correlation plot for the single-order nightly RVs from the Barnard’s star high  $S/N$  run. Each block is colored according to the value of the Pearson Correlation Coefficient. Neighboring orders (near the diagonal) are typically more correlated than orders further away, perhaps because they overlap in wavelength.

## 2.6 Discussion

With a complex forward model of 48 parameters, we investigate the benefits and drawbacks of our choice of parameter space. Proper analysis of our forward model requires a thorough analysis for each component, but here we only focus on the wavelength solution and  $LSF$ , as we identify they significantly impact the derivation of our RVs. Without a robust  $LSF$  and wavelength solution, the model breaks down and remaining parameters will fail to converge. We conclude the discussion with a comparison to other NIR RV spectrographs, methodologies, and prospects for planet confirmation.

### 2.6.1 Wavelength Solution

We expect the wavelength solution to be well-modeled by a quadratic, but considering both the non-ideal stability conditions for iSHELL and extremely fine RV measurements



being performed, there are good motives to try a wavelength solution that allows for local perturbations. To test this, we run several orders of Barnard’s Star from the high  $S/N$  data set with considerable stellar RV content using a various number of splines for the wavelength solution. For orders near the middle of the detector, the addition of splines can yield worse RV precision, but in most cases the RVs are improved (figures 2.27–2.28). Unfortunately, there is little agreement on the number of splines. However, we find the average spline corrections for all targets and orders are similar (order-to-order consistency), with most deviations occurring at the end points, further justifying the spline correction (fig. 2.29).

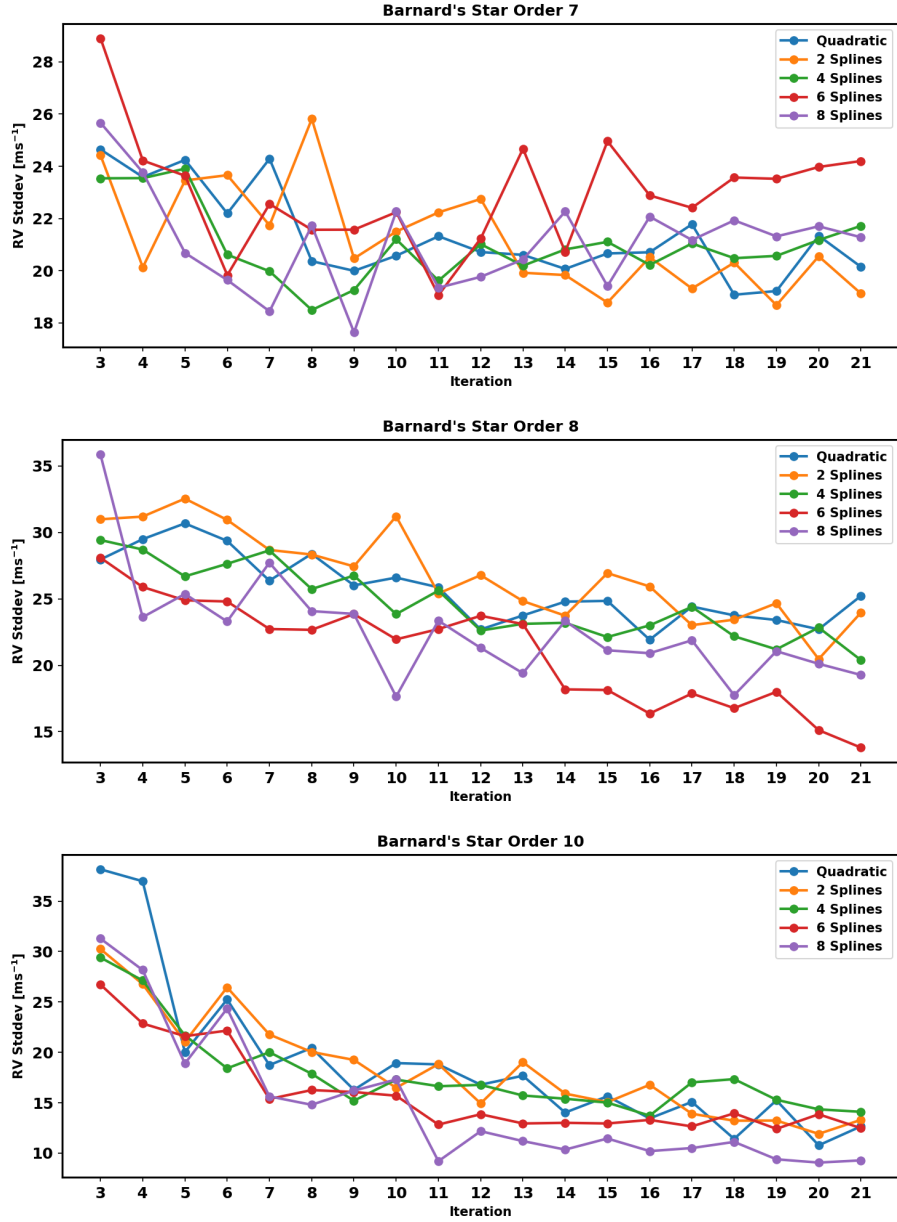


Figure 2.27: The obtained RV precision for Barnard's Star using different spline implementations for the wavelength solution for orders 7, 8, & 10 using the high  $S/N$  data set. Most orders show improvement when using splines, but the number of splines is inconsistent and can in some cases make RV precisions larger.

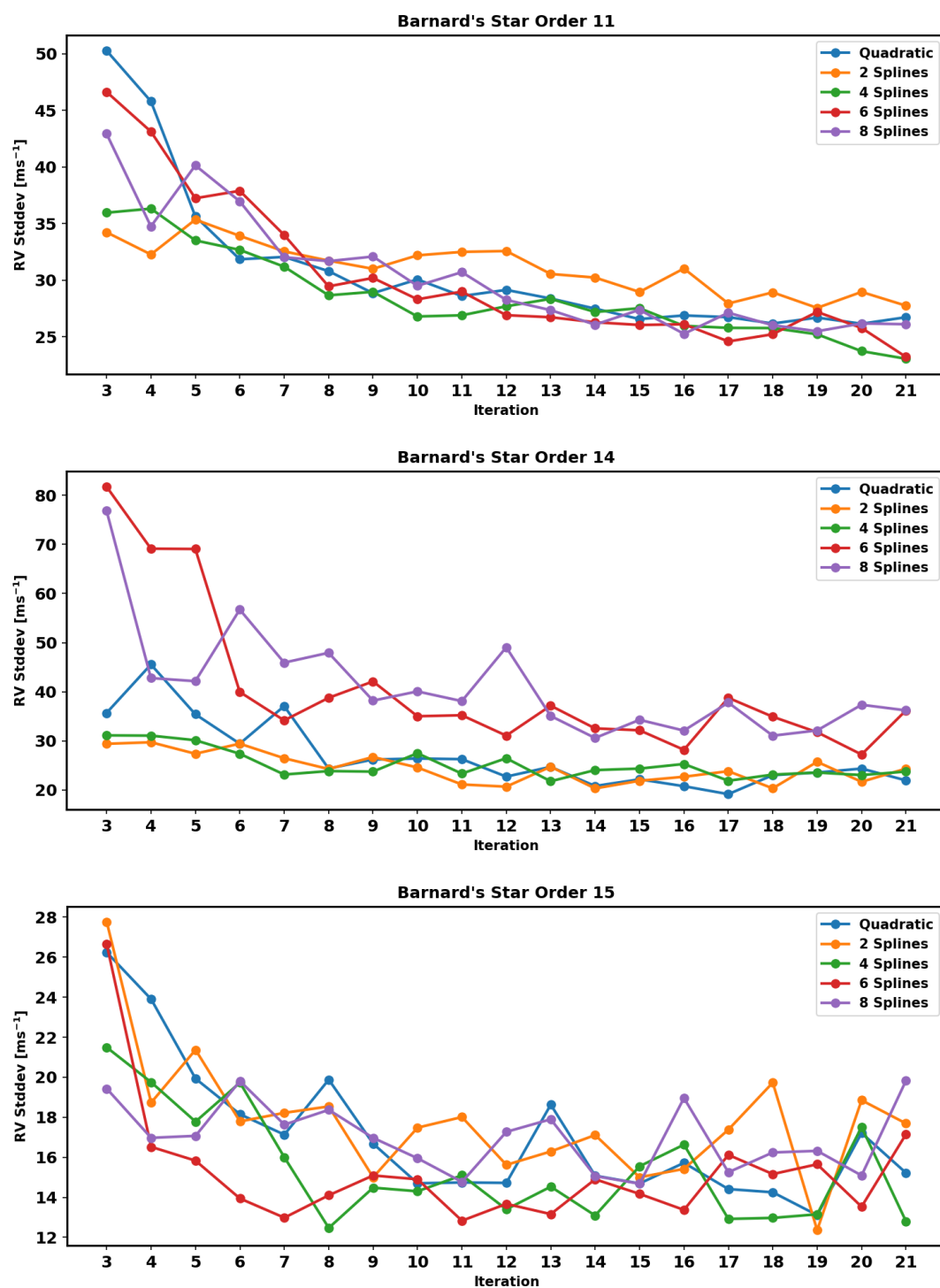


Figure 2.28: Same as Fig. 2.27 but for orders 11, 14, & 15.

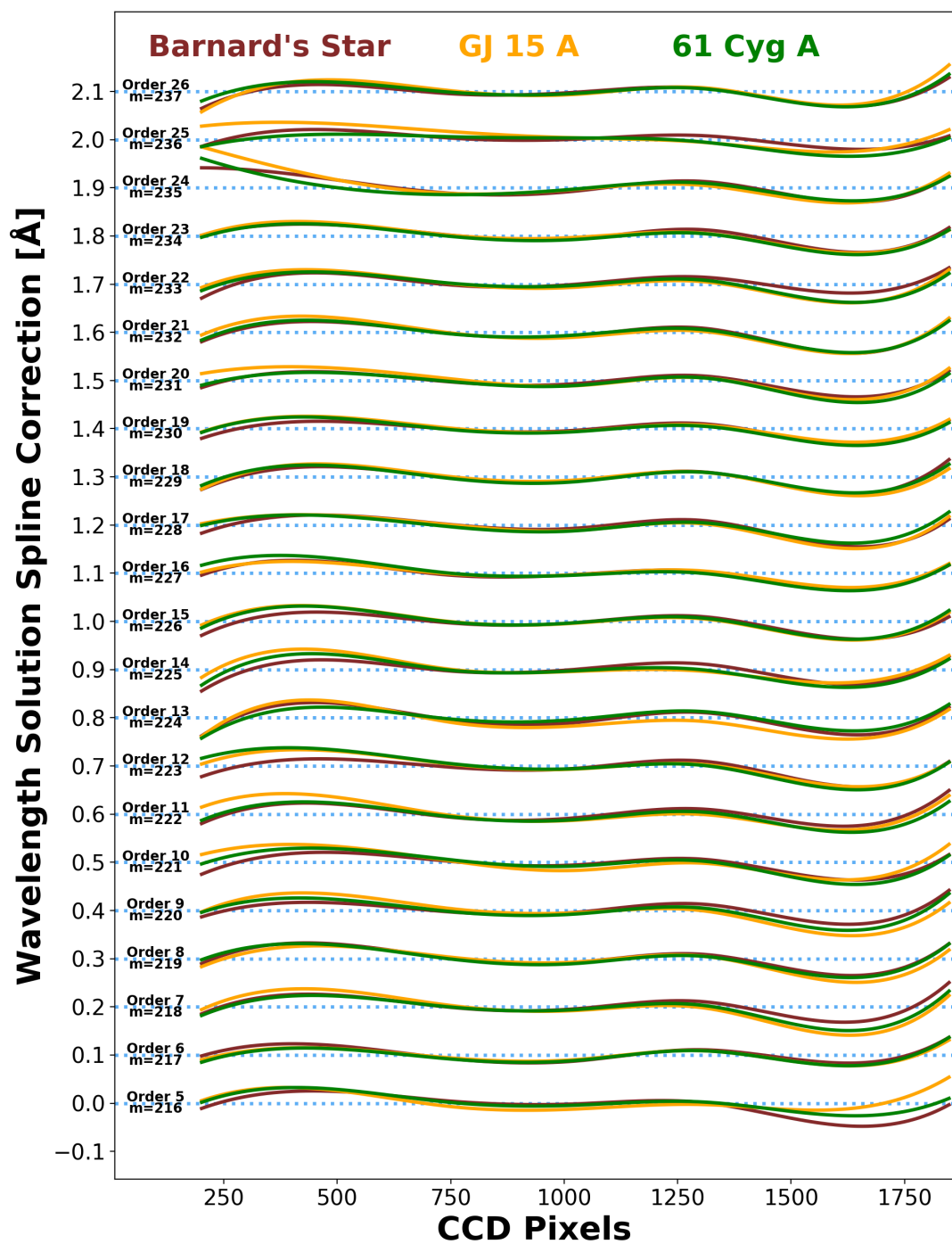


Figure 2.29: The average spline correction that gets added to a quadratic in the wavelength solution for all three runs (using the full data set for Barnard's Star). The average correction is approximately the same for all orders and targets, strengthening the case for including the correction.

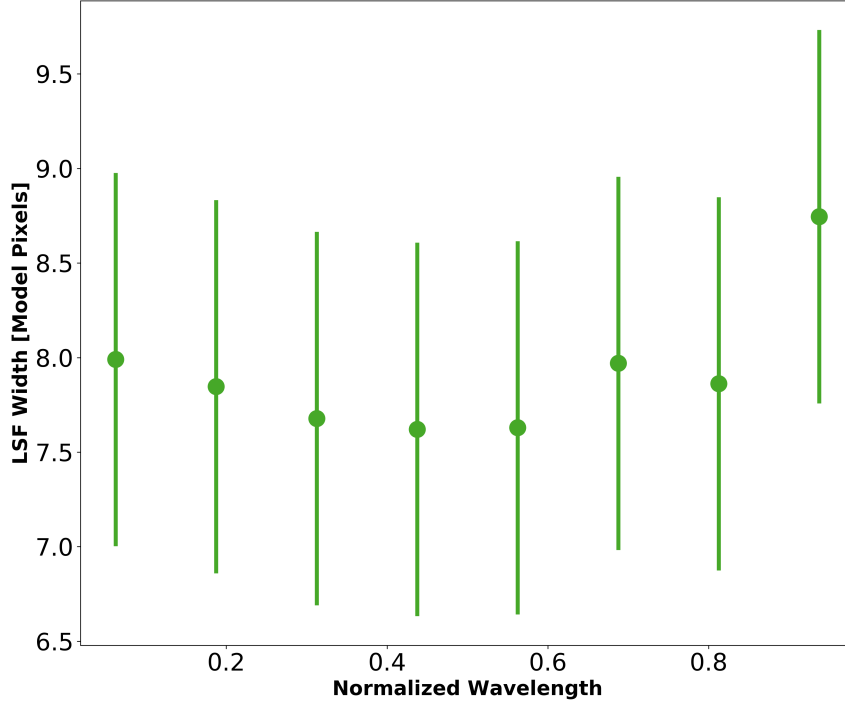


Figure 2.30: The  $LSF$  width across the detector for the cropped portion of the data (spectral pixels 200-1848). This data set is an average of the high  $S/N$  Barnard’s Star observations (61 spectra) and 6 echelle orders high in gas cell RV content (eq. 2.25). A higher order  $LSF$  model may over-compensate for a larger width on the ends of the detector (further from the blaze angle), so only a 3 Hermite term model was used. The error bars represent a  $1\sigma$  spread. The  $LSF$  width tends to be higher on the ends (especially the red end), but is generally consistent in the middle of the detector.

### 2.6.2 LSF Model

Like (23) with CSHELL, we assess different parameterizations of our  $LSF$  model. With iSHELL’s larger spectral grasp, we find that a varying  $LSF$  model within the order can improve the RMS in fitting. If the  $LSF$  truly is dynamic across a single-order, then it would be advantageous to allow for a unique  $LSF$  model at each model pixel using spline continuity relations, similar to the wavelength solution and blaze function. Unfortunately

this would be too computationally expensive having to compute over 16,000  $LSF$ 's for a single model. Further, there is no reason to use a finer  $LSF$  model than a single resolution element ( $\sim 0.03$  nm, or 3 detector pixels). The downside of a binned  $LSF$  is it drastically increases the number of model parameters and therefore runtime. Further, from the limited number of cases performed with a dynamic  $LSF$ , we find that this degrades RV precision. A 3 Hermite term model with 8 equally sized bins across the detector (Fig. 2.30) typically yields  $\sim 5 \text{ m s}^{-1}$  higher single-order RV precision, while a 7 Hermite term model (8 bins) is anywhere from 0–10  $\text{m s}^{-1}$  worse on average. Since it is possible to over-fit the data, a lower RMS from a more complex  $LSF$  model does not necessarily lead to the lowest RV precision.

### 2.6.3 Other NIR Precise RV Instruments & Methodologies

We compare our results with other on-sky NIR precise RV spectrographs. Early instruments like NIRSPEC (61) on Keck were capable of 40–50  $\text{m s}^{-1}$  precisions using tellurics as a wavelength reference and were mostly limited by the smaller spectral resolution of  $R \sim 25,000$  (22). The CRIRES (62) spectrograph on the VLT obtained 5  $\text{m s}^{-1}$  long-term RVs at K-band using an ammonia gas cell for wavelength calibration, and was primarily limited by imperfect modeling of telluric lines (24). The Habitable Zone Planet Finder (HPF) spectrograph (Y- & J-band) on the 10 meter Hobby-Eberly telescope has reached  $< 3 \text{ m s}^{-1}$  long-term precisions on Barnard's Star (26). Unlike iSHELL which uses a gas cell to serve as a common optical path wavelength reference, HPF uses a laser frequency comb providing a series of evenly spaced emission lines to serve as a wavelength reference (25). The CARMENES instrument utilizes two spectrographs (visible and J-, Y-band) with the goal of characterizing stellar activity through analyzing the color (wavelength) dependence on RVs. The visible arm has shown 1–5  $\text{m s}^{-1}$  is possible (27), but the NIR is still impacted by the mitigation of tellurics using the CCF method and the lower than expected (from synthetic spectra) RV information content in the Y- and J-bands (63).

While not used here, the `wobble` pipeline (56) is a second data-driven technique to retrieve  $I_*$  and has shown notable precision at optical wavelengths further validating our approach. In their work, an initial template is determined using a similar method we outline above, but is then treated as a high resolution grid of values to be optimized. The grid must be the same for all spectra, but each is then Doppler shifted with a unique  $\Delta v$ . This implies all spectra are optimized simultaneously with a single likelihood function, although the temporal variations are fit separately.

#### 2.6.4 Prospects for iSHELL Planet Confirmation

With the launch of the NASA *TESS* (Transiting Exoplanet Survey Satellite) mission, there will be a plethora of planet candidates needing RV follow-up to constrain the mass, and therefore density of the planets. Given our demonstrated precision, many of these candidates orbiting K and M dwarfs brighter than  $K_{\text{mag}} = 9$  and with velocity semi-amplitudes  $>3 \text{ m s}^{-1}$  will be detectable with iSHELL. From the existing list of objects of interest<sup>6</sup> that meet this brightness and predicted semi-amplitude criteria, and the total estimated yield from (64), we estimate  $\approx 100$  candidates will be amenable to follow-up with iSHELL.

With its unique wavelength coverage, iSHELL measurements will provide a valuable window to confirm planets around K and M dwarfs, particularly those that are more magnetically active and less amenable to confirmation at visible wavelengths. To first order, we expect RV variations induced by stellar activity from stellar rotation modulated spots and plagues to be reduced in amplitude in the NIR w.r.t. to the visible by a factor proportional to the frequency ratio (21). For example, a star with  $5 \text{ m s}^{-1}$  stellar activity in the visible may be reduced to  $<1.5 \text{ m s}^{-1}$  in the NIR, improving sensitivity to planets with velocity semi-amplitudes of  $\sim 1\text{--}10 \text{ m s}^{-1}$ .

---

<sup>6</sup><https://tess.mit.edu/toi-releases/>

## 2.7 Summary & Future Improvements

We have developed a data analysis pipeline that can robustly extract RVs from K-band spectra taken with the iSHELL spectrograph on the NASA IRTF using a  $^{13}\text{CH}_4$  gas cell as a wavelength reference. By iteratively minimizing the RMS between the model and observed spectrum, we retrieve both the best-fit RVs as well as a deconvolved high-resolution spectrum of the star. The model uses 48 parameters and accounts for our gas cell, tellurics, fringing, blaze,  $LSF$ , and wavelength solution. Our initial efforts have shown  $5 \text{ m s}^{-1}$  precision for Barnard’s Star and 61 Cyg A over a  $\sim 1$  year baseline, and  $3 \text{ m s}^{-1}$  for GJ 15 A over one month. We note a summary of accomplishments shown in this chapter below. Further improvements to our RV forward model will be explored in future work.

1. Achieve  $5 \text{ m s}^{-1}$  RV precision over 1 year with
  - A unique calibration source at an unfrequented wavelength range for precise RV work,
  - A spectrograph that slews with the telescope at Cassegrain focus,
2. In the presence of
  - Deep and dynamic telluric lines across entire spectral orders,
  - A prominent fringing signal, sophisticating an already high-dimensional forward model,
  - Starting from the assumption of an unknown stellar template.



## Chapter 3: Chromatic Radial Velocities of the Young AU Mic Planetary System

In this chapter, we present a detailed radial velocity analysis of the AU Mic system. AU Mic is a young (22 Myr) early M dwarf known to host two transiting planets -  $P_b \sim 8.46$  days,  $R_b = 4.38^{+0.18}_{-0.18} R_\oplus$ ,  $P_c \sim 18.86$  days,  $R_c = 3.51^{+0.16}_{-0.16} R_\oplus$ . With visible RVs from CHIRON, HIRES, TRES, HARPS, MINERVA-Australis, and CARMENES-Vis, as well as near-infrared (NIR) RVs from NIRSPEC, CSHELL, IRD, CARMENES-NIR, iSHELL and SPIRou, we provide a  $5\sigma$  upper limit to the mass of AU Mic c of  $M_c \leq 20.13 M_\oplus$  and present a refined mass of AU Mic b of  $M_b = 20.12^{+1.72}_{-1.57} M_\oplus$ . Used in our analyses are a new RV modeling toolkit to exploit the wavelength dependence of stellar activity present in our RVs via wavelength-dependent Gaussian processes. By obtaining near-simultaneous visible and near-infrared RVs, we also compute the temporal evolution of radial-velocity “color” and introduce a regression method to aid in isolating Keplerian from stellar activity signals when modeling RVs in future works. Using a multi-wavelength Gaussian process model, we demonstrate the ability to recover injected planets at  $5\sigma$  significance with semi-amplitudes down to  $\approx 10 \text{ m s}^{-1}$  with a known ephemeris, more than an order of magnitude below the stellar activity amplitude. However, we find that the accuracy of the recovered semi-amplitudes is  $\sim 50\%$  for such signals.

### 3.1 Introduction

Characterizing young planetary systems is key to improving our understanding of their formation and evolution. Young transiting systems in particular offer a means to directly probe the radii, and together with masses from precise radial-velocity (RV) measurements,

the bulk densities of the planets. RV observations are also crucial to constrain the eccentricity of the orbit to understand the kinematic history and stability of the system. A precision of 20% for the mass determination is further recommended for enabling detailed atmospheric characterization, particularly for terrestrial-mass planets (65).

Unfortunately, searches for planets orbiting young stars have been limited by stellar activity signals comparable in amplitude to that of typical Keplerian signals. Stellar surface inhomogeneities (e.g., cool spots, hot plages) driven by the dynamic stellar magnetic field rotate in and out of view, leading to photometric variations over time. The presence of such active regions breaks the symmetry between the approaching and receding limbs of the star, introducing RV variations over time as well (66). These active regions further affect the integrated convective blue-shift over the stellar disk, and will therefore manifest as an additional net red- or blue-shift (67; 68). Various techniques have been introduced to lift the degeneracy between activity- and planetary-induced signals in RV datasets such as line-by-line analyses (69; 70; 71) and Gaussian process (GP) modeling (e.g., 3; 72; 73; 74; 75; 76; 77), but such measurements remain challenging due to the sparse cadence of typical RV datasets compared to the activity timescales.

AU Mic is a young (22 Myr; 78), nearby ( $\beta$  Pictoris moving group,  $\sim 10$  pc; 79), and active pre-main-sequence M1 dwarf (77). AU Mic hosts an edge-on debris disk (80), and therefore the probability for planets to transit is greater than for other systems. Using photometric observations from *TESS* (81) in Sector 1 (2018-July-25 to 2018-August-22), (77) (hereafter referred to as P20) discovered an  $\approx 8.46$  day Neptune-size ( $R_b = 4.38^{+0.18}_{-0.18} R_{\oplus}$ ) transiting planet, which was further validated to transit with *Spitzer* observations (hereafter referred to as AU Mic b). P20 also reported the detection of a single-transit event in the *TESS* Sector 1 light curve, but did not constrain the period with only an isolated event. With high cadence RVs from SPIRou, (3) (hereafter referred to as K21) measured the mass of AU Mic b and confirmed it to be consistent with a Neptune-mass planet ( $M_b = 17.1^{+4.7}_{-4.5} M_{\oplus}$ ). With more observations of AU Mic from the *TESS* extended mission in Sector 27 (2020-July-04 to 2020-July-30), (2) (hereafter referred to as M20) determined

AU Mic c to be a smaller Neptune-sized planet ( $R_c = 3.51^{+0.16}_{-0.16} R_{\oplus}$ ) with a period of  $\approx 18.86$  days.

## 3.2 Observations

### 3.2.1 RVs

Our analyses make use of new and archival high-resolution echelle spectra from a variety of facilities, which are summarized in Table 3.1. We briefly detail new spectroscopic observations and the corresponding RVs from observing programs primarily intended to characterize the AU Mic planetary system.

#### Minerva-Australis

Spectroscopic observations of AU Mic were carried out using the MINERVA-Australis facility situated at the Mount Kent Observatory in Queensland, Australia (82; 83; 84) between 2019 July 18 and 2019 November 5. MINERVA-Australis consists of an array of four independently operated 0.7 m CDK700 telescopes, three of which were used in observing AU Mic. Each telescope simultaneously feeds stellar light via fiber optic cables to a single KiwiSpec R4-100 high-resolution ( $R \sim 80,000$ ) spectrograph (85) with wavelength coverage from 480 to 620 nm. In total, we obtained 31 observations with telescope 3 (M-A Tel3), 35 observations with telescope 4 (M-A Tel4), and 33 observations with telescope 6 (M-A Tel6). Exposure times for these observations were set to 1800 s, providing a signal-to-noise ratio between 15 and 35 per spectral pixel. RVs are derived for each telescope by using the least-squares shift and fit technique (86), where the template being matched is the mean spectrum of each telescope. Spectrograph drifts are corrected for using simultaneous thorium-argon (ThAr) arc lamp observations.

## CARMENES

The CARMENES (Calar Alto high-Resolution search for M dwarfs with Exo-earths with Near-infrared and optical echelle Spectrographs) instrument (87) is a pair of two high-resolution spectrographs installed at the 3.5 m telescope at the Calar Alto Observatory in Spain. The visual (Vis) and near-infrared (NIR) arms cover a wavelength range of 520–960 nm and 960–1710 nm, with resolving powers of  $R=94,600$  and  $R=80,400$ , respectively. AU Mic was observed 100 times with CARMENES during two different campaigns between 14 July and 9 October 2019, and between 19 July and 16 November 2020, respectively. This last observing period was partially contemporaneous with *TESS* observations of AU Mic in Sector 27 (04 July – 30 July 2020). One or two exposures of 295 s were obtained per epoch with typical  $S/N$  larger than 70–100, and at airmasses larger than 2.5, due to the low declination of the target at the Calar Alto observatory. CARMENES data were processed by the *caracal* pipeline (88), which includes bias, flat-field, and dark correction, tracing the echelle orders on the detector, optimal extraction of the one-dimensional spectra, and performance of the initial wavelength calibration using U-Ar, U-Ne, and Th-Ne lamps. The RVs were obtained with the **SERVAL** pipeline (89) by cross-correlating the observed spectrum with a reference template constructed from all observed spectra of the same star. In addition, the **SERVAL** pipeline also computes the correction for barycentric motion, secular acceleration, instrumental drift using simultaneous observations of Fabry-Pérot etalons, and nightly zero-points using RV standards observed during the night (90).

## IRD

We obtained near infrared, high resolution spectra of AU Mic using the InfraRed Doppler (IRD) instrument (e.g., 91) on the Subaru 8.2 m telescope. The observations were carried out between June – October 2019, and we obtained a total of 430 frames with integration times of 30–60 seconds. Half of these frames were taken on the transit night (UT 2019 June 17) with the goal of measuring the stellar obliquity for AU Mic b, whose RVs were already presented in (92). The raw data are reduced in a standard manner using our custom

code as well as IRAF (93), and the extracted one-dimensional spectra are analyzed by the RV-analysis pipeline for IRD as described in (94). The typical precision of the derived RVs is 9–13 m s<sup>-1</sup>.

## HIRES

We include 60 Keck-HIRES (95) observations of AU Mic in our analyses. The majority of these observations took place in the second half of 2020 with several nights yielding contemporaneous observations with other facilities. Exposure times range from 204–500 seconds, yielding a median  $S/N \approx 234$  at 550 nm per spectral pixel. HIRES spectra are processed and RVs computed via methods described in (96).

## TRES

We include 85 observations (archival and new) of AU Mic observed with the Tillinghast Reflector Echelle Spectrograph (TRES; 97; 98) in our analyses. The majority of these observations took place in the second half of 2019 with several nights yielding contemporaneous observations with other facilities. Typical exposure times range from 600–1200 seconds, with a median  $S/N \approx 60$  per resolution element. Spectra are processed using methods outlined in (99) and (100), with the exception of the cross-correlation template, for which we use the high- $S/N$  median observed spectrum.

## iSHELL

We obtained 46 out-of-transit observations of AU Mic with iSHELL on the NASA Infrared Telescope Facility (101) from October 2016 to October 2020. The exposure times varied from 20–300 seconds, and the exposures were repeated 2–23 times within a night to reach a cumulative  $S/N$  per spectral pixel  $> 200$  (the approximate center of the blaze for the middle order, 2.35  $\mu\text{m}$ ) for most nights. Raw iSHELL spectra are processed in `pyshell` using methods outlined in (45).

The corresponding iSHELL RVs are computed in `pychell` using updated methods to those described in (45). Instead of starting from an unknown (flat) stellar template, we start with a BT-Settl (102) stellar template with  $T_{eff} = 3700$  K, and with solar values for  $\log g$  and Fe/H. We further Doppler-broaden the template using the `rotBroad` routine from `PyAstronomy` (103) with  $v \sin i = 8.8 \text{ km s}^{-1}$ . Qualitatively, this broadened template matches the iSHELL observations well. We also “iterate” the template by co-adding residuals in a quasi-inertial reference frame with respect to the star according to the bary-center velocities ( $v_{BC}$ ), however the stellar RVs for subsequent iterations tend to be highly correlated with  $v_{BC}$  and exhibit significantly larger scatter than the first iteration suggests. We therefore use RVs from the first iteration only and leave the cause of this correlation as a subject for future work.

## CHIRON

We obtained 14 nightly observations of AU Mic with the CHIRON spectrometer (91) on the SMARTS 1.5 m telescope at the Cerro Tololo Inter-American Observatory (CTIO) between UT dates 2019-09-14 and 2019-11-10. Observations are recorded in narrow slit mode ( $R \sim 136,000$ ) using the iodine cell to simultaneously calibrate for the wavelength scale and instrument profile. Like iSHELL observations (see 45), exposure times ( $t_{exp}$ ) were limited to 5 minutes due to the uncertainties of barycenter corrections scaling as  $t_{exp}^2$  (104), and the dynamicity of telluric absorption over a single exposure. We initially recorded 22 exposures per-night, and later increased this to 42 as the cumulative  $S/N$  within a night was insufficient ( $\sim 100$ ).<sup>1</sup> Raw CHIRON observations are reduced via the `REDUCE` package (105), and the corresponding RVs are computed using `pychell`. Unfortunately, a significant fraction of the extracted 1-dimensional spectra are too noisy to robustly measure the precise

---

<sup>1</sup>Unlike iSHELL (and like many modern echelle spectrographs), CHIRON makes use of an exposure meter in order to calculate the proper (flux-weighted) exposure midpoint, and therefore longer exposure times will be less-impacted by the uncertainty in computing the exposure midpoint. Further, tellurics at visible wavelengths are far more sparse than for iSHELL at K-band wavelengths. We therefore recommend significantly longer exposure times ( $\geq 30$  minutes) for future observations of AU Mic (or targets of similar brightness) with CHIRON in narrow slit mode.

Table 3.1: A summary of the RV datasets used in this work. The nightly-binned measurements are provided in appendix C.  $N_{\text{tot}}$  and  $N_{\text{nights}}$  refers to the number of individual and per-night epochs, respectively. The median intrinsic error bars  $\sigma_{RV}$  consider all observations.

Spectrograph/ Facility	$\lambda/\Delta\lambda$ [ $\times 10^3$ ]	$N_{\text{nights}}$	$N_{\text{used}}$	Median $\sigma_{RV}$ [ $\text{m s}^{-1}$ ]	Adopted $\lambda$ [nm]	Pipeline	Comm. Paper
HIRES/Keck	85	60	41	2.6	565	–	(95)
Tillinghast/TRES	44	85	55	24.2	650	–	(97)
CARMENES-Vis/ Calar Alto 3.5m	94.6	63	60	11.4	750	caracal (88)	(87)
CARMENES-NIR/ Calar Alto 3.5m	80.4	62	49	32.6	1350	SERVAL (110)	–
SPIRou/CFHT	75	27	27	5.0	1650	K21	(111)
iSHELL/IRTF	85	46	31	5.0	2350	pychell (45)	(101)
HARPS-S/ La Silla 3.6m	115	34	0	2.2	565	ESO DRS (112)	(113)
MINERVA- Australis-T3	80	13	0	9.5	565	HARPS-TERRA (86)	(82)
MINERVA- Australis-T4	80	13	0	9.5	565	–	(83)
MINERVA- Australis-T6	80	13	0	9.5	565	–	(84)
CHIRON/CTIO	136	12	0	46	565	(114)	(115)
IRD/Subaru	70	6	0	3.0	1350	(45) IRAF; (93)	(91)
NIRSPEC/Keck	25	14	0	50	2350	(94)	(116)
CSHELL/IRTF	36	21	0	26	2350	(49) (117), (118)	(119)

RVs from (peak  $S/N \approx 20 - 30$  per spectral pixel). We therefore flag clear outliers in the RV measurements, and re-compute the nightly (binned) RVs resulting in 12 epochs to be included in our analyses.

### 3.2.2 Photometry from *TESS*

The NASA *TESS* mission (81) observed AU Mic in Sectors 1 (2018-July-25 to 2018-August-22) and 27 (2020-July-04 to 2020-July-30). We download the light-curves from the Mikulski Archive for Space Telescopes (106, MAST). We use the Science Processing Operations Center (SPOC; 1) “Presearch Data Conditioning” light curves utilizing “Simple Aperture Photometry” (PDCSAP; 107; 108; 109) to inform our model in section 3.3.3.

## 3.3 Radial Velocity Fitting

### 3.3.1 Bayesian Inference for Radial-Velocities

We primarily seek to utilize a global (joint) Gaussian process model with multiple realizations that give rise to the data we observe with all of the above instruments simultaneously. To implement our desired framework, we have developed two *Python* packages. We leave the description of `optimize` - a high-level Bayesian inference framework to appendix A.

To provide RV-specific routines, we extend the `optimize` package within the `orbits` submodule of the `pychell` (45) package<sup>2</sup>. We define classes specific for RV-data, models, and likelihoods, with much of the “boiler-plate” code handled through `optimize`. A top-level “RVProblem” further defines a pool of RV-specific methods for pre- and post-optimization routines, such as plotting phased RVs, periodogram tools, model comparison tests, and propagation of MCMC chains for deterministic Keplerian parameters (e.g, planet masses, semi-major axes, and densities).

### 3.3.2 Two Chromatic Gaussian Processes

A Gaussian process kernel is defined through a square matrix,  $\mathbf{K}$  (also called the covariance matrix), where each entry describes the covariance between two measurements<sup>3</sup>. We introduce two GP kernels as extensions of the quasi-periodic (QP) kernel, which has been demonstrated in numerous cases to model rotationally modulated stellar activity in both photometric and RV observations (see Section 3.1)<sup>4</sup>.

---

<sup>2</sup>Documentation: <https://pychell.readthedocs.io/en/latest/>

<sup>3</sup>See (120) for a thorough discussion of Gaussian processes.

<sup>4</sup>Other parameterizations are also common.



$$\mathbf{K}_{\mathbf{QP}}(t_i, t_j) = \eta_\sigma^2 \exp \left[ -\frac{\Delta t^2}{2\eta_\tau^2} - \frac{1}{2\eta_\ell^2} \sin^2 \left( \pi \frac{\Delta t}{\eta_p} \right) \right] \quad (3.1)$$

where  $\Delta t = |t_i - t_j|$

Here,  $\eta_P$  typically represents the stellar-rotation period,  $\eta_\tau$  the mean spot lifetime, and  $\eta_\ell$  is the relative contribution of the periodic term, which may be interpreted as a smoothing parameter (larger is smoother).  $\eta_\sigma$  is the amplitude of the auto-correlation of the activity signal.

We seek to use a fully-inclusive QP-like kernel that accounts for the wavelength-dependence of the stellar activity present in our multi-wavelength dataset. In this work, we only modify the amplitude parameter,  $\eta_\sigma$ ; we leave further chromatic modifications (namely convective blue-shift and limb-darkening, see Section 3.1), as subjects for future work. To first order, we expect the amplitude from activity to be linearly proportional to frequency (or inversely proportional to wavelength). This approximation is a direct result of the spot-contrast scaling with the photon frequency (or inversely with wavelength) from the ratio of two black-body functions with different effective temperatures (21).

We first re-parametrize the amplitude through a linear kernel as follows:

$$\mathbf{K}_{\mathbf{J1}}(t_i, t_j) = \eta_{\sigma, s(i)} \eta_{\sigma, s(j)} \times \exp[\dots] \quad (3.2)$$

Here,  $\eta_{\sigma, s(i)} \eta_{\sigma, s(j)}$  are the effective amplitudes for the spectrographs at times  $t_i$  and  $t_j$ , respectively, where  $s(i)$  represents an indexing set between the observations at time  $t_i$  and spectrograph  $s$ .<sup>5</sup> Each amplitude is a free parameter.

---

<sup>5</sup>Truly simultaneous measurements (i.e.,  $t_i = t_j$ ) would necessitate a more sophisticated indexing set.

We also consider a variation of this kernel which further enforces the expected inverse relationship between the amplitude with wavelength. We rewrite the kernel to become:

$$\mathbf{K}_{\mathbf{J2}}(t_i, t_j, \lambda_i, \lambda_j) = \eta_{\sigma,0}^2 \left( \frac{\lambda_0}{\sqrt{\lambda_i \lambda_j}} \right)^{2\eta_\lambda} \times \exp[\dots] \quad (3.3)$$

Here,  $\eta_{\sigma,0}$  is the effective amplitude at  $\lambda = \lambda_0$ , and  $\eta_\lambda$  is an additional power-law scaling parameter with wavelength to allow for a more flexible non-linear (with frequency) relation.  $\lambda_i$  and  $\lambda_j$  are the “effective” wavelengths for observations at times  $t_i$  and  $t_j$ , respectively. For both eqs. 3.2 and 3.3, the expression within square brackets is identical to that in eq. 3.1.

To make predictions from  $\mathbf{K}_{\mathbf{J2}}$  (eq. 3.3), we follow (121) (eqs. 2.23 and 2.24). We construct the matrix  $\mathbf{K}_{\mathbf{J2}}(t_{i,*}, t_j, \lambda_*, \lambda_j)$ , which denotes the  $n_* \times n$  matrix of the covariances evaluated at all pairs of test points and training points (the data). Wavelengths in the  $*$  dimension are identical, and therefore each realization corresponds to a unique wavelength. This formulation allows us to realize the GP with high accuracy for all wavelengths so long as at least one wavelength is sampled near  $t_{i,*}$ . Predictions with kernel  $\mathbf{K}_{\mathbf{J1}}$  (eq. 3.2) are found in a similar fashion, where each realization corresponds to a particular spectrograph.

### 3.3.3 Primary RV Analyses

We first bin out-of-transit RV observations from each night (per-spectrograph). While not negligible, we expect changes from rotationally modulated activity to be small within a night, so we choose to mitigate activity on shorter timescales our model is not intended to capture. The median RV for each spectrograph is also subtracted. We choose to ignore poorly-sampled regions with respect to our adopted mean spot lifetime  $\eta_\tau$  (100 days, see Section 3.3.3); each instance of a covariance matrix represents a *family* of functions, and therefore the GP regression may be too flexible (and thus poorly constrained) in regions of low-cadence observations. We also ignore regions with only low precision measurements

(median errors  $\gtrsim 10 \text{ m s}^{-1}$ ). This limits our analyses to all observations between September 2019 – December 2020, and the spectrographs HIRES, TRES, CARMENES-Vis and NIR, SPIRou, and iSHELL. We do not include six binned IRD or thirteen binned MINERVA-Australis observations in our primary analyses as we expect the offsets to be poorly constrained in the presence of stellar activity. Finally, we discard 3 CARMENES-Vis and 13 CARMENES-NIR measurements from our analyses primarily near the beginning of each season due to residuals  $> 100 \text{ m s}^{-1}$  that are inconsistent with our other datasets. We suspect that telluric contamination which is further exacerbated by the high airmass of the observations may have degraded the CARMENES observations. For completeness, we present fit results including all spectrographs in appendix D. A summary of measurements is provided in Table 3.1.

Our RV model first consists of two Keplerian components for the known transiting planets, a GP model for stellar activity, and per-instrument zero points. The zero points are each assigned to  $1 \text{ m s}^{-1}$  with a uniform prior of  $\pm 300 \text{ m s}^{-1}$ . We further adopt a normal prior of  $\mathcal{N}(0, 100)$  to make each offset well-behaved<sup>6</sup>.

Analyses of the *TESS* transits in M20 found  $P_b = 8.4629991 \pm 0.0000024$  days,  $TC_b = 2458330.39046 \pm 0.00016$ ,  $P_c = 18.858991 \pm 0.00001$  days, and  $TC_c = 2458342.2243 \pm 0.0003$ . For all of our analyses, we fix  $P$  and  $TC$  for planets b and c; the uncertainties in these measurements are insignificant even for our full baseline of  $\approx 17$  years. The semi-amplitudes of each planet start at  $K_b = 8.5 \text{ m s}^{-1}$  and  $K_c = 5 \text{ m s}^{-1}$ , and are only enforced to be positive. Preliminary analyses of a secondary eclipse observed in *Spitzer* observations support a moderately eccentric orbit for AU Mic b, with  $e_b = 0.189 \pm 0.04$  (Collins et al., in prep.), which is somewhat larger than the eccentricity determined from the duration of the primary transits observed with *TESS* ( $e_b = 0.12 \pm 0.04$ , Gilbert et al., submitted to *Astrophysical Journal*). We assume a circular orbit for AU Mic c, and further examine eccentric cases in section 3.5.1. The Keplerian component of our RV model in `pychell` is nearly identical to that used in `RadVel` (122). Kepler’s equation is written in *Python* and

---

<sup>6</sup>The prior distribution for a parameter with  $\geq 1$  prior are improper, i.e., they do not integrate to unity.

makes use of the `numba.@jit` decorator (123) for optimal performance. We exclusively use the orbit basis  $\{P, TC, e, \omega, K\}$ .

Our optimizer seeks to maximize the natural-logarithm of the a posteriori probability (MAP) under the assumption of normally distributed errors:

$$\ln \mathcal{L} = -\frac{1}{2} \left[ \vec{r}^T \mathbf{K}_o^{-1} \vec{r} + \ln |\mathbf{K}_o| + N \ln(2\pi) \right] + \sum_i \ln \mathcal{P}_i \quad (3.4)$$

Here,  $\vec{r}$  is the vector of residuals between the observations and model.  $\mathbf{K}_o$  is the covariance matrix sampled at the same observations,  $N$  is the number of data points, and  $\{\mathcal{P}_i\}$  is the set of prior knowledge. We maximize eq. 3.4 using the iterative Nelder-Mead algorithm described in (45), which is included as part of the `optimize` package. We also sample the posterior distributions using the `emcee` package (124) for a subset of models to determine parameter uncertainties, always starting from the MAP-derived parameters. In all cases, we use twice the number of chains as varied parameters. We perform a burn-in phase of 1000 steps followed by a full MCMC analysis for  $\approx 50 \times$  the median auto-correlation time (steps) of all chains.

### Estimation of Kernel Parameters

We briefly analyze both Sectors of *TESS* photometry in order to estimate the GP kernel parameters  $\eta_\tau$ ,  $\eta_\ell$ , and  $\eta_P$ . We note that the rotationally modulated structure in both Sectors is consistent (fig. 3.1). If we assume spots are spatially static in the rest-frame of the stellar-surface (i.e., spots do not migrate), this suggests a similar spot configuration and contrast for each Sector. We first determine  $\eta_P$  by qualitatively analyzing both *TESS* Sectors phased up to periods close to that used in M20 ( $4.862 \pm 0.032$  days) with a step size of 0.001 days (see fig. 3.1). We find  $\eta_P \approx 4.836$  or  $\eta_P \approx 4.869$  days from our range of periods tested; no periods between these two values are consistent with our assumption of an identical spot configuration. The difference in these two periods further corresponds to one additional period between the two sectors (i.e.,  $|1/\eta_{P,1} - 1/\eta_{P,2}| \approx 1/700 \text{ days}^{-1}$ ). The

smaller of these two values implies AU Mic b is in a 7:4 resonance with the stellar rotation period, potentially indicating tidal interactions between the planet and star. We adopt  $\eta_P \sim \mathcal{N}(4.836, 0.001)$  in all our analyses where the uncertainty is a conservative estimate determined by our step size.

Although the *TESS* light curve itself can provide insight into  $\eta_\tau$  and  $\eta_\ell$ , we instead try to estimate these values directly from the predicted spot-induced RV variability via the  $FF'$  technique (125):

$$\Delta RV_{\text{spots}}(t) = -F(t)F'(t)R_\star/f \quad (3.5)$$

Here,  $F$  is the photometric flux and  $f$  represents the relative flux drop for a spot at the center of the stellar disk. To compute  $F$  and  $F'$  (the derivative of  $F$  with respect to time), we first fit the *TESS* light curve via cubic spline regression (`scipy.interpolate.LSQUnivariateSpline`; 126) for each Sector individually with knots sampled in units of 0.5 days ( $\approx 10\%$  of one rotation period) to average over transits and the majority of flare events (fig. 3.1). The nominal cubic splines are then used to directly compute both  $F$  and  $F'$  on a down-sampled grid of 100 evenly-spaced points for each Sector. We then divide the resulting joint-Sector curve by its standard deviation for normalization; we do not care to directly fit for the chromatic parameter  $f(\text{TESS}, \dots)$ . We further assume  $f$  to be constant in time (i.e., spots are well-dispersed on the stellar surface). We then perform both MAP and MCMC analyses for this curve using a standard QP kernel (eq. 3.1) with loose uniform priors of  $\eta_\tau \sim \mathcal{U}(10, 2000)$  (days) and  $\eta_\ell \sim \mathcal{U}(0.05, 0.6)$ . We set the intrinsic error bars of the curve to zero but include an additional “jitter” (white noise) term in the model with a Jeffrey’s prior (127) distribution with the knee at zero to help keep the jitter well-behaved by discouraging larger values unless it significantly improves the fit-quality through an inversely proportional penalty term. The amplitude of the model is drawn from a wide uniform distribution of  $\mathcal{U}(0.3, 3.0)$ . The posterior distributions are provided in fig. 3.2.

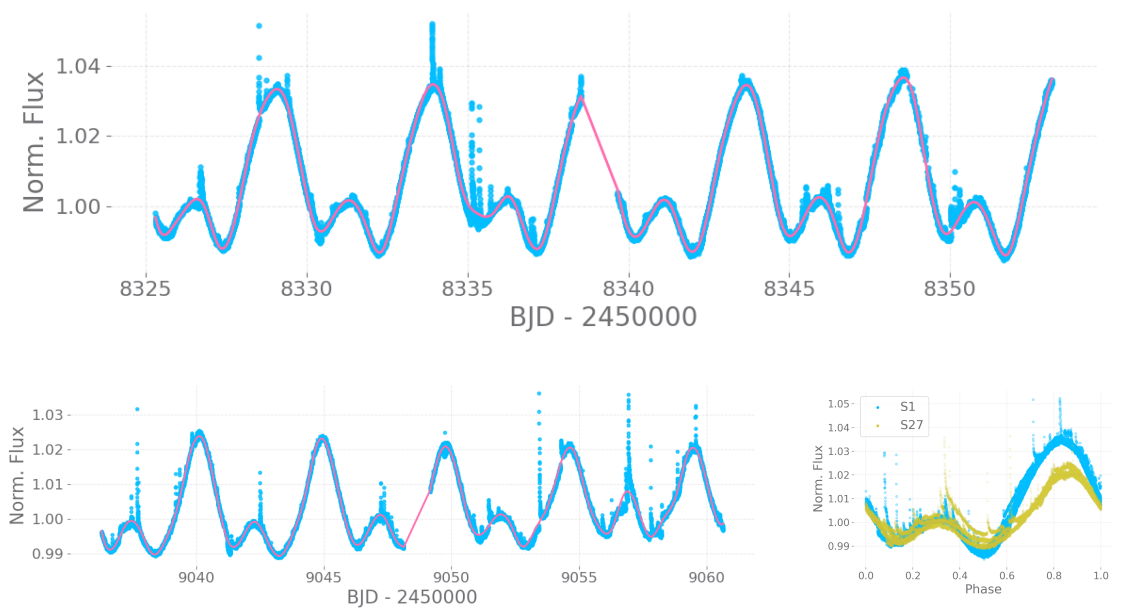


Figure 3.1: The *TESS* PDCSAP light curves of AU Mic from Sectors 1 (top) and 27 (bottom). The lower right plot shows both Sectors phased to 4.836 days. Although the two seasons exhibit nearly identical periodic signals, Sector 27 exhibits moderate evolution. The least-squares cubic spline fit for each Sector is shown in pink.

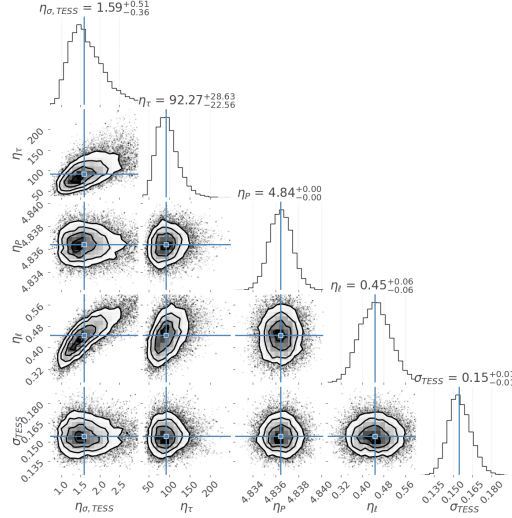


Figure 3.2: Posterior distributions from fits to the predicted RV variability from the  $FF'$  technique (eq. 3.5).

A fit to the  $FF'$  curve suggests the mean activity timescale  $\eta_\tau \approx 92^{+29}_{-23}$  days. Although our interpretation implies  $\eta_\tau$  should be comparable to the gap between the two Sectors, ( $\sim 700$  days) we do not have photometric measurements between the two Sectors, and therefore cannot speak to evolution which will be important for our 2019 observations. We further note that the *TESS* Sector 27 light curve exhibits moderate evolution whereas Sector 1 appears more stable (fig. 3.1). The posterior distributions are also consistent with a relatively smooth GP with the period length scale  $\eta_\ell \approx 0.45 \pm 0.06$ .

Before making use of our joint kernels, we first assess the performance of the standard QP kernel (eq. 3.1) for each instrument individually. Here, each spectrograph makes use of a unique QP kernel and amplitude term, but the remaining three GP parameters are shared across all kernels. Each amplitude is drawn from a Gaussian prior with mean equal to the standard deviation of the dataset, and a conservative width of  $30 \text{ ms}^{-1}$ . The expected semi-amplitudes for AU Mic b and c ( $\lesssim 10 \text{ ms}^{-1}$ ) will negligibly affect this estimation. We also apply a Jeffrey's prior with the knee at zero to help keep the amplitude well-behaved. For  $\eta_\tau$  and  $\eta_\ell$ , we first make use of the same priors used to model the  $FF'$  curve. We

further include a fixed jitter term at  $3 \text{ ms}^{-1}$  added in quadrature along the diagonal of the covariance matrix  $\mathbf{K}_\mathbf{o}$  for the HIRES observations only; HIRES observations provide the smallest intrinsic uncertainties, but are most impacted by activity (largest in amplitude), so we choose to moderately down-weight the HIRES observations. Given the flexibility of GP regression with a nightly-cadence, we choose not to fit for (nor include) jitter-terms for other spectrographs, and further discuss this decision in Section 3.5.5. This is the most flexible model we employ to the RVs, and we therefore use these results to flag the aforementioned CARMENES-Vis and CARMENES-NIR measurements.

We find normally distributed posteriors for  $\eta_\tau$  and  $\eta_\ell$  (fig. B.1), but the reduced  $\chi^2$  statistic of 0.22 indicates the model significantly over fits the data. The per-spectrograph amplitudes are reasonably consistent with their respective priors, so we assert this is a result of  $\eta_\tau$  ( $\approx 43$  days) and/or  $\eta_\ell$  ( $\approx 0.23$ ) taking on too small of values, indicating our RV model is insufficient to constrain these values from the RV observations, either due to insufficient cadence and/or an inadequate model. We therefore again fix  $\eta_\tau = 100$  days to let each season have mostly distinct activity models, while minimizing the flexibility within each season, which is consistent with what the  $FF'$  curve suggests. As a compromise between the  $FF'$  and RV analyses, we also fix  $\eta_\ell = 0.28$ . Our adopted value of  $\eta_\tau$  is larger than that used in K21 ( $\approx 70$  days<sup>7</sup>), while  $\eta_\ell$  is nearly identical. We further explore these decisions and its impact on our derived semi-amplitudes in section 3.5.2. With fixed value for  $\eta_\tau$ , we re-run MAP and MCMC fits with disjoint kernels, yielding a reduced  $\chi^2$  of 0.57, indicating the model is still over-fit, but less so.

### Joint Kernel RV Fitting

We use results from the disjoint case to inform our primary joint-kernel models. Although the different GPs appear similar (fig. 3.3), each still exhibits unique features, suggesting a simple scaling is not valid, and/or insufficient sampling for each kernel individually. Regardless, our two joint kernels will enforce a perfect scaling between any two spectrographs.

---

<sup>7</sup>In K21, the hyperparameters  $\eta_\tau$  and  $\eta_\ell$  absorb the factors of two present in the formulation used in this work (eq. 3.1).



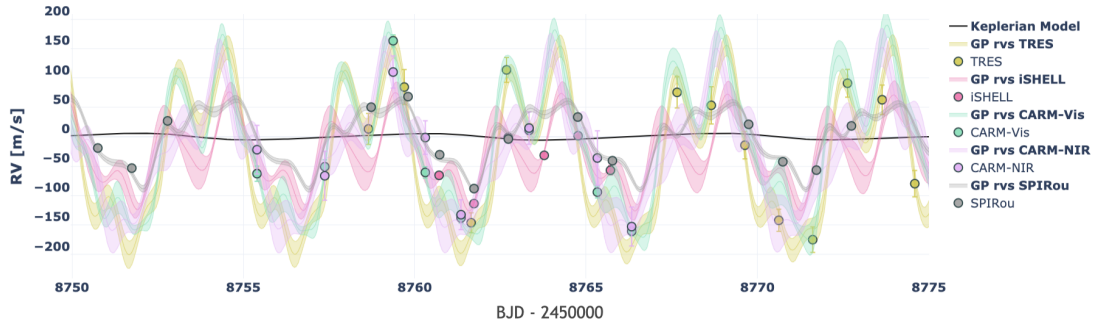


Figure 3.3: RVs of AU Mic zoomed in on a window with high-cadence, multi-wavelength observations from 2019. Here, we use a disjoint QP GP kernel (eq. 3.1) to model the stellar activity. Each plotted dataset is only corrected according to the best-fit zero points. Data errors are computed by adding the intrinsic errors in quadrature with the GP uncertainty. Although each GP makes use of the same parameters, each still exhibits unique features. This indicates either an insufficient activity model with our cadence or yet-to-be characterized chromatic effects of activity from different wavelength regimes not consistent with a simple scaling relation.

We run MAP and MCMC fits using the joint kernel  $\mathbf{K}_{J1}$  (eq. 3.2) again making use of the same normal and Jeffrey’s priors for each amplitude. We then fit the resulting set of best-fit amplitudes using our proposed power law relation (see eq. 3.3):  $\eta_{\sigma}(\lambda) = \eta_{\sigma,0}(\lambda_0/\lambda)^{\eta_{\lambda}}$  with `scipy.optimize.curve_fit` (128) (fig. 3.6). We arbitrarily anchor  $\lambda_0$  at  $\lambda = 565$  nm. The effective mean wavelength of each spectrograph should consider the RV information content (stellar and calibration), and ignore regions with dense telluric features. For gas-cell calibrated spectrographs (HIRES, CHIRON, and iSHELL), we do limit the the range to regions with gas cell features. For all other spectrographs, we take the effective RV information content to be uniform over the full spectral range. We further do not consider regions of tellurics which may have been masked (e.g., CARMENES RVs generated with **SERVAL**). Although these estimation are crude, they are only relevant to kernel  $\mathbf{K}_{J2}$  (eq. 3.3). The adopted wavelengths for each spectrograph are listed in Table 3.1.

We find  $\eta_{\sigma,0} \approx 221 \text{ m s}^{-1}$ , and  $\eta_{\lambda} \approx 1.17$ . This amplitude is significantly larger than the intrinsic scatter of our observations (namely HIRES) suggests, so we adopt a tight normal prior of  $\mathcal{N}(221, 10)$  to restrict it from getting any larger. We only apply a loose uniform

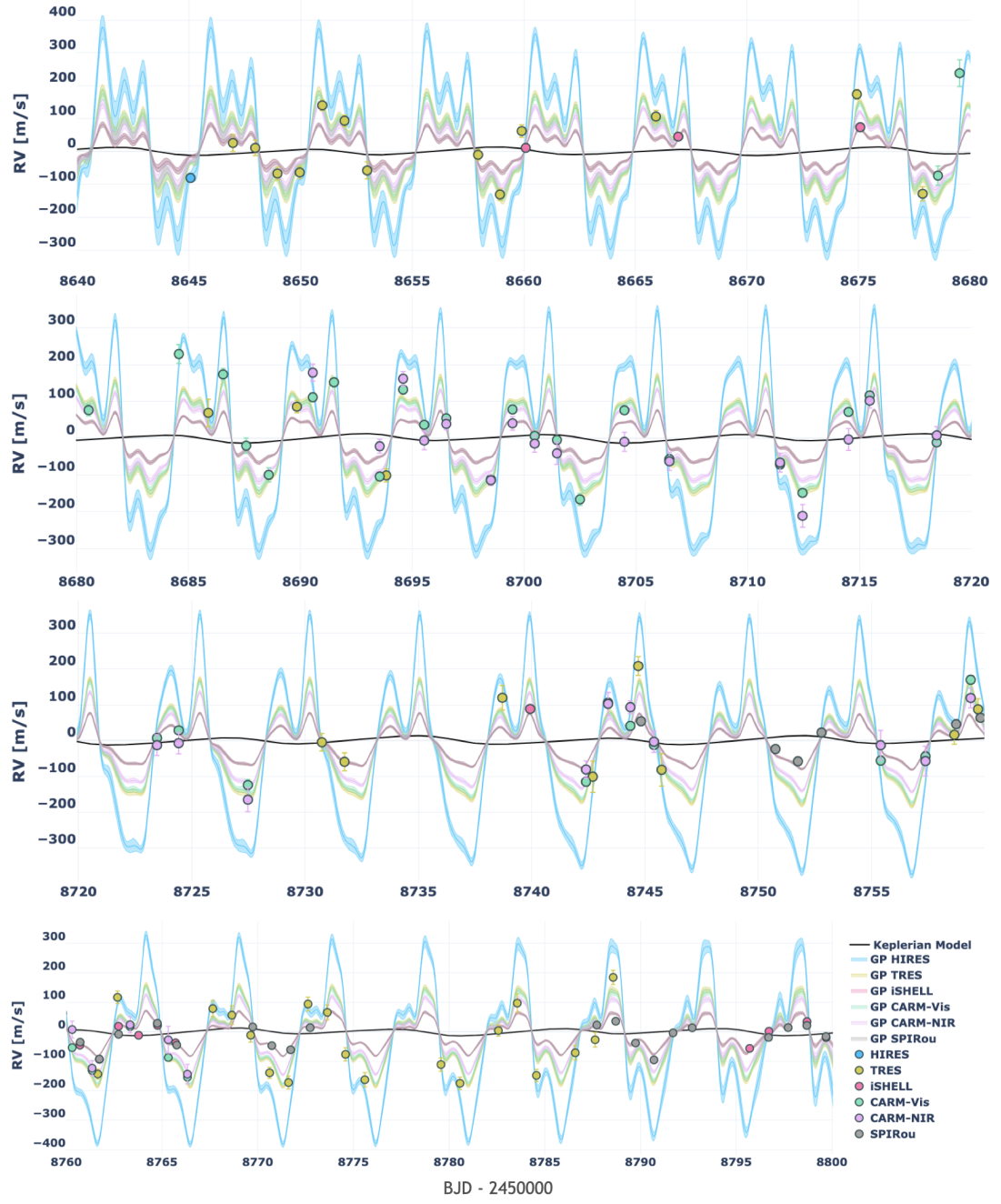


Figure 3.4: Here we show the 2019 RVs using kernel  $\mathbf{K}_{J1}$  (eq. 3.2) to model the stellar activity. Although there is only one HIRES observation in early 2019, we are still able to make predictions for the HIRES GP for the entire baseline by using joint kernels.

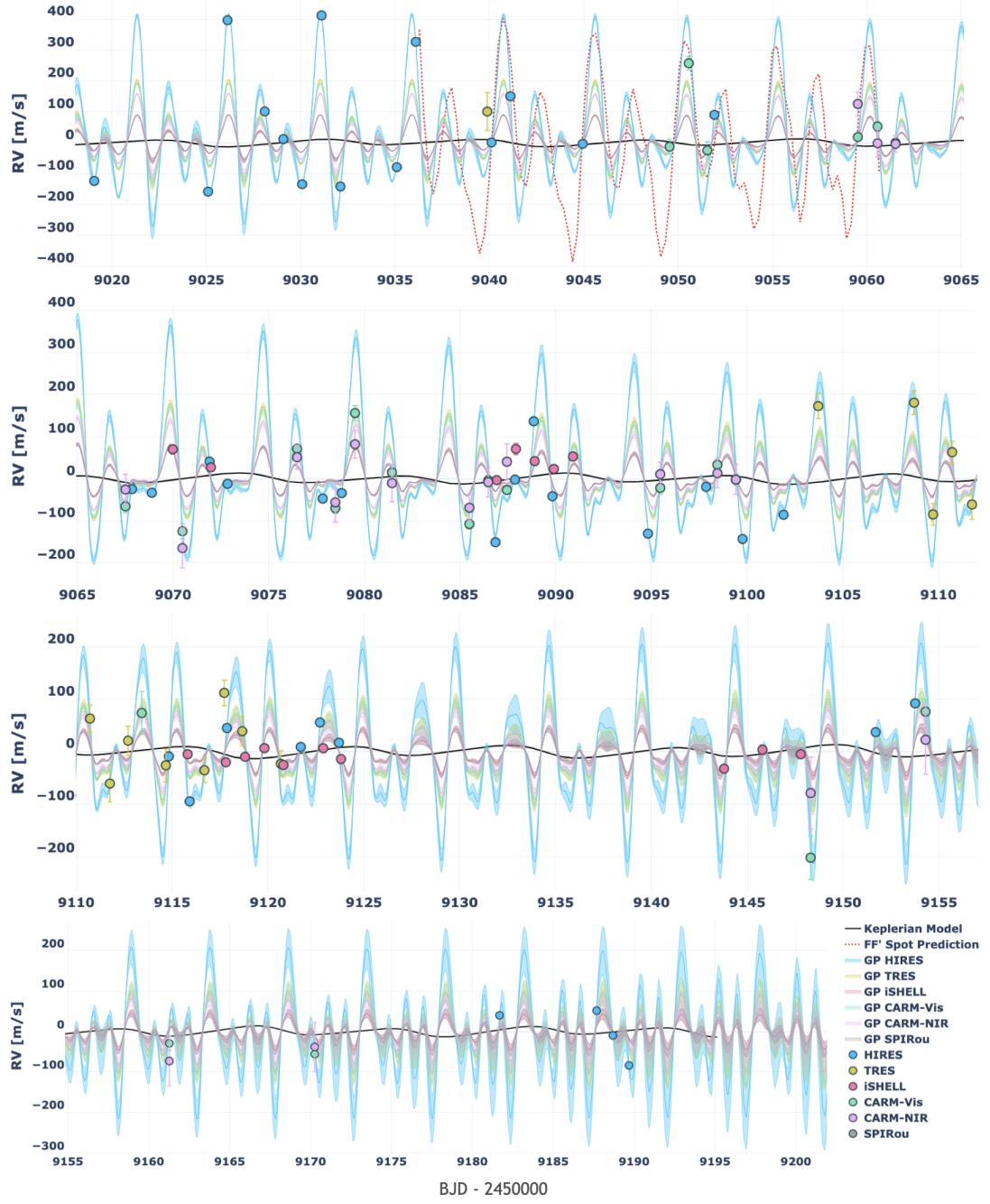


Figure 3.5: Same as fig. 3.4, but for our 2020 observations which overlap with the *TESS* Sector 27 photometry. In red we show the generated  $FF'$  curve for spot-induced activity signals (eq. 3.5, arbitrarily scaled) generated from the *TESS* light-curve (section 3.3.3).

Table 3.2: The model parameters and prior distributions used in our primary fitting routines.  $\blacksquare$  indicates the parameter is fixed. Parameters with multiple priors are We run models utilizing  $\mathbf{K}_{J1}$  and  $\mathbf{K}_{J2}$ . We list the radii of AU Mic b and c measured in M20 which we use to compute the corresponding densities of each planet.

Parameter [units]	Initial Value ( $P_0$ )	Priors	Citation
$P_b$ [days]	8.4629991	$\blacksquare$	Primary transit; M20
$TC_b$ [days]	2458330.39046	$\blacksquare$	Primary transit; M20
$e_b$	0.189	$\mathcal{N}(P_0, 0.04)$	Secondary eclipse; Collins et al. in prep
$\omega_b$ [rad]	1.5449655	$\mathcal{N}(P_0, 0.004)$	Secondary eclipse; Collins et al. in prep
$K_b$ [ms $^{-1}$ ]	8.5	Positive	K21
$P_c$ [days]	18.858991	$\blacksquare$	Primary transit; M20
$TC_c$ [days]	2458342.2243	$\blacksquare$	Primary transit; M20
$e_c$	0	$\blacksquare$	—
$\omega_c$ [rad]	$\pi$	$\blacksquare$	—
$K_c$ [ms $^{-1}$ ]	5	Positive	M20
$\eta_{\sigma,0}$ [m s $^{-1}$ ]	216	$\mathcal{J}(1, 600), \mathcal{N}(P_0, 10)$	RVs; this work
$\eta_\lambda$	1.18	$\mathcal{U}(0.3, 2)$	RVs; this work
$\eta_{\sigma,HIRES}$ [m s $^{-1}$ ]	130	$\mathcal{J}(1, 600), \mathcal{N}(P_0, 30)$	RVs; this work
$\eta_{\sigma,TRES}$ [m s $^{-1}$ ]	103	$\mathcal{J}(1, 600), \mathcal{N}(P_0, 30)$	RVs; this work
$\eta_{\sigma,CARM-VIS}$ [m s $^{-1}$ ]	98	$\mathcal{J}(1, 600), \mathcal{N}(P_0, 30)$	RVs; this work
$\eta_{\sigma,CARM-NIR}$ [m s $^{-1}$ ]	80	$\mathcal{J}(1, 600), \mathcal{N}(P_0, 30)$	RVs; this work
$\eta_{\sigma,SPIROU}$ [m s $^{-1}$ ]	42	$\mathcal{J}(1, 600), \mathcal{N}(P_0, 30)$	RVs; this work
$\eta_{\sigma,iSHELL}$ [m s $^{-1}$ ]	40	$\mathcal{J}(1, 600), \mathcal{N}(P_0, 30)$	RVs; this work
$\eta_\tau$ [days]	100	$\blacksquare$	TESS light curve and RVs; this work
$\eta_\ell$	0.28	—	TESS light curve and RVs; this work
$\eta_p$ [days]	4.836	$\mathcal{N}(P_0, 0.001)$	TESS light curve; this work
$\gamma$ (per-spectrograph) [m s $^{-1}$ ]	1	$\mathcal{U}(-300, 300), \mathcal{N}(0, 100)$	RVs; this work
$\sigma_{HIRES}$ [m s $^{-1}$ ]	3	$\blacksquare$	—
$\sigma_{TRES}$ [m s $^{-1}$ ]	0	$\blacksquare$	—
$\sigma_{CARM-VIS}$ [m s $^{-1}$ ]	0	$\blacksquare$	—
$\sigma_{CARM-NIR}$ [m s $^{-1}$ ]	0	$\blacksquare$	—
$\sigma_{SPIROU}$ [m s $^{-1}$ ]	3 0	$\blacksquare$	—
$\sigma_{iSHELL}$ [m s $^{-1}$ ]	3 0	$\blacksquare$	—
$M_\star$ [ $M_\odot$ ]	$0.5^{+0.03}_{-0.03}$	—	P20
$R_b$ [ $R_\oplus$ ]	$4.38^{+0.18}_{-0.18}$	—	P20
$R_c$ [ $R_\oplus$ ]	$3.51^{+0.16}_{-0.16}$	—	M20

prior for  $\eta_\lambda \sim \mathcal{U}(0.2, 2)$ . We then run corresponding MAP and MCMC fits with kernel  $\mathbf{K}_{J2}$  (eq. 3.3). A summary of all parameters is provided in Table 3.2. We present and discuss fit results from both joint kernels in Section 3.4.

### 3.4 Results

The best-fit parameters and corresponding uncertainties from the MAP and MCMC analyses with a two-planet model using joint kernels  $\mathbf{K}_{J1}$  (eq. 3.2) and  $\mathbf{K}_{J2}$  (eq. 3.3) are provided in Table 3.3. We compute planet masses, densities, and orbital semi-major axes by propagating the appropriate MCMC chains. The uncertainties in  $M_\star$  and the planetary radii from Table 3.2 are added in quadrature where appropriate. A corner plot presenting the posterior distributions of each varied parameter are provided in figs. B.3 and B.4 for

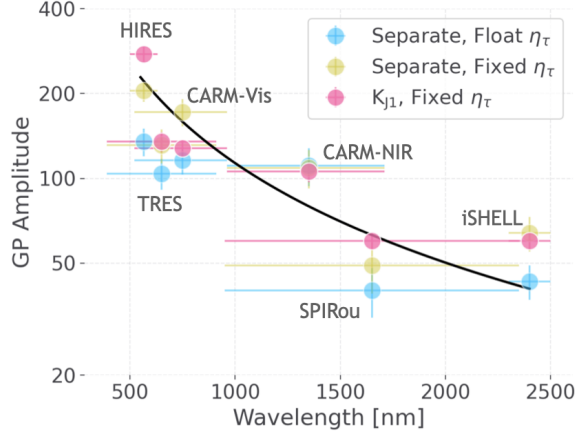


Figure 3.6: The best-fit GP amplitudes and uncertainties from kernels without enforcing any dependence with wavelength. We consider cases which let  $\eta_\tau$  and  $\eta_\ell$  float as well as and our fixed values (see Table 3.2). The solid line is a least-squares solution to the amplitudes for kernel  $\mathbf{K}_{J2}$  (eq. 3.3) for the joint-kernel fixed case (pink markers). Horizontal bars correspond to the adopted spectral range for each instrument.

kernels  $\mathbf{K}_{J1}$  and  $\mathbf{K}_{J2}$ , respectively. All chains are well-converged, with posteriors resembling Gaussian distributions. We find the offsets for each spectrograph are highly correlated with one-another; we note this is unique to the cases leveraging a joint-kernel, and strongest when datasets overlap, but do not further explore this result.

With kernel  $\mathbf{K}_{J1}$  (eq. 3.2), we report the median semi-amplitudes of AU Mic b and c to be  $10.23^{+0.88}_{-0.91} \text{ m s}^{-1}$  and  $3.68^{+0.87}_{-0.86} \text{ m s}^{-1}$ , corresponding to masses of  $20.12^{+1.57}_{-1.72} M_\oplus$  and  $9.60^{+2.07}_{-2.31} M_\oplus$ , respectively. The phased-up RVs for AU Mic b and c are shown in fig. 3.7. With kernel  $\mathbf{K}_{J2}$  (eq. 3.3), we find  $K_b = 8.92^{+0.85}_{-0.85} \text{ m s}^{-1}$  and  $K_c = 5.21^{+0.90}_{-0.87} \text{ m s}^{-1}$ . Both our findings for  $K_b$  are larger but within  $1\sigma$  of the semi-amplitude reported in K21 ( $8.5^{+2.3}_{-2.2} \text{ m s}^{-1}$ ). The mass of AU Mic c is also consistent with a Chen-Kipping mass-radius relation ( $\approx 12.1 M_\oplus$ ; 5). The posterior distributions for  $e_b$  and  $\omega_b$  are also consistent with their respective priors. Our finding for  $K_b$  is nearly twice as large as that obtained when using disjoint QP kernels ( $5.58 \text{ m s}^{-1}$ , fig. B.2), although the uncertainties are similar. With disjoint kernels, we find no evidence in the RVs for AU Mic c.

We further validate our results by computing the Bayesian information criterion (BIC) and the small-sample Akaike information criterion (129; 130). We compute the relevant quantities for a power-set of planet models. We are not trying to independently detect the eccentricity of AU Mic b and therefore do not include cases with  $e_b = 0$ . Prior probabilities are not included in the calculation of the corresponding  $\ln \mathcal{L}$  (eq. 3.4) to maintain normalization between different models. The results are summarized in Table 3.5 and are consistent with the relative precisions for each derived semi-amplitude.

Lastly, we compute and present the reduced chi-squared statistic ( $\chi_{red}^2$ ) for each spectrograph individually to assess their respective goodness of fit (Table 3.4). We find the HIRES observations are significantly over-fit ( $\chi_{red}^2=0.64$ ), whereas the other spectrographs are under-fit. We suspect this is due to the activity amplitude for HIRES being significantly larger than the other spectrographs despite exhibiting a similar overall dispersion. Although we include an additional  $3 \text{ ms}^{-1}$  white noise term for the HIRES observations, they still yield the smallest overall error bars and therefore are given the most weight in the GP regression. Although a more flexible uncorrelated noise model (i.e., a varied “jitter” parameter for each spectrograph), we favor the model without them for the variety of reasons discussed in Section 3.5.5.

### 3.4.1 Evidence For Additional Candidates?

We compute periodograms to further assess the relative statistical confidence of the two transiting planets and to search for other planets in the system. We first compute a series of generalized Lomb-Scargle (GLS; 103; 131) periodograms out to 500 days after removing the nominal zero-points, appropriate GPs, and the two planets, all generated using parameters from our nominal two-planet model (Table 3.3) with kernel  $\mathbf{K}_{J1}$  (eq. 3.2) to model the stellar activity. We also compute an activity-filtered periodogram from a planet-free model to assess how much the GP model will absorb planetary signals, and inform our interpretation of other peaks present in the periodogram. We further plot the normalized power-levels for false alarm probabilities (FAPs) of 10%, 1%, and 0.1%.

Table 3.3: The best-fit parameters and corresponding Keplerian variables for our primary two-planet fits using joint-kernels  $\mathbf{K}_{J1}$  (eq. 3.2) and  $\mathbf{K}_{J2}$  (eq. 3.3). The MCMC values correspond to the 15.9<sup>th</sup>, 50<sup>th</sup>, and 84.1<sup>th</sup> percentiles. Planet masses, densities, and semi-major axes are computed by propagating the appropriate MCMC chains. We also add in quadrature the uncertainties in  $M_\star$  and planetary radii from Table 3.2 where relevant.

Name [units]	MAP (J1)	MCMC (J1)	MAP (J2)	MCMC (J2)
$P_b$ [days]	8.4629991	—	—	—
$TC_b$ [days; BJD]	2458330.39046	—	—	—
$e_b$	0.187	$0.186^{+0.036}_{-0.035}$	0.182	$0.181^{+0.035}_{-0.035}$
$\omega_b$ [radians]	1.5452	$1.5451^{+0.0038}_{-0.0038}$	1.5453	$1.5454^{+0.0041}_{-0.0041}$
$K_b$ [m s <sup>-1</sup> ]	10.21	$10.23^{+0.88}_{-0.91}$	8.94	$8.92^{+0.85}_{-0.85}$
$M_b$ [ $M_\oplus$ ]	20.14	$20.12^{+1.57}_{-1.72}$	17.66	$17.73^{+1.68}_{-1.62}$
$a_b$ [AU]	0.0645	$0.0645^{+0.0013}_{-0.0013}$	—	—
$\rho_b$ [g/cm <sup>3</sup> ]	1.32	$1.32^{+0.19}_{-0.20}$	1.16	$1.16^{+0.18}_{-0.18}$
$P_c$ [days]	18.858991	—	—	—
$TC_c$ [days; BJD]	2458342.2243	—	—	—
$e_c$	0	—	—	—
$\omega_c$ [radians]	$\pi$	—	—	—
$K_c$ [m s <sup>-1</sup> ]	3.62	$3.68^{+0.87}_{-0.86}$	5.23	$5.21^{+0.90}_{-0.87}$
$M_c$ [ $M_\oplus$ ]	9.50	$9.60^{+2.07}_{-2.31}$	13.71	$14.12^{+2.48}_{-2.71}$
$a_c$ [AU]	0.1101	$0.1101^{+0.002}_{-0.002}$	—	—
$\rho_c$ [g/cm <sup>3</sup> ]	1.21	$1.22^{+0.26}_{-0.29}$	1.75	$1.80^{+0.31}_{-0.34}$
$\gamma_{HIRES}$ [m s <sup>-1</sup> ]	2.9	$4.1^{+55.6}_{-57.0}$	-19.4	$-8.7^{+43.3}_{-42.9}$
$\gamma_{TRES}$ [m s <sup>-1</sup> ]	11.4	$12.1^{+27.4}_{-27.8}$	-0.2	$9.3^{+38.4}_{-38.0}$
$\gamma_{CARM-Vis}$ [m s <sup>-1</sup> ]	3.7	$4.3^{+26.0}_{-26.6}$	-12.1	$-3.4^{+34.5}_{-33.9}$
$\gamma_{CARM-NIR}$ [m s <sup>-1</sup> ]	2.6	$2.9^{+21.7}_{-21.8}$	-6.8	$-1.5^{+21.2}_{-21.2}$
$\gamma_{SPIRou}$ [m s <sup>-1</sup> ]	5.5	$5.6^{+12.3}_{-12.4}$	0.72	$5.1^{+17.8}_{-17.3}$
$\gamma_{iSHELL}$ [m s <sup>-1</sup> ]	-2.8	$-2.4^{+12.1}_{-12.4}$	-7.5	$-4.3^{+13.0}_{-12.9}$
$\eta_{\sigma,0}$ [m s <sup>-1</sup> ]	—	—	242.4	$243.1^{+8.8}_{-9.1}$
$\eta_\lambda$	—	—	0.843	$0.845^{+0.024}_{-0.024}$
$\eta_{\sigma,HIRES}$ [m s <sup>-1</sup> ]	269.4	$275.7^{+17.4}_{-16.4}$	—	—
$\eta_{\sigma,TRES}$ [m s <sup>-1</sup> ]	132.3	$135.4^{+10.6}_{-9.5}$	—	—
$\eta_{\sigma,CARM-Vis}$ [m s <sup>-1</sup> ]	125.1	$128.2^{+8.8}_{-8.2}$	—	—
$\eta_{\sigma,CARM-NIR}$ [m s <sup>-1</sup> ]	103.0	$105.5^{+9.1}_{-8.7}$	—	—
$\eta_{\sigma,SPIRou}$ [m s <sup>-1</sup> ]	58.5	$60.1^{+4.3}_{-4.0}$	—	—
$\eta_{\sigma,iSHELL}$ [m s <sup>-1</sup> ]	58.5	$60.0^{+4.2}_{-3.9}$	—	—
$\eta_P$ [days]	4.8384	$4.8384^{+0.0008}_{-0.0009}$	4.8376	$4.8376^{+0.0009}_{-0.0009}$

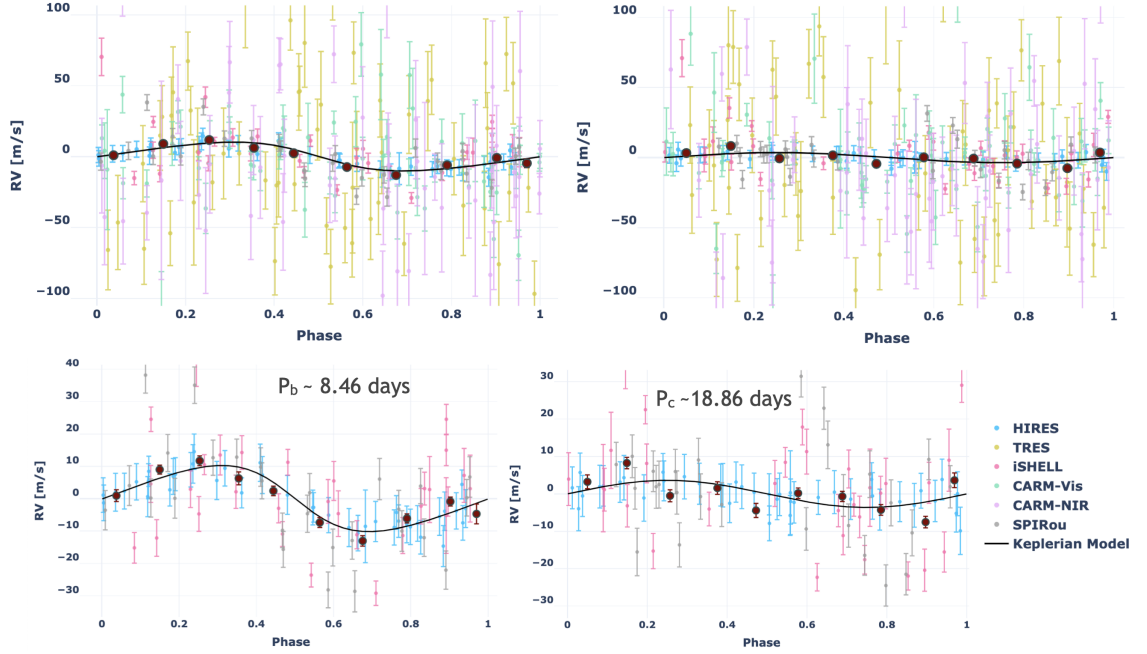


Figure 3.7: The phased RVs for AU Mic b (left column), and c (right column), and the corresponding best fit Keplerian models, generated from our nominal two-planet model. For each spectrograph, we subtract the unique zero-points, all other planet signals, and the appropriate GP. Corresponding data errors are computed by adding the intrinsic error and GP uncertainty in quadrature. The dark red points are generated by binning the phased RVs using a window size of 0.1, weighted by  $1/\sigma_{RV}^2$  where  $\sigma_{RV}$  are the data errors. In the top row we plot all data used in the fit. In the bottom row, we only show HIRES, iSHELL, and SPIRou. Although the HIRES cadence in 2020 was relatively dense with respect to the activity timescales  $\eta_\tau$  and  $\eta_P$ , the data still appears to be over-fit.

Table 3.4: Here we report the reduced chi-squared for each spectrograph from our nominal two-planet model using kernel  $\mathbf{K}_{J1}$ . Unlike when using quasi-disjoint kernels (Section 3.3.3), we find the model is overall significantly under-fit with the disjoint kernel. We suspect this is primarily due to an inadequate stellar-activity (i.e., a scaling relation is insufficient between spectrographs) and/or the exclusion of per-spectrograph jitter terms, and discuss these details further in Section 3.5.5.

Spectrograph	$\chi_{red}^2$
HIRES	0.64
TRES	5.97
CARMENES-Vis	4.96
CARMENES-NIR	4.25
SPIRou	12.84
iSHELL	18.62



We also compute “brute-force” periodograms by performing MAP fits for a wide range of fixed orbital periods for a user-defined “test-planet” with various assumptions for other model parameters (see 84). Given the time complexity of GP regression, we only consider periods out to 100 days. We first run two searches with no other planets in the model, first allowing for the test-planet’s  $TC$  to float, and second fixing  $TC$  to the nominal value for AU Mic b (Table 3.3). We then run searches for a second-planet, this time including a planetary model to account for the orbit of AU Mic b, with  $K_b \sim \mathcal{N}(8.5, 2.5)$ , consistent with the semi-amplitude found in K21. We again consider the case of letting the test-planet’s  $TC$  float, then run three cases with fixing the test-planet’s  $TC$  to each time of transit for AU Mic c from the *TESS* Sector 1 and 27 light curves (M20). Lastly, we perform a search for a third planet letting its  $TC$  float, and including models for AU Mic b and c ( $K_b \sim \mathcal{N}(8.5, 2.5)$ ,  $K_c > 0$ ).

Both the GLS (fig. 3.8) and brute-force (fig. 3.9) periodograms exhibit clear aliasing with a frequency of  $\approx 0.00281 \text{ days}^{-1}$  (or 356 days) which we attribute to having two seasons of observations separated by  $\approx 200$  days. Given the respective power of AU Mic b in both the GLS and brute-force planet-free periodograms, we briefly explore other peaks with similar power, even though all other peaks are below all three FAPs after removing the nominal two-planet model (fig. 3.8, row 3; fig. 3.9, row 7). Both two- and zero-planet periodograms (as well as GLS and brute-force) show power between AU Mic b and c’s orbits near 12.72 and 13.19 days, as well as power near 66.7 days for the residual RVs. Although these peaks are comparable in power to AU Mic b in both planet-free periodograms, they may be spurious. We further discuss the confirmation of AU Mic b and c as well as the validation of such additional potential candidates in Section 3.5.3. A mass-radius diagram is shown in fig. 3.10 to place the mass and radius of all AU Mic b and c in context with other known exoplanets, including a subset of young sample of exoplanets shown in P20. The plotted masses for AU Mic b and c are from our nominal two-planet model using kernel  $\mathbf{K}_{J1}$  (eq. 3.2).



Figure 3.8: GLS periodograms for AU Mic. Rows 1–4 are generated from our nominal two-planet MAP fit result using  $\mathbf{K}_{J1}$  (eq. 3.2) to model the stellar activity. From top to bottom, with each step applying an additional “correction”: 1. zero-point corrected RVs, 2. activity-filtered RVs, 3. planet b-filtered RVs, 4. planet c-filtered RVs. Annotated from left to right in green are the periods for AU Mic c and b. In the top row, we also annotate in orange (from left to right) potential aliases of the stellar rotation period  $3\eta_P$ ,  $2\eta_P$ , and  $3\eta_P/2$ , followed by the first three harmonics. In the bottom row, we compute a periodogram from an activity-filtered and trend-corrected zero-planet model to indicate how power from planets is absorbed by the GP. In each periodogram, we also identify the false alarm probability (FAP) power levels corresponding to 0.1% (highest), 1%, and 10% (lowest). The clear alias present in all periodograms is caused from the large gap between the two seasons of observations. In the bottom panel, we also plot in pink a Lomb-Scargle periodogram (arbitrarily scaled) of our window function (i.e, identical yet arbitrary RVs at each observation).

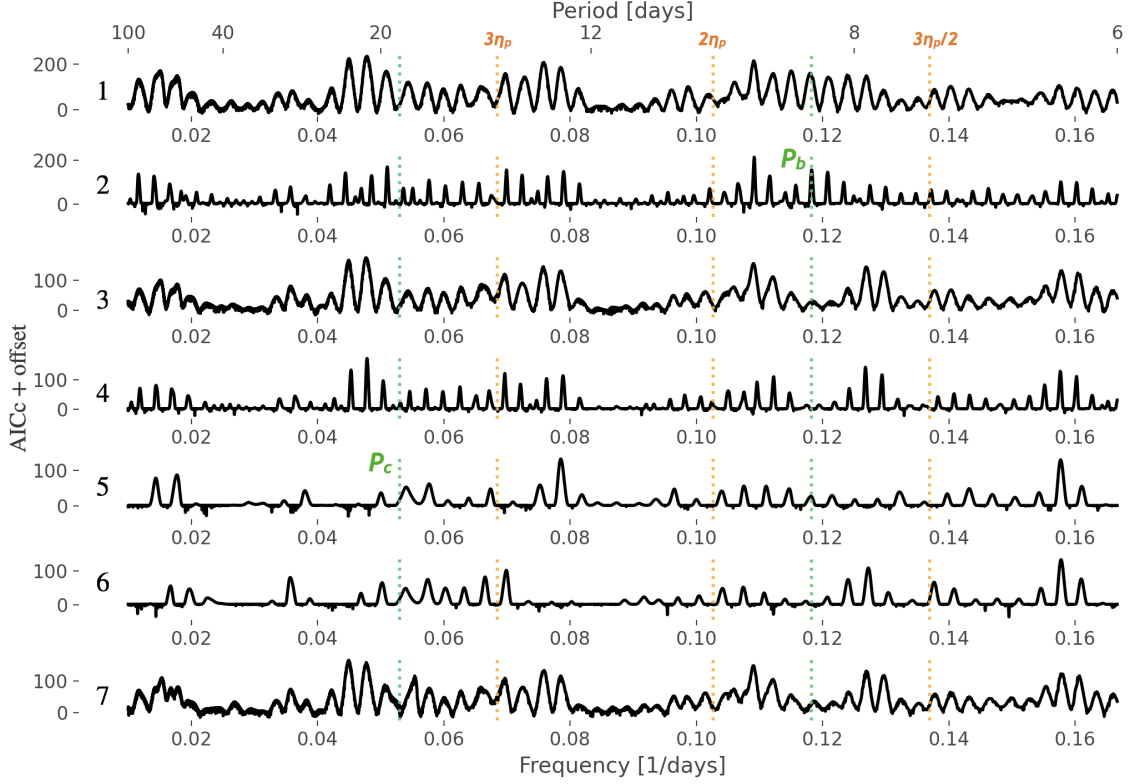


Figure 3.9: “Brute-force” periodograms for AU Mic with different assumptions for planetary models, but all making use of kernel  $\mathbf{K}_{J1}$  (eq. 3.2) to model the stellar activity. In each row, we perform a MAP fit for a wide range of fixed periods for a particular “test”-planet. In row 1, we include no other planets in our model, and allow for the test-planet’s  $TC$  to float. In row 2, we perform the same search but fixing  $TC$  to the nominal value for AU Mic b (Table 3.2). In row 3, we include a model for AU Mic b (with  $K_b \sim \mathcal{N}(8.5, 2.5)$ , see K21), and search for a second planet again letting  $TC$  float. In rows 4–6, we perform the same search but fix the test-planet’s  $TC$  to one of the three times of transit for AU Mic c from *TESS* (in chronological order). In the bottom row, we include nominal models for AU Mic b and c ( $K_b \sim \mathcal{N}(8.5, 2.5)$ ,  $K_c > 0$ ). We also annotate the same potential aliases with the stellar-rotation period (orange) and planetary periods (green) as in fig. 3.8.

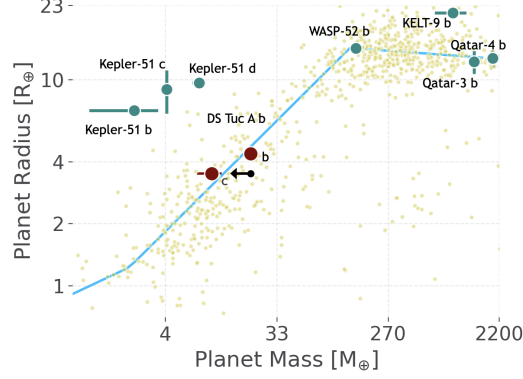


Figure 3.10: Here we plot the mass vs. radius for all exoplanets with provided radii and masses from the NASA Exoplanet Archive (4). For AU Mic b and c, we plot (maroon markers) the masses determined from our two-planet model with kernel  $\mathbf{K}_{\mathbf{J1}}$ . We also indicate with an arrow the  $5\sigma$  upper limit to the mass of AU Mic c determined from the posterior of  $K_c$ . The radii for b and c are those reported in M20. In blue, we plot a piecewise Chen-Kipping mass-radius relation (5). We also annotate (cyan markers) the masses and radii for a sample of young planets (stellar-age estimated  $\lesssim 400$  Myr).

Table 3.5: Model information criterion for AU Mic b and c using kernel  $\mathbf{K}_{\mathbf{J1}}$  (eq. 3.2) to model the stellar activity.

Planets	$\ln \mathcal{L}$	$\chi^2_{red}$	N free	$\Delta\text{AICc}$	$\Delta\text{BIC}$
b, c	-1760.3	3.99	17	181.7	162.3
b	-1769.0	4.04	16	197.0	174.3
c	-1824.1	4.30	14	302.6	273.2
None	-1836.5	4.39	13	325.3	292.5

## 3.5 Discussion

### 3.5.1 Constraints on Eccentricity

Here we briefly explore eccentric orbits for the two-transiting planets b and c. For each planet, we take  $e \sim \mathcal{U}(0, 0.7)$  and  $\omega \sim \mathcal{U}(0, 2\pi)$ . We only use kernel  $\mathbf{K}_{\mathbf{J1}}$  (eq. 3.2) to model the stellar activity. We find  $e_b = 0.30 \pm 0.04$ , which is  $\approx 50\%$  larger than our prior informed by a secondary eclipse event indicates. The corresponding finding of  $\omega_b = 3.01 \pm 0.27$  is also inconsistent with our adopted prior for  $\omega_b$ . The posterior distribution for  $e_c$  is concentrated at the upper bound (0.7), implying an overlapping orbit with AU Mic b. Orbital stability calculations presented in M20 indicate  $e_c < 0.2$ , so we assert our model is unable to accurately constrain its eccentricity. Our finding for  $e_c$  further indicates our detection of  $K_c$  may not be significant.

### 3.5.2 Sensitivity to Kernel Hyperparameters

Our analyses in section 3.3.3 make use of a fixed mean spot lifetime  $\eta_\tau = 100$  days and smoothing parameter  $\eta_\ell = 0.28$ . Here we determine how sensitive the recovered semi-amplitudes of AU Mic b and c are to these two parameters. We consider  $\eta_\tau \in \{40, 70, 100, 200, 300\}$  (days), and  $\eta_\ell \in \{0.15, 0.2, 0.25, 0.3, 0.35\}$ . We perform MAP and MCMC fits for all pairs of these two fixed parameters using  $\mathbf{K}_{\mathbf{J1}}$  (eq. 3.2) for a two-planet model. All other parameters adopt initial values and priors from Table 3.2. Results are summarized in Table 3.6.

We find  $K_b$  is only moderately sensitive to the values of each hyper-parameter, ranging from  $\sim 7\text{--}11 \text{ ms}^{-1}$ . With a larger spot lifetime,  $K_b$  tends towards larger values, indicating the GP is likely absorbing power from planet b with a more flexible model (smaller  $\eta_\tau$ ). However,  $K_b$  is relatively insensitive to the value of  $\eta_\ell$ . The range of values for  $K_c$  is larger, changing by nearly a factor of three. Unlike  $K_b$ ,  $K_c$  is more unstable and tends towards larger values when using a more flexible (smaller) spot lifetime. The reduced chi-squared statistic indicates the model is not over-fit in any of the cases performed, but is also larger

than unity by a several factors in most cases indicating our modeling is inadequate.

### 3.5.3 Planet Injection and Recovery

Here we assess the fidelity of our RV model applied to the AU Mic system through planetary injection and recovery tests. We first inject planetary signals into the RV data with well-defined semi-amplitudes, periods, and ephemerides ( $TC$ ). We arbitrarily choose  $TC = 2457147.36589$  for all injected cases. We consider 40 unique periods between 5.12345–100.12345 days, uniformly distributed in log-space. For the semi-amplitude  $K$ , we consider values from 1–10  $\text{m s}^{-1}$  with a step size of 1  $\text{m s}^{-1}$ , as well as values between 10–100  $\text{m s}^{-1}$  which are uniformly distributed in log-space (20 total values). In all cases, we include a model for AU Mic b with fixed  $P$  and  $TC$  such that  $K_b \sim \mathcal{N}(8.5, 2.5)$ . We first assess our recovery capabilities using a Gaussian prior for  $P$  such that  $P \sim \mathcal{N}(P_{\text{inj}}, P_{\text{inj}}/50)$  and a uniform prior for  $TC$  such that  $TC \sim \mathcal{U}(TC_{\text{inj}} \pm P_{\text{inj}}/2)$ . For each injected planet (one at a time), we run our MAP and MCMC analyses to determine the recovered  $K$  and corresponding uncertainty. The starting value for  $K$  and  $TC$  are always the injected values. We also consider the same injection and recovery test but with fixing  $P$  and  $TC$  to the injected value. We finally determine how susceptible our RV model is to pick out “fake”-planets by running these same two trials with no injected planets. Although there are no injected planets, we still run the same trials as the injected case with different initial values for  $K$ . A two-dimensional histogram of the recovered  $K$  as a fraction of the injected  $K$ , as well as the associated uncertainty (also as a fraction of the injected  $K$ ) for each case are shown in figs. 3.11 and 3.12 for the injected and non-injected cases, respectively.

In the case of injected planets, we find our RV-model is able to confidently recover semi-amplitudes down to a few  $\text{m s}^{-1}$  in this data set with a relative precision of  $\gtrsim 4\sigma$ . However, a closer inspection reveals the recovered semi-amplitudes are typically larger than the injected  $K$ , particularly for smaller injected values (1–5  $\text{m s}^{-1}$ ) that includes our measured semi-amplitude AU Mic c. When the ephemeris is known, we tend to poorly measure the smallest values of  $K$ , indicating the recovered  $TC$  in the non-fixed case is unlikely what we have

Table 3.6: MCMC results with different assumptions for the mean spot lifetime  $\eta_\tau$  and  $\eta_\ell$  using kernel  $\mathbf{K}_{\mathbf{J1}}$  (eq. 3.2). For each row, we fix the values of  $\eta_\tau$  and  $\eta_\ell$ . All other model parameters take on the initial values and priors from Table 3.2 for a two-planet model. We perform a MAP fit followed by MCMC sampling for each case. We report the nominal values and uncertainties for the semi-amplitudes of AU Mic b and c from the MCMC fitting, as well as the reduced chi-square statistic,  $\chi_{red}^2$  using the MAP-derived parameters. Uncertainties reported here for  $K_b$  and  $K_c$  are the average of the upper and lower uncertainties.

$\eta_\tau$ [days]	$\eta_\ell$	$K_b$ [m s <sup>-1</sup> ]	$K_c$ [m s <sup>-1</sup> ]	$\chi_{red}^2$
40	0.15	$8.79 \pm 1.47$	$7.38 \pm 1.65$	1.58
40	0.2	$8.84 \pm 1.30$	$8.51 \pm 1.33$	2.10
40	0.25	$8.23 \pm 1.17$	$9.05 \pm 1.17$	2.45
40	0.3	$7.41 \pm 1.08$	$9.13 \pm 1.13$	2.68
40	0.35	$6.95 \pm 0.98$	$9.23 \pm 1.05$	2.85
70	0.15	$8.74 \pm 1.24$	$6.88 \pm 1.30$	1.99
70	0.2	$10.32 \pm 1.13$	$5.90 \pm 1.07$	2.69
70	0.25	$10.45 \pm 1.04$	$4.76 \pm 0.95$	3.25
70	0.3	$9.61 \pm 0.91$	$4.16 \pm 0.89$	3.65
70	0.35	$9.18 \pm 0.82$	$3.94 \pm 0.83$	3.90
100	0.15	$9.28 \pm 1.17$	$5.88 \pm 1.08$	2.46
100	0.2	$10.85 \pm 1.00$	$4.73 \pm 0.98$	3.20
100	0.25	$10.78 \pm 0.95$	$3.78 \pm 0.87$	3.76
100	0.3	$9.81 \pm 0.85$	$3.63 \pm 0.80$	4.12
100	0.35	$9.22 \pm 0.80$	$3.60 \pm 0.77$	4.39
200	0.15	$9.38 \pm 0.98$	$4.01 \pm 0.96$	3.44
200	0.2	$11.04 \pm 0.89$	$3.35 \pm 0.84$	4.16
200	0.25	$11.09 \pm 0.87$	$3.38 \pm 0.77$	4.73
200	0.3	$10.14 \pm 0.84$	$4.51 \pm 0.76$	5.28
200	0.35	$9.06 \pm 0.73$	$4.77 \pm 0.66$	5.59
300	0.15	$9.32 \pm 0.92$	$3.84 \pm 0.87$	3.82
300	0.2	$10.60 \pm 0.88$	$3.78 \pm 0.81$	4.68
300	0.25	$10.42 \pm 0.80$	$4.99 \pm 0.74$	5.59
300	0.3	$10.51 \pm 0.76$	$4.52 \pm 0.68$	5.96
300	0.35	$9.89 \pm 0.75$	$4.41 \pm 0.68$	6.27

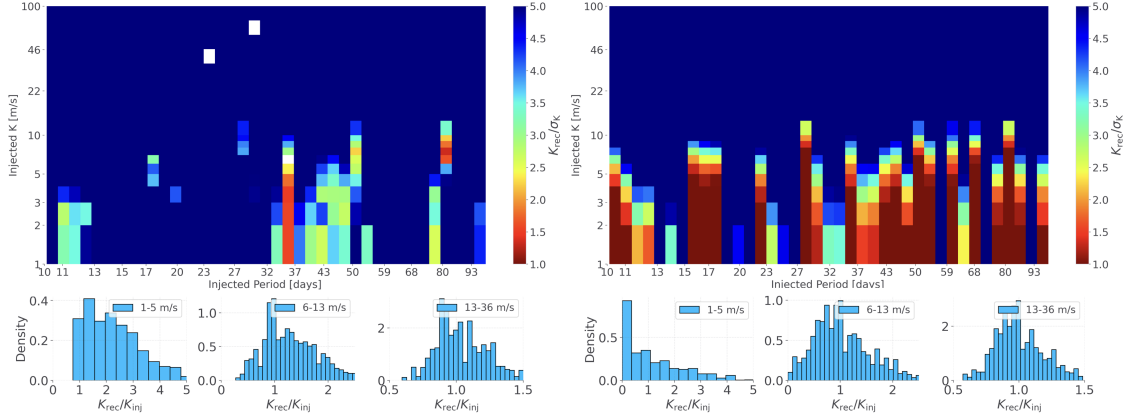


Figure 3.11: Histograms depicting our injection and recovery-test results. In the top row, we show the relative confidence interval of the recovered semi-amplitudes ( $K_{rec}$ ) derived from the MCMC analysis in the case of letting the ephemeris  $(P, TC)$  float (left) and fixing the ephemeris to the injected values (right). In the bottom row, we compare the recovered semi-amplitude to the injected value ( $K_{inj}$ ).

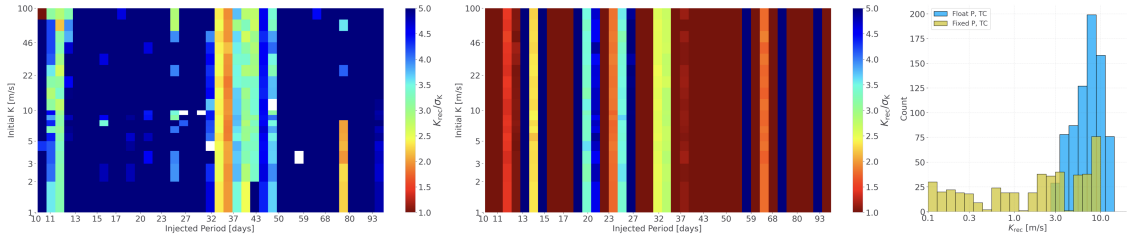


Figure 3.12: Histograms depicting the recovery of planetary signals without having injected any into the data. In panels 1 and 2, we show the relative confidence interval of the recovered semi-amplitudes ( $K_{rec}$ ) derived from the MCMC analysis in the case of letting the ephemeris  $(P, TC)$  float (left) and fixing the ephemeris to arbitrary the arbitrary  $TC=2457147.36589$  (middle). On the right, we show the recovered semi-amplitudes for each case.



injected. In the  $6\text{--}13\text{ m s}^{-1}$  range, which covers the recovered semi-amplitude of AU Mic b, we find that the accuracy of the recovered semi-amplitudes are  $\sim 50\%$ . So, while we quote a formal precision on the mass of AU Mic b to be  $M_b = 20.12^{+1.72}_{-1.57} M_{\oplus}$  ( $\sim 9\%$  precision), our injection and recovery tests indicate that the accuracy on the mass of AU Mic b is only known to a factor of two.

Unfortunately, attempts to recover non-injected planets are “unsuccessful”, in that our modeling finds strong evidence for planets we did not inject (fig. 3.12) in the case of allowing  $P$  and  $TC$  to float. A deeper investigation into the posteriors of such fits indicates certain parameters (primarily  $P$  and  $TC$ ) are typically not well-behaved and yield non-Gaussian distributions. When fixing  $P$  and  $TC$  to “nominal” values, our modeling does not tend to find such non-existent planets (fig. 3.12).

The confident recoveries of “fake”-planets in our tests indicate our GP model is flexible enough to find relatively (quasi)-stable islands in probability space with high confidence for  $K$  specifically. Although several peaks stand out in our periodogram analyses (figs. 3.8 and 3.9), more observations and/or more sophisticated modeling are needed to robustly claim these periods as statistically validated planets. We further note that the recovered values of  $K$  for the smallest injected values are inaccurate, indicating our measurement of  $K_c = 3.68\text{ m s}^{-1}$  is also moderately unconvincing, and is likely an overestimate given the behavior of all recoveries at this level of  $K$ . We finally note this analysis is limited by planets we do not account for in the model, which may impact our ability to recover certain combinations of  $P$  and  $TC$ . Further tests using several values for the injected  $TC$  may also yield different results. With these limitations in mind, we also provide an estimation of the upper-limit to the mass of AU Mic c. We find a  $5\sigma$  upper-limit to the semi-amplitude of AU Mic c of  $\leq 7.68\text{ m s}^{-1}$ , corresponding to a mass of  $\leq 20.13 M_{\oplus}$ .

### 3.5.4 Utility of RV-Color

Our chromatic kernel used in this work is an initial step to exploit the expected correlation of stellar activity versus wavelength by introducing a scaling relation between wavelengths

(eqs. 3.2 and 3.3). Here we examine the “RV-color” for our multi-wavelength dataset in order to further assess the correlation between our RVs with expected activity:

$$RV_{\text{color}}(t, \lambda, \lambda') = RV(t, \lambda) - RV(t, \lambda') \quad (3.6)$$

We first determine which nights contain nearly simultaneous measurements at unique wavelengths. We require observations to be within 0.3 days ( $\approx 6\%$  of one rotation period) of each other to minimize differences from rotationally modulated activity but to increase the number of pairs for our brief use. For each nearly simultaneous chromatic pair, we compute the “data-color” directly from the measured RVs as well as the “GP-color” by computing the differences between the two measurements and two GPs sampled at the identical times, respectively (such that  $\lambda' > \lambda$ ). This calculation requires knowledge of the parameters in order to remove the per-instrument zero points and realize each appropriate GP, so we make use of the MAP-derived parameters in Table 3.3 with kernel  $\mathbf{K}_{\mathbf{J2}}$  (eq. 3.3). The correlation between the data- and GP-color is shown in fig. 3.13. The agreement between the data and the model (weighted  $R^2 \approx 0.71$ ) indicates that our chromatic GP technique is doing a good job of reproducing the RV-color phenomenon for multiple wavelength pairs.

With a sufficient model for stellar activity, we expect the data and GP RV-color to match (up to white noise). Therefore, the “RV-color” between the data and GP may be used to further constrain (in future analyses) the model (and therefore prevent over-fitting) by including an effective L2 regularization penalty as follows:

$$\ln \mathcal{L} += -\Lambda \sum_t r_{\text{col}}(t)^2 \quad (3.7)$$

Here,  $\vec{r}_{\text{col}}$  is the vector of residuals between the GP and data RV-color.  $\Lambda > 0$  is a tunable hyperparameter whose value is directly correlated with the relative importance and confidence of the stellar activity model.  $+=$  represents the standard “addition assignment” operator.

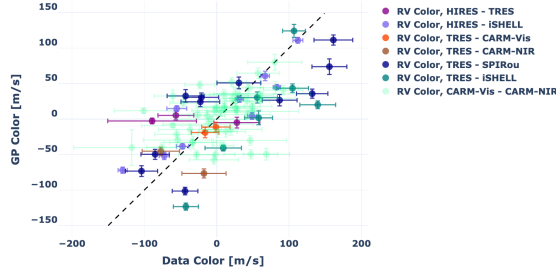


Figure 3.13: Here we plot the observed “RV-color” =  $RV(t, \lambda) - RV(t, \lambda')$  ( $\lambda' > \lambda$ ) from our 2019 and 2020 nights with nearly simultaneous measurements at unique wavelengths. These are plotted against the same RV-color difference predicted by our chromatic GP model using kernel  $\mathbf{K}_{J2}$ . Pairs consisting of CARMENES-Vis and CARMENES-NIR measurements are nearly transparent to make other pairs more visible. We do not plot pairs of SPIRou and iSHELL because they are tightly centered near zero. A dashed one-to-one line is also shown. The weighted coefficient of determination ( $R^2$ ) is  $\approx 0.68$ .

The vector  $\vec{r}_{col}$  may be computed for all pairs of wavelengths with (nearly)-simultaneous measurements, and each pair can make use of an identical or unique values of  $\Lambda$ . We finally note this regularization term is not limited to our assumption of a simple-scaling relation, and could also be used in the case of disjoint kernels.

### 3.5.5 Additional Caveats and Future Work

Kernels  $\mathbf{K}_{J1}$  (3.2) and  $\mathbf{K}_{J2}$  (eq. 3.3) make use of a scaling relation for stellar activity models at different wavelengths (spectrographs) where each activity model is drawn from a Gaussian process characterized by a covariance matrix utilizing all observations. Using such joint kernels yield fits with larger scatter than cases using disjoint QP kernels (one per-spectrograph, eq. 3.1). In the latter case, we find that although each activity model appears to be “in-phase” with one another, each GP exhibits unique features that are inconsistent with a simple scaling relation (fig. 3.3). With nightly sampling, it is difficult to determine whether the observed differences between disjoint GPs is indicative of inadequate sampling or an inadequate RV model (activity + planets). Further, all activity models used in this work make use of identical kernel hyperparameters (excluding the amplitude) which may further be an inadequate assumption. We expect the stellar rotation period

( $\eta_P$ ) to be identical across wavelengths (or nearly so), however it is not clear whether the mean activity timescale ( $\eta_\tau$ ) or period length scale ( $\eta_\ell$ ) in particular should be achromatic hyperparameters.

Our work further excluded per-spectrograph white noise jitter terms. We suspect this may be the source of our model’s ability to find planets we did not inject into the model, which we defer to future work (Section 3.5.3). The reduced- $\chi^2$  values in Tables 3.4 and 3.6 quantify the degree to which our models do not capture signals from possible additional planets, incorrect values for eccentricity and/or  $\omega$ , per-spectrograph systematics not included in the formal measurement uncertainties, stellar activity such as p-mode oscillations, convection noise, or longer time-scale variations. We choose not to combine these correlated noise terms into an assumed white noise jitter; there is no a priori reason to assume these potential additional sources of error are well-enough explained by an additional uncorrelated noise term, even if they may collectively be “reduced” to a normal distribution by our optimization routines.

More accurately characterizing the masses and orbits of AU Mic b and c may require a more sophisticated stellar activity model and more intensive multi-wavelength cadence. Our work further does not make use of activity indicators (e.g., Ca II H and K, H $\alpha$ ) or asymmetries in the cross-correlation function (e.g., the bisector inverse slope (BIS) or differential line width dLW; (132)) to help constrain the activity model (see 133). The **SERVAL** pipeline in particular provides a measure of the chromaticity (CRX) for both the CARMENES Vis and NIR datasets which we do not use in our modeling. For AU Mic, we expect that each spectrograph is precise enough to resolve first-order chromatic effects within their respective spectral grasp’s which will unfortunately make the formal uncertainties of each spectrograph larger. Further, our QP-based kernels are primarily intended to capture rotationally modulated activity induced from temperature inhomogeneities on the stellar surface. Although the flexibility of disjoint GPs likely captures other rotationally modulated effects such as convective blueshift and limb-darkening, it will not capture short-term activity such as flares. We finally note that more seasons with high-cadence RVs will

help mitigate the strong 1 year alias present in our dataset, and will help determine the correct periods for potential non-transiting planets.

### 3.6 Conclusion

In this work, we have developed two joint-Gaussian process kernels which begin to take into account the expected wavelength dependence of stellar activity through a simple-scaling relation. We apply our kernels to a dataset of AU Mic, which is composed of RVs from multiple facilities, and wavelengths ranging from visible to K-band. With our analyses, we report a refined mass of AU Mic b of  $M_b = 20.12^{+1.57}_{-1.72} M_{\oplus}$ , and provide a  $4.2\sigma$  mass estimate of the recently validated transiting planet AU Mic c to be  $M_c = 9.60^{+2.07}_{-2.31} M_{\oplus}$ , corresponding to a  $5\sigma$  upper limit of  $M_c \leq 20.13 M_{\oplus}$ . We also identify additional peaks present in the activity-filtered RVs, but such periods require more evidence for a robust validation given the overall flexibility of our RV model with an unknown ephemeris.

In Section 3.5.1, we find our model is unable to robustly constrain the eccentricity for AU Mic b or c. In section 3.5.2, we find the derived planetary semi-amplitudes for AU Mic b and c are moderately sensitive to the choice of kernel-parameters, indicating careful attention must be made when interpreting planetary masses with such a flexible model. Through injection and recovery tests in section 3.5.3, we further validate our RV-model by demonstrating our ability to recover planets down to  $\approx 10 \text{ m s}^{-1}$  when the orbit’s ephemeris is known. However, we find that the accuracy in the recovered semi-amplitudes is  $\sim 50\%$  at  $10 \text{ m s}^{-1}$ . In section 3.5.4, we introduce a method to further leverage the “RV-color” correlation between the observations and activity model through penalizing the objective function by including an effective L2 regularization term.

## Appendix A: optimize

`optimize`<sup>1</sup> is a generic, high-level optimization package in *Python*, which generalizes the Bayesian-inspired classes used in `RadVel`. The primary container (*Python* class) in `optimize` is referred to as an “OptProblem”; primary attributes for this object are then helper-types to 1. construct the model, 2. compare the data and model with an objective function, and 3. perform the optimization & sample posterior distributions via Markov-Chain Monte-Carlo (MCMC) methods. Many attributes (such as initial parameters) are shared in multiple layers of this hierarchy for easier access and extension with appropriate methods to propagate changes to each. `Optimize` does not re-implement specific optimization algorithms, but rather is intended to be high-level wrapper around such routines (e.g., currently `scipy.optimize` and `emcee`)

---

<sup>1</sup>Documentation: <https://optimize.readthedocs.io/en/latest/>

## Appendix B: Posterior Distributions

Here we show the posterior distributions for the relevant RV models employed in this work in Chapter 3. In each corner plot, blue lines correspond to the 50<sup>th</sup> percentile of the distribution. Upper and lower uncertainties correspond to the 84.1<sup>st</sup> and 15.9<sup>th</sup> percentiles, respectively.

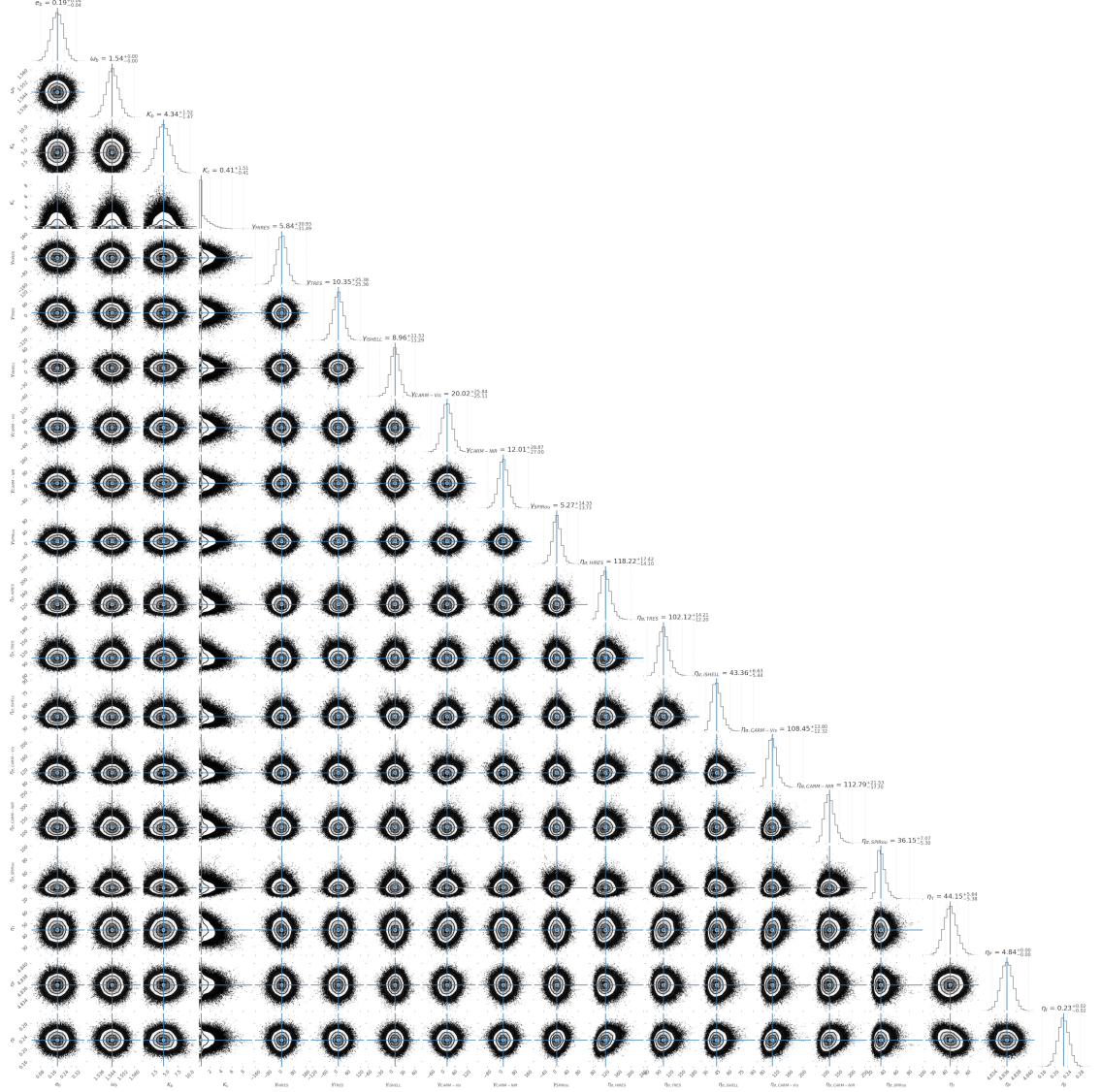


Figure B.1: Posterior distributions using disjoint QP kernels (eq. 3.1) for each spectrograph to model the stellar activity, including a two-planet model for the transiting planets b and c. The derived values for  $\eta_T$  suggests a more dynamic activity model than the  $FF'$  curve prediction suggests.



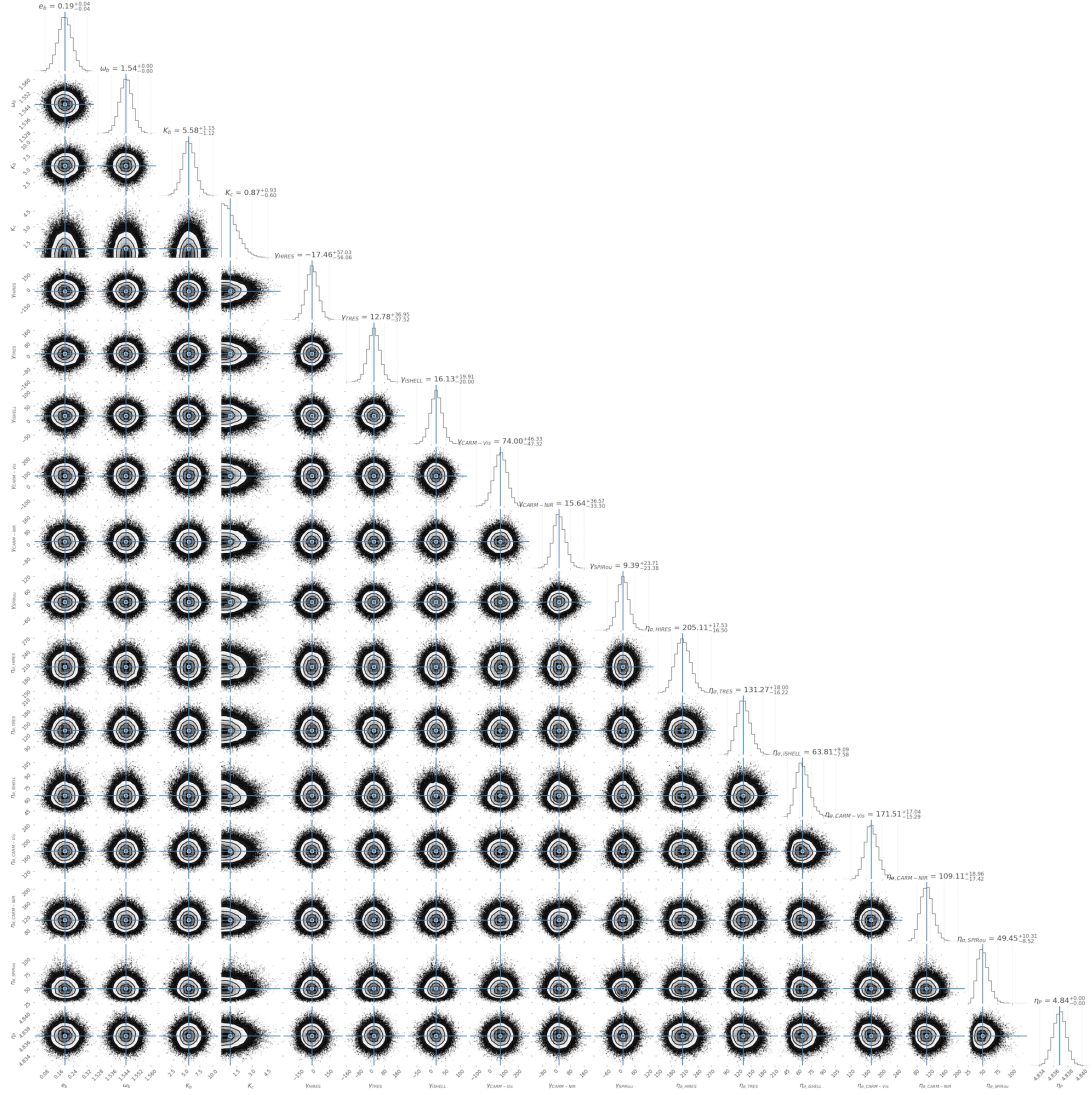


Figure B.2: Same as fig. B.1 but fixing  $\eta_\tau = 100$  days.

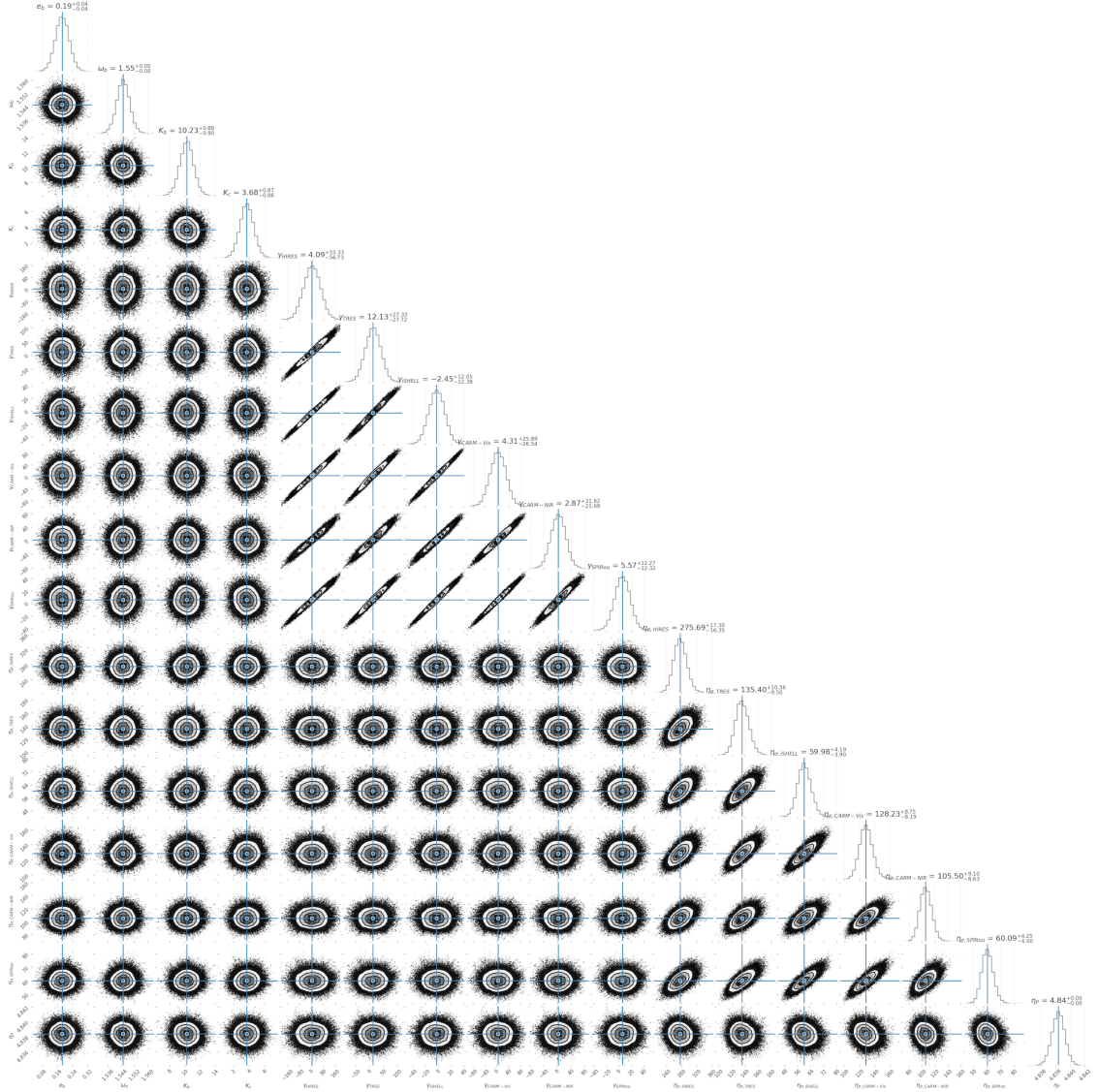


Figure B.3: Posterior distributions for a two-planet fit to the RVs using  $\mathbf{K}_{J1}$  (eq. 3.2) to model the stellar activity.

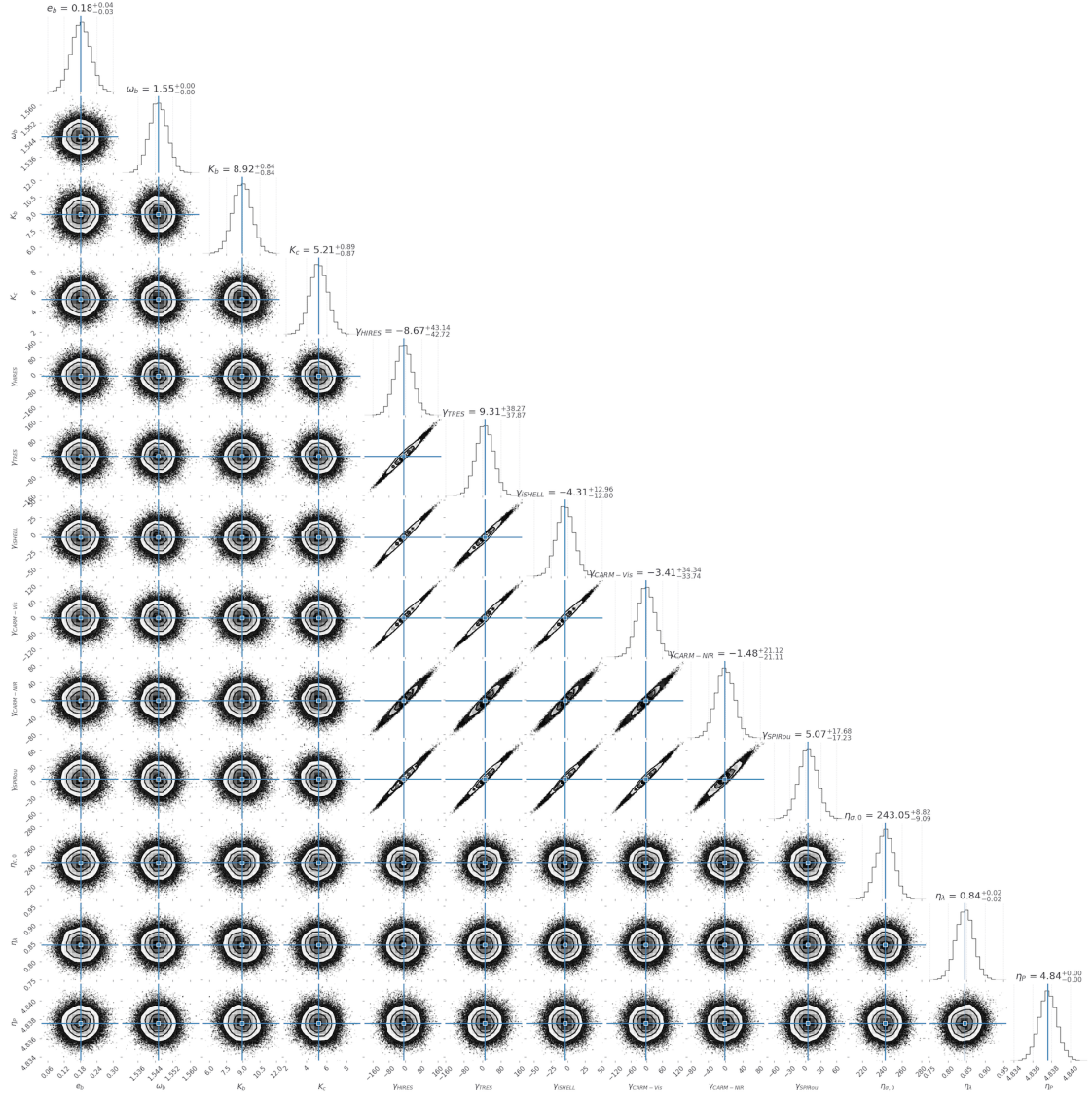


Figure B.4: Same as fig. B.3 but using  $\mathbf{K}_{J2}$  to model the stellar activity.

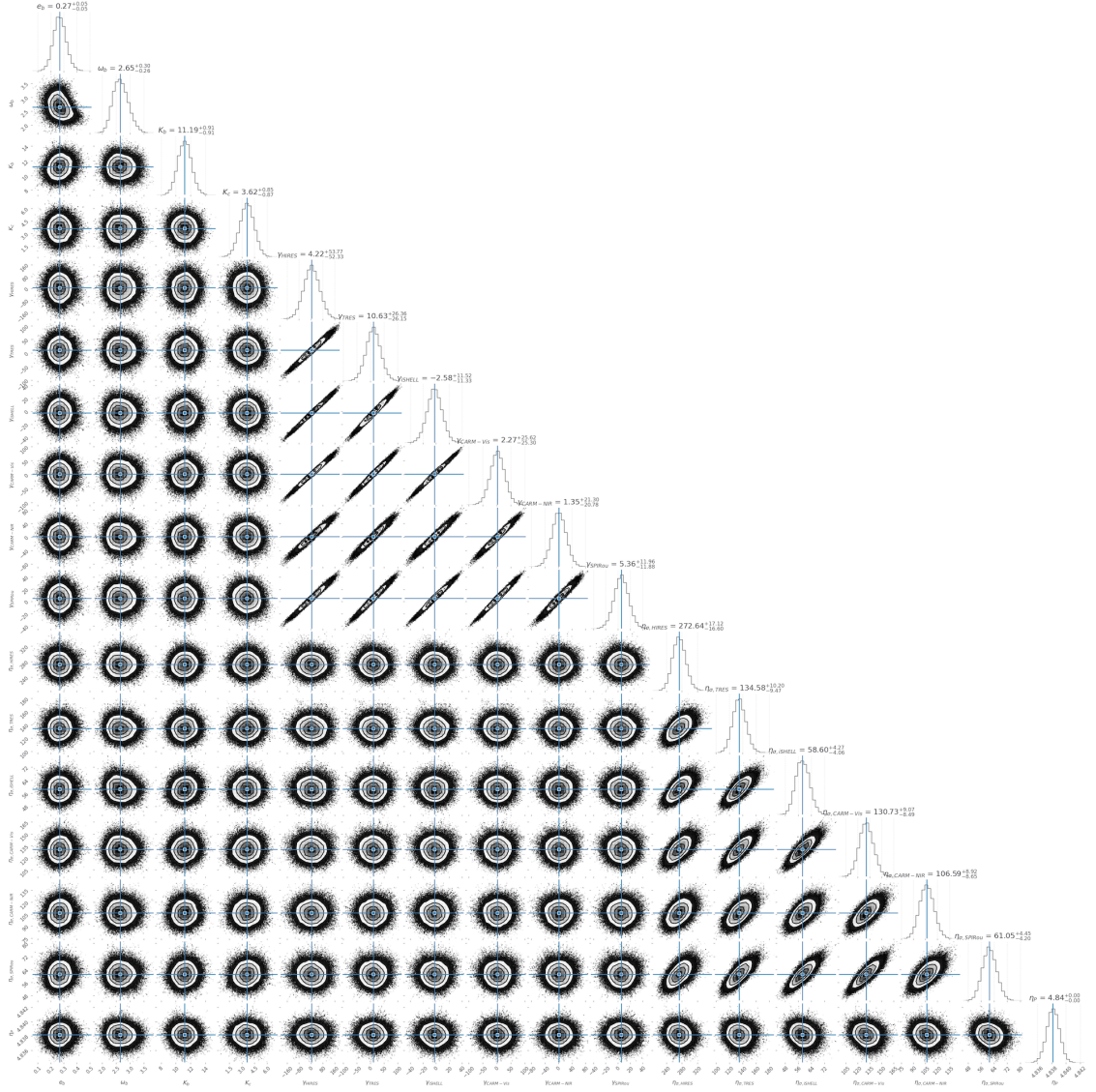


Figure B.5: Same as fig. B.3 but using less restrictive priors for  $e_b$  or  $\omega_c$ .

## Appendix C: RV Measurements

Table C.1: Nightly HARPS RVs analyzed in this work.

BJD	RV [ $\text{m s}^{-1}$ ]	$\sigma_{RV}$ [ $\text{m s}^{-1}$ ]
2452986.514817	73.91	4.81
2453157.898424	19.26	1.72
2453201.82345	-32.8	2.56
2453468.89237	-135.2	2.52
2453469.843534	-170.56	2.92
2453499.868255	-43.41	2.52
2453521.894368	-345.97	6.36
2453551.803998	-34.22	2.5
2453593.622139	137.84	3.33
2456568.510365	-244.53	2.16
2456569.500104	-32.99	1.8
2456570.565952	193.28	2.17
2456772.919271	-54.34	1.64
2456773.918979	-9.22	0.99
2456794.882288	-119.81	2.53
2456795.885873	66.36	2.91
2456797.857541	20.03	3.0
2456844.806163	162.85	2.18
2456982.539577	-65.03	1.8
2457223.648073	217.24	2.71
2457333.535731	94.85	1.29
2457493.891905	90.65	2.11
2457590.712986	73.08	1.4



2457904.813342	-287.06	3.36
2457917.892902	161.13	1.97
2458035.528955	-22.13	1.55
2458037.494745	-41.59	2.39
2458206.872213	-43.23	1.38
2458207.892023	33.78	1.56
2458208.884974	82.61	1.29
2458591.919473	120.82	1.42
2458594.904828	19.89	2.43
2458602.927758	9.22	1.47
2458605.916360	-248.46	2.33

Table C.2: Nightly HIRES RVs analyzed in this work.

BJD	RV [ $\text{m s}^{-1}$ ]	$\sigma_{RV}$ [ $\text{m s}^{-1}$ ]
2453182.049556	58.09	4.01
2453195.938633	-171.02	2.74
2453926.030459	-270.15	3.02
2453926.979641	271.86	3.18
2453927.920257	68.35	2.13
2453931.079663	-191.25	3.16
2453932.007322	256.77	2.76
2453932.978973	7.97	2.18
2453933.944291	162.29	2.36
2453934.930418	-159.79	2.73
2453960.942379	257.92	2.98
2453962.030949	5.08	2.28
2454636.072465	-9.82	2.53

2454688.871239	-133.07	2.46
2454808.692607	-83.96	3.06
2455015.018198	-140.72	2.86
2455371.044475	100.3	1.9
2455727.981919	35.73	2.89
2456638.683238	325.16	4.18
2458645.065398	-77.3	7.43
2459019.062251	-121.05	2.81
2459025.094631	-155.66	2.48
2459026.123675	399.32	3.35
2459028.098307	104.1	2.86
2459029.081905	14.31	2.53
2459030.078281	-131.6	2.19
2459031.106844	414.91	3.41
2459032.105577	-138.95	2.71
2459035.092001	-76.31	2.26
2459036.101597	329.39	3.4
2459040.11603	3.72	2.12
2459041.117761	153.21	3.14
2459044.942379	-0.97	2.22
2459051.9219	92.94	2.44
2459067.855784	-21.57	3.09
2459068.895396	-30.19	2.4
2459071.907618	43.81	3.37
2459072.852897	-8.9	2.74
2459077.821906	-44.12	2.71
2459078.813958	-31.15	2.45
2459086.849156	-147.83	3.51

2459087.868995	0.97	2.58
2459088.849805	139.3	2.57
2459089.824376	-38.53	3.28
2459094.815792	-127.27	2.67
2459097.855698	-16.26	2.6
2459099.761856	-139.97	3.05
2459101.904682	-82.58	2.51
2459114.829534	-6.09	2.08
2459115.91498	-92.15	2.61
2459117.857924	48.2	2.29
2459121.710044	11.92	2.38
2459122.709275	58.74	2.34
2459123.703587	20.0	2.6
2459151.692854	40.18	2.41
2459153.753326	95.26	2.73
2459181.680326	42.79	2.6
2459187.682871	54.26	2.47
2459188.689611	-6.89	2.6
2459189.684349	-81.15	2.86

Table C.3: Nightly NIRSPEC RVs analyzed in this work.

BJD	RV [ $\text{m s}^{-1}$ ]	$\sigma_{RV}$ [ $\text{m s}^{-1}$ ]
2453522.56	48.5	50.0
2453523.55	-19.5	50.0
2453596.37	111.5	50.0
2453597.38	19.5	50.0
2453669.19	113.5	50.0



2453670.2	262.5	50.0
2453928.5	-74.5	50.0
2453929.45	-148.5	50.0
2453930.46	-93.5	50.0
2453931.4	-24.5	50.0
2454308.43	123.5	50.0
2454309.41	-166.5	50.0
2454311.4	20.5	50.0
2454312.36	-157.5	50.0

Table C.4: Nightly CSHELL RVs analyzed in this work.

BJD	RV [ $\text{m s}^{-1}$ ]	$\sigma_{RV}$ [ $\text{m s}^{-1}$ ]
2455455.85303	16.79	38.76
2455479.800206	41.04	26.96
2455480.768983	143.4	56.64
2455482.756068	136.64	22.11
2455523.7002290003	0.0	20.78
2455752.0995830004	43.59	27.48
2455755.0752310003	141.67	44.57
2455758.967657	-17.29	31.52
2455791.812748	123.61	54.8
2455793.8316450003	234.74	10.87
2456844.9609169997	-35.3	15.47
2456917.743247	-36.65	21.07
2457275.8463990004	-115.88	26.14
2457551.12512	-102.38	51.72
2457555.058318	-150.06	20.78

2457564.0072459998	-198.34	30.4
2457570.063826	82.72	36.9
2457587.023049	-245.01	18.85
2457598.976608	-90.04	25.01
2457618.963993	8.92	19.22
2457619.947171	-72.55	21.1

Table C.5: Nightly TRES RVs analyzed in this work.

BJD	RV [ $\text{m s}^{-1}$ ]	$\sigma_{RV}$ [ $\text{m s}^{-1}$ ]
2456573.68979	-128.0	11.6
2456574.640606	-45.2	11.8
2456575.669816	183.9	14.4
2456576.660338	-186.6	10.3
2456577.632961	203.9	12.3
2456578.625675	-68.1	11.9
2456579.634451	-64.0	13.8
2456580.634669	173.3	13.7
2456581.610641	-117.8	11.3
2456582.623658	101.1	21.4
2456583.619796	-35.2	9.7
2456584.624069	-18.7	11.0
2456585.596255	59.0	11.7
2456586.617077	-22.2	12.7
2456587.611581	0.0	11.7
2456588.591012	-33.7	11.6
2456589.602899	45.0	11.8
2456590.622533	-64.4	12.1

2456605.581655	-250.0	13.7
2456606.565507	225.6	8.4
2456607.563214	-172.0	12.1
2456608.58807	-11.5	10.6
2456609.587085	211.2	13.7
2456610.565465	-233.4	15.0
2456611.571286	213.0	9.2
2456615.560722	-193.0	13.6
2456616.572477	176.9	13.8
2456622.557557	-102.5	19.3
2456624.552961	85.6	46.8
2456625.563003	38.7	24.7
2458646.96613	49.9	24.2
2458647.964611	34.3	22.0
2458648.961007	-44.6	17.8
2458649.958409	-41.2	18.9
2458650.97301	164.3	16.2
2458651.966405	116.1	17.5
2458652.981466	-33.8	24.0
2458657.953559	13.6	15.7
2458658.932441	-107.5	17.0
2458659.912405	84.9	19.9
2458665.924079	130.6	17.8
2458674.932143	198.8	14.2
2458677.882169	-99.1	20.1
2458685.884899	96.1	35.5
2458689.846153	110.1	14.7
2458693.842764	-74.1	24.1

2458730.740018	17.1	23.4
2458731.739653	-35.0	23.9
2458738.70382	145.2	32.6
2458742.696035	-86.4	40.1
2458744.700854	234.4	25.3
2458745.730511	-65.9	40.3
2458758.650170	42.1	25.3
2458759.694882	114.5	28.3
2458761.645681	-117.3	17.2
2458762.677499	144.6	21.8
2458767.656488	107.5	33.1
2458768.653311	83.7	30.6
2458769.635106	15.1	22.5
2458770.623329	-112.3	18.2
2458771.612582	-144.9	21.1
2458772.628816	120.2	22.4
2458773.638865	91.1	25.1
2458774.591042	-51.3	25.3
2458775.598544	-135.9	24.1
2458779.573710	-86.3	24.1
2458780.566456	-148.0	20.2
2458782.572973	29.7	19.0
2458783.561459	123.9	30.0
2458784.56098	-121.1	21.7
2458786.591881	-45.4	22.6
2458787.627174	-2.0	29.9
2458788.570062	211.2	22.7

Table C.6: Nightly iSHELL RVs analyzed in this work.

BJD	RV [ $\text{m s}^{-1}$ ]	$\sigma_{RV}$ [ $\text{m s}^{-1}$ ]
2457684.759584	76.97	4.94
2457698.745971	47.96	3.05
2457699.710324	47.8	14.07
2457850.129559	87.59	7.24
2457856.130267	-33.33	3.41
2457923.120317	-1.31	4.77
2457931.026094	-15.53	1.59
2457940.000525	-7.44	0.26
2457982.918015	-2.11	11.34
2457983.911491	-25.53	31.67
2457984.906727	76.12	7.17
2458046.688896	-53.89	6.97
2458047.677872	20.45	9.09
2458048.684528	1.5	7.03
2458049.677166	-68.12	11.49
2458660.089282	8.42	3.31
2458666.92506	42.5	2.21
2458675.084455	71.1	4.86
2458739.930751	85.7	4.12
2458760.71097	-48.38	4.51
2458761.729422	-96.54	3.37
2458762.730214	16.08	6.35
2458763.779074	-14.43	3.17
2458764.766543	18.96	5.06
2458765.71105	-39.79	7.94

2458795.700288	-59.42	3.14
2458796.706964	-0.86	5.37
2458798.695629	32.0	4.13
2458799.69492	-22.28	9.62
2459069.985765	67.29	11.02
2459071.979622	24.53	3.5
2459086.915335	-5.96	4.43
2459087.917716	68.09	13.17
2459088.900423	39.07	5.6
2459089.900047	20.73	7.19
2459090.897927	50.16	4.41
2459115.810803	-7.73	5.78
2459117.805977	-23.08	3.53
2459118.807183	-12.72	4.15
2459119.813063	3.98	5.34
2459120.804824	-28.18	4.32
2459122.88224	3.77	4.62
2459123.807924	-16.94	5.09
2459143.789273	-35.3	5.73
2459145.789894	0.86	9.38
2459147.782831	-7.73	4.04

Table C.7: Nightly IRD RVs analyzed in this work.

BJD	RV [ $\text{m s}^{-1}$ ]	$\sigma_{RV}$ [ $\text{m s}^{-1}$ ]
2458650.116682	-36.37	2.06
2458653.123778	5.82	4.63
2458654.116977	-62.9	1.88

2458655.126277	42.79	1.75
2458679.945743	1.82	5.4
2458771.845784	-1.82	3.99

Table C.8: Nightly CARMENES-NIR RVs analyzed in this work.

BJD	RV [ $\text{m s}^{-1}$ ]	$\sigma_{RV}$ [ $\text{m s}^{-1}$ ]
2458678.567915	92.38	46.13
2458679.537705	315.17	54.39
2458680.53478	247.69	65.59
2458684.568375	437.36	75.05
2458686.548525	275.14	49.79
2458687.578395	201.29	45.37
2458688.584370	86.47	46.79
2458690.55771	180.81	23.17
2458691.505425	276.31	30.81
2458693.54918	-19.49	18.84
2458694.59554	164.36	19.65
2458695.53909	-3.88	25.06
2458696.523080	41.45	15.91
2458698.51838	-112.18	13.87
2458699.48421	43.11	18.82
2458700.47701	-12.46	23.43
2458701.471955	-38.69	30.48
2458702.50203	-267.32	55.65
2458704.48929	-7.34	25.96
2458706.498265	-60.66	24.28
2458711.444815	-64.13	25.69

2458712.45243	-208.9	30.92
2458714.507735	-1.04	29.74
2458715.454715	104.33	19.43
2458718.45001	10.36	23.92
2458723.46396	-10.17	29.09
2458724.419910	-4.56	29.82
2458727.47503	-162.58	33.76
2458742.39457	-78.27	23.94
2458743.368875	105.08	32.28
2458744.35226	96.0	17.59
2458745.395085	-0.64	29.71
2458755.39838	-10.29	41.43
2458757.375210	-54.66	41.67
2458759.369515	121.73	27.43
2458760.30872	10.36	28.45
2458761.35095	-120.87	25.35
2458763.336130	26.53	27.49
2458765.32907	-24.44	46.17
2458766.329605	-141.11	33.1
2459049.54651	177.28	83.51
2459050.5627	326.43	75.53
2459051.54861	164.54	58.18
2459059.517	128.17	38.35
2459060.56397	0.64	45.11
2459061.51774	-1.64	26.11
2459067.51658	-22.7	35.8
2459070.49213	-161.95	47.51
2459076.47969	53.98	28.45



2459078.48314	-53.38	47.45
2459079.51194	84.71	32.93
2459081.44324	-7.63	44.14
2459085.4860900003	-66.12	30.86
2459086.4707	-5.4	35.27
2459087.44822	43.18	42.15
2459095.462660	13.58	28.27
2459098.44795	15.8	34.37
2459099.41347	0.86	35.8
2459148.30047	-76.46	68.62
2459154.2969	25.34	66.01
2459161.27302	-70.52	61.17
2459170.25901	-35.74	60.54

Table C.9: Nightly CARMENES-Vis RVs analyzed in this work.

BJD	RV [ $\text{m s}^{-1}$ ]	$\sigma_{RV}$ [ $\text{m s}^{-1}$ ]
2458678.568125	-69.66	29.45
2458679.537290	241.65	40.59
2458680.53527	79.92	15.96
2458684.568335	232.51	25.58
2458686.54842	177.2	16.04
2458687.578910	-17.01	20.79
2458688.584365	-96.42	19.21
2458690.5572350	114.83	11.18
2458691.505425	155.65	13.93
2458693.549395	-100.78	8.52
2458694.59568	135.7	6.79

2458695.53932	39.93	10.69
2458696.522970	57.79	6.7
2458698.518795	-108.57	4.86
2458699.484225	81.68	8.55
2458700.47709	10.01	6.31
2458701.472325	-1.34	7.9
2458702.502	-163.13	16.45
2458704.489635	79.4	7.75
2458706.498955	-53.41	13.14
2458711.445175	-68.26	9.3
2458712.452575	-145.53	8.27
2458714.507445	74.89	11.13
2458715.454290	119.79	6.96
2458718.449865	-8.15	7.88
2458723.46386	10.82	9.14
2458724.42014	32.17	9.24
2458727.47467	-120.64	15.58
2458742.394525	-111.51	6.47
2458743.36923	109.79	10.05
2458744.35274	44.66	6.63
2458745.394785	-8.64	10.77
2458755.399070	-52.31	12.96
2458757.37524	-40.49	11.8
2458759.369535	173.63	10.1
2458760.30896	-50.26	9.67
2458761.350815	-127.71	8.52
2458763.33635	21.39	6.78
2458765.32879	-83.71	9.85

2458766.32998	-150.2	7.98
2459049.54617	-9.06	23.94
2459050.56301	261.02	21.89
2459051.54856	-21.26	27.7
2459059.51739	21.86	12.02
2459060.56385	56.21	15.25
2459061.51767	3.43	9.96
2459067.51635	-61.79	14.71
2459070.49224	-120.99	17.32
2459076.47973	74.87	9.62
2459078.48285	-66.09	12.86
2459079.51202	159.74	17.82
2459081.4433	18.72	16.94
2459085.48611	-103.96	11.19
2459086.47053	0.0	11.41
2459087.44817	-22.76	10.14
2459095.46273	-17.99	15.28
2459098.44771	36.94	14.87
2459099.41364	1.26	13.44
2459113.41579	77.58	40.76
2459148.3007	-199.06	41.82
2459154.29727	80.14	23.03
2459161.27325	-25.96	17.31
2459170.25874	-52.59	15.02

Table C.10: Nightly MINERVA-Australis RVs analyzed in this work.

BJD	RV [m s <sup>-1</sup> ]	$\sigma_{RV}$ [m s <sup>-1</sup> ]
2458683.150648	89.06	38.22
2458684.165833	208.9	10.54
2458711.967436	-67.42	12.5
2458716.998287	-61.47	10.95
2458719.003218	175.13	22.44
2458720.062263	81.08	6.24
2458725.959649	32.34	104.73
2458738.040897	-55.32	7.36
2458739.963764	235.89	6.39
2458740.989093	-125.63	5.43
2458741.999722	-128.95	8.06
2458743.006845	0.0	5.15
2458792.965243	-13.18	9.52

Table C.11: Nightly CHIRON RVs analyzed in this work.

BJD	RV [m s <sup>-1</sup> ]	$\sigma_{RV}$ [m s <sup>-1</sup> ]
2458740.72096	1.48	45.24
2458741.713716	149.09	46.54
2458742.711554	-54.11	37.64
2458762.643643	112.47	56.45
2458763.64337	-44.57	36.34
2458764.629147	72.97	42.89
2458765.631185	-310.79	58.25
2458766.614416	-169.88	44.79
2458795.574927	51.27	68.8
2458796.570968	-1.48	71.87

2458797.56992	-11.17	37.07
2458798.597397	359.32	52.94

Table C.12: Nightly SPIRou RVs analyzed in this work.

BJD	RV [ $\text{m s}^{-1}$ ]	$\sigma_{RV}$ [ $\text{m s}^{-1}$ ]
2458744.8212	59.5	5.0
2458750.7542	-18.2	5.0
2458751.7453	-52.4	5.0
2458752.7898	27.9	5.0
2458758.7288	51.3	5.0
2458759.8053	69.2	5.0
2458760.7278	-29.6	5.0
2458761.7305	-87.2	5.0
2458762.7315	-2.9	5.0
2458764.7571	34.5	5.0
2458765.7694	-39.8	5.0
2458769.7438	22.1	5.0
2458770.7407	-41.6	5.0
2458771.7212	-55.8	5.0
2458772.7416	19.4	5.0
2458787.7155	28.3	5.0
2458788.7045	41.3	5.0
2458789.7367	-32.6	5.0
2458790.701	-90.1	5.0
2458791.6983	2.1	5.0
2458792.6976	19.1	5.0
2458796.6859	-13.5	5.0

2458797.7098	19.7	5.0
2458798.6873	27.0	5.0
2458799.6883	-10.3	5.0
2458800.6896	-46.2	5.0
2458801.6873	0.0	5.0

## Appendix D: Fitting the Full RV Dataset

Here we present fits to the full radial velocity dataset (see section 3.2). Although the baseline of the full dataset is nearly 17 years (first epoch in Dec. 2003), the uncertainties for the period and time of transit for AU Mic b and c are small enough to be fixed (see Table 3.2). We only use kernel  $\mathbf{K}_{\mathbf{J2}}$  (eq. 3.3) to model the stellar activity as we do not seek to fit for per-spectrograph activity amplitudes for datasets with  $\lesssim 10$  measurements. A first-order estimation for the secular acceleration (134) of AU Mic is negligible given the precision of our measurements and baseline ( $\Delta \text{RV} < 3 \text{ cm s}^{-1}$ ), so no long-term linear or quadratic trend is used. The posteriors are shown in figure D.3. The GPs and Keplerian model are shown in figure D.1.

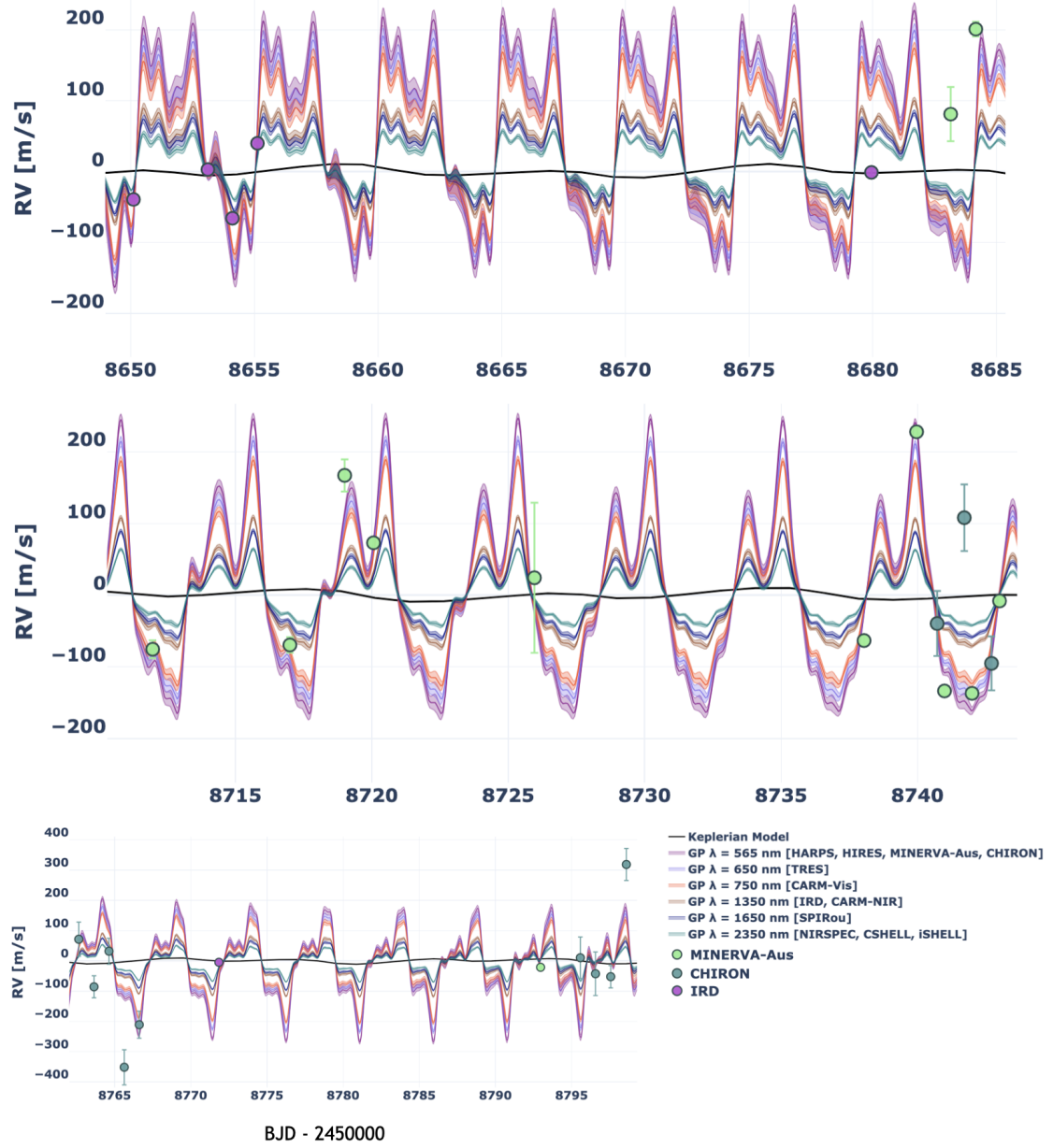


Figure D.1: Here we show a subset of the 2019 RVs using kernel  $\mathbf{K}_{J2}$  (eq. 3.2) to model the stellar activity and including the full RV dataset. Although we do not include the MINERVA-Australis or IRD RVs in our primary fits in section 3.3, we find they are generally consistent with our stellar activity model. We do not show the phased CHIRON RVs due to their larger residuals.



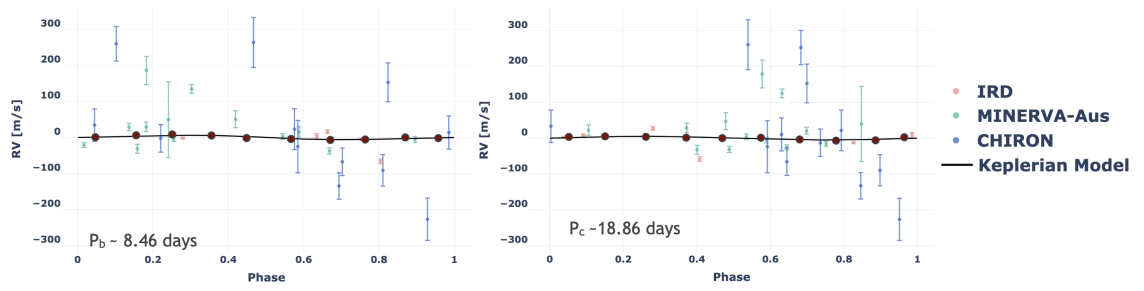


Figure D.2: Same as fig. D.1, but showing the phased RVs.

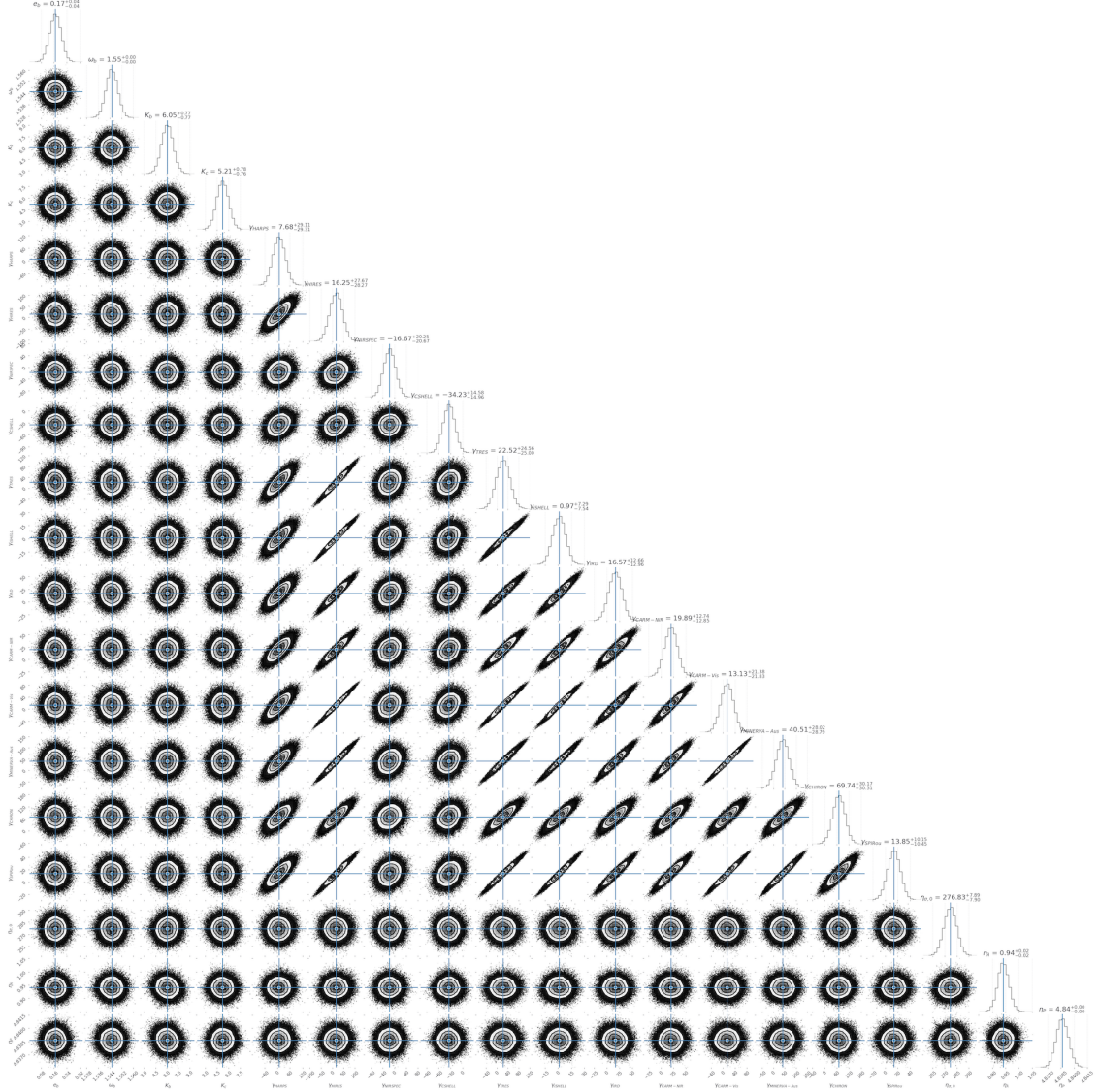


Figure D.3: Posterior distributions for a two-planet fit to the full RV dataset using  $\mathbf{K}_{J2}$  to model the stellar activity. Blue lines correspond to the 50<sup>th</sup> percentile of the distribution. Upper and lower uncertainties correspond to the 15.9<sup>th</sup> and 84.1<sup>st</sup> percentiles, respectively. The semi-amplitude  $K_b$  is  $\approx 30\%$  smaller than the subset of 2019-2020 data yields (Table 3.3), however  $K_c$  is relatively unchanged.

## Bibliography

- [1] J. M. Jenkins, J. D. Twicken, S. McCauliff, J. Campbell, D. Sanderfer, D. Lung, M. Mansouri-Samani, F. Girouard, P. Tenenbaum, T. Klaus, J. C. Smith, D. A. Caldwell, A. D. Chacon, C. Henze, C. Heiges, D. W. Latham, E. Morgan, D. Swade, S. Rinehart, and R. Vanderspek, “The TESS science processing operations center,” in *Software and Cyberinfrastructure for Astronomy IV*, ser. , vol. 9913, Aug. 2016, p. 99133E.
- [2] E. Martioli, G. Hébrard, A. C. M. Correia, J. Laskar, and A. Lecavelier des Etangs, “New constraints on the planetary system around the young active star AU Mic. Two transiting warm Neptunes near mean-motion resonance,” *arXiv e-prints*, p. arXiv:2012.13238, Dec. 2020.
- [3] B. Klein, J.-F. Donati, C. Moutou, X. Delfosse, X. Bonfils, E. Martioli, P. Fouqué, R. Cloutier, É. Artigau, R. Doyon, G. Hébrard, J. Morin, J. Rameau, P. Plavchan, and E. Gaidos, “Investigating the young AU Mic system with SPIRou: large-scale stellar magnetic field and close-in planet mass,” , vol. 502, no. 1, pp. 188–205, Mar. 2021.
- [4] NASA Exoplanet Archive, “Confirmed planets table,” 2019. [Online]. Available: <https://catcopy.ipac.caltech.edu/doi/doi.php?id=10.26133/NEA1>
- [5] J. Chen and D. Kipping, “Probabilistic Forecasting of the Masses and Radii of Other Worlds,” , vol. 834, no. 1, p. 17, Jan. 2017.
- [6] M. Perryman, *The Exoplanet Handbook*. Cambridge University Press, 2011.

- [7] P. Figueira, F. Pepe, C. H. F. Melo, N. C. Santos, C. Lovis, M. Mayor, D. Queloz, A. Smette, and S. Udry, “Radial velocities with CRIRES. Pushing precision down to 5-10 m/s,” , vol. 511, p. A55, Feb. 2010.
- [8] M. Mayor and D. Queloz, “A Jupiter-mass companion to a solar-type star,” , vol. 378, pp. 355–359, Nov. 1995.
- [9] P. Plavchan, D. Latham, S. Gaudi, J. Crepp, X. Dumusque, G. Furesz, A. Vanderburg, C. Blake, D. Fischer, L. Prato, R. White, V. Makarov, G. Marcy, K. Stapelfeldt, R. Haywood, A. Collier-Cameron, A. Quirrenbach, S. Mahadevan, G. Anglada, and P. Muirhead, “Radial Velocity Prospects Current and Future: A White Paper Report prepared by the Study Analysis Group 8 for the Exoplanet Program Analysis Group (ExoPAG),” *arXiv e-prints*, Mar. 2015.
- [10] D. A. Fischer, G. Anglada-Escude, P. Arriagada, R. V. Baluev, J. L. Bean, F. Bouchy, L. A. Buchhave, T. Carroll, A. Chakraborty, J. R. Crepp, R. I. Dawson, S. A. Didams, X. Dumusque, J. D. Eastman, M. Endl, P. Figueira, E. B. Ford, D. Foreman-Mackey, P. Fournier, G. Fűrész, B. S. Gaudi, P. C. Gregory, F. Grundahl, A. P. Hatzes, G. Hébrard, E. Herrero, D. W. Hogg, A. W. Howard, J. A. Johnson, P. Jorden, C. A. Jurgenson, D. W. Latham, G. Laughlin, T. J. Loredo, C. Lovis, S. Mahadevan, T. M. McCracken, F. Pepe, M. Perez, D. F. Phillips, P. P. Plavchan, L. Prato, A. Quirrenbach, A. Reiners, P. Robertson, N. C. Santos, D. Sawyer, D. Segransan, A. Sozzetti, T. Steinmetz, A. Szentgyorgyi, S. Udry, J. A. Valenti, S. X. Wang, R. A. Wittenmyer, and J. T. Wright, “State of the Field: Extreme Precision Radial Velocities,” , vol. 128, no. 6, p. 066001, Jun. 2016.
- [11] A. A. West, S. L. Hawley, L. M. Walkowicz, K. R. Covey, N. M. Silvestri, S. N. Raymond, H. C. Harris, J. A. Munn, P. M. McGehee, Ž. Ivezić, and J. Brinkmann, “Spectroscopic Properties of Cool Stars in the Sloan Digital Sky Survey: An Analysis of Magnetic Activity and a Search for Subdwarfs,” , vol. 128, pp. 426–436, Jul 2004.

- [12] G. Basri, L. M. Walkowicz, N. Batalha, R. L. Gilliland, J. Jenkins, W. J. Borucki, D. Koch, D. Caldwell, A. K. Dupree, D. W. Latham, S. Meibom, S. Howell, and T. Brown, “Photometric Variability in Kepler Target Stars: The Sun Among Starsa First Look,” , vol. 713, pp. L155–L159, Apr. 2010.
- [13] P. Robertson, A. Roy, and S. Mahadevan, “Stellar Activity Mimics a Habitable-zone Planet around Kapteyn’s Star,” , vol. 805, p. L22, Jun. 2015.
- [14] E. R. Newton, J. Irwin, D. Charbonneau, Z. K. Berta-Thompson, and J. A. Dittmann, “The Impact of Stellar Rotation on the Detectability of Habitable Planets around M Dwarfs,” , vol. 821, no. 1, p. L19, Apr 2016.
- [15] A. Vanderburg, P. Plavchan, J. A. Johnson, D. R. Ciardi, J. Swift, and S. R. Kane, “Radial velocity planet detection biases at the stellar rotational period,” , vol. 459, no. 4, pp. 3565–3573, Jul 2016.
- [16] E. L. Martín, E. Guenther, C. Del Burgo, F. Rodler, C. Álvarez, C. Baffa, V. J. S. Béjar, J. A. Caballero, R. Deshpande, P. Esparza, M. López Morales, A. Moitinho, D. Montes, M. M. Montgomery, E. Pallé, R. Tata, L. Valdivielso, and M. R. Zapatero Osorio, “NAHUAL: A Next-Generation Near Infrared Spectrograph for the GTC,” in *Pathways Towards Habitable Planets*, ser. Astronomical Society of the Pacific Conference Series, V. Coudé du Foresto, D. M. Gelino, and I. Ribas, Eds., vol. 430, Oct. 2010, p. 181.
- [17] N. I. Mahmud, C. J. Crockett, C. M. Johns-Krull, L. Prato, P. M. Hartigan, D. T. Jaffe, and C. A. Beichman, “Starspot-induced Optical and Infrared Radial Velocity Variability in T Tauri Star Hubble I 4,” , vol. 736, p. 123, Aug. 2011.
- [18] C. J. Crockett, N. I. Mahmud, L. Prato, C. M. Johns-Krull, D. T. Jaffe, P. M. Hartigan, and C. A. Beichman, “A Search for Giant Planet Companions to T Tauri Stars,” , vol. 761, p. 164, Dec. 2012.

- [19] G. Anglada-Escudé, R. P. Butler, A. Reiners, H. R. A. Jones, M. Tuomi, J. S. Jenkins, J. R. Barnes, S. S. Vogt, and M. Zechmeister, “Surfing the photon noise: New techniques to find low-mass planets around M dwarfs,” *Astronomische Nachrichten*, vol. 334, p. 184, Feb. 2013.
- [20] R. C. Marchwinski, S. Mahadevan, P. Robertson, L. Ramsey, and J. Harder, “Toward Understanding Stellar Radial Velocity Jitter as a Function of Wavelength: The Sun as a Proxy,” , vol. 798, p. 63, Jan. 2015.
- [21] A. Reiners, J. L. Bean, K. F. Huber, S. Dreizler, A. Seifahrt, and S. Czesla, “Detecting Planets Around Very Low Mass Stars with the Radial Velocity Method,” , vol. 710, pp. 432–443, Feb. 2010.
- [22] A. Tanner, R. White, J. Bailey, C. Blake, G. Blake, K. Cruz, A. J. Burgasser, and A. Kraus, “Keck NIRSPEC Radial Velocity Observations of Late-M Dwarfs,” , vol. 203, p. 10, Nov. 2012.
- [23] P. Gao, P. Plavchan, J. Gagné, E. Furlan, M. Bottom, G. Anglada-Escudé, R. White, C. L. Davison, C. Beichman, C. Brinkworth, J. Johnson, D. Ciardi, K. Wallace, B. Mennesson, K. von Braun, G. Vasisht, L. Prato, S. R. Kane, A. Tanner, T. J. Crawford, D. Latham, R. Rougeot, C. S. Geneser, and J. Catanzarite, “Retrieval of Precise Radial Velocities from Near-infrared High-resolution Spectra of Low-mass Stars,” , vol. 128, no. 10, p. 104501, Oct. 2016.
- [24] J. L. Bean, A. Seifahrt, H. Hartman, H. Nilsson, G. Wiedemann, A. Reiners, S. Dreizler, and T. J. Henry, “The CRIRES Search for Planets Around the Lowest-mass Stars. I. High-precision Near-infrared Radial Velocities with an Ammonia Gas Cell,” , vol. 713, pp. 410–422, Apr. 2010.
- [25] A. J. Metcalf, C. D. Fredrick, R. C. Terrien, S. B. Papp, and S. A. Diddams, “A 30 GHz electro-optic frequency comb spanning 300 THz in the near infrared and visible,” *arXiv e-prints*, Feb. 2019.

- [26] A. J. Metcalf, T. Anderson, C. F. Bender, S. Blakeslee, W. Brand, D. R. Carlson, W. D. Cochran, S. A. Diddams, M. Endl, C. Fredrick, S. Halverson, D. D. Hickstein, F. Hearty, J. Jennings, S. Kanodia, K. F. Kaplan, E. Levi, E. Lubar, S. Mahadevan, A. Monson, J. P. Ninan, C. Nitroy, S. Osterman, S. B. Papp, F. Quinlan, L. Ramsey, P. Robertson, A. Roy, C. Schwab, S. Sigurdsson, K. Srinivasan, G. Stefansson, D. A. Sterner, R. Terrien, A. Wolszczan, J. T. Wright, and G. Ycas, “Stellar Spectroscopy in the Near-infrared with a Laser Frequency Comb,” *arXiv e-prints*, Feb. 2019.
- [27] A. Reiners, M. Zechmeister, J. A. Caballero, I. Ribas, J. C. Morales, S. V. Jeffers, P. Schöfer, L. Tal-Or, A. Quirrenbach, P. J. Amado, A. Kaminski, W. Seifert, M. Abril, J. Aceituno, F. J. Alonso-Floriano, M. Ammler-von Eiff, R. Antona, G. Anglada-Escudé, H. Anwand-Heerwart, B. Arroyo-Torres, M. Azzaro, D. Baroch, D. Barrado, F. F. Bauer, S. Becerril, V. J. S. Béjar, D. Benítez, Z. M. Berdinas, G. Bergond, M. Blümcke, M. Brinkmüller, C. del Burgo, J. Cano, M. C. Cárdenas Vázquez, E. Casal, C. Cifuentes, A. Claret, J. Colomé, M. Cortés-Contreras, S. Czesla, E. Díez-Alonso, S. Dreizler, C. Feiz, M. Fernández, I. M. Ferro, B. Fuhrmeister, D. Galadí-Enríquez, A. Garcia-Piquer, M. L. García Vargas, L. Gesa, V. Gómez Galera, J. I. González Hernández, R. González-Peinado, U. Grözing, S. Grohner, J. Guàrdia, E. W. Guenther, A. Guijarro, E. de Guindos, J. Gutiérrez-Soto, H. J. Hagen, A. P. Hatzes, P. H. Hauschildt, R. P. Hedrosa, J. Helmling, T. Henning, I. Hermelo, R. Hernández Arabí, L. Hernández Castaño, F. Hernández Hernando, E. Herrero, A. Huber, P. Huke, E. N. Johnson, E. de Juan, M. Kim, R. Klein, J. Klüter, A. Klutsch, M. Kürster, M. Lafarga, A. Lamert, M. Lampón, L. M. Lara, W. Laun, U. Lemke, R. Lenzen, R. Launhardt, M. López del Fresno, J. López-González, M. López-Puertas, J. F. López Salas, J. López-Santiago, R. Luque, H. Magán Madinabeitia, U. Mall, L. Mancini, H. Mandel, E. Marfil, J. A. Marín Molina, D. Maroto Fernández, E. L. Martín, S. Martín-Ruiz, C. J. Marvin, R. J. Mathar, E. Mirabet,

- D. Montes, M. E. Moreno-Raya, A. Moya, R. Mundt, E. Nagel, V. Naranjo, L. Nortmann, G. Nowak, A. Ofir, R. Oreiro, E. Pallé, J. Panduro, J. Pascual, V. M. Passegger, A. Pavlov, S. Pedraz, A. Pérez-Calpena, D. Pérez Medialdea, M. Perger, M. A. C. Perryman, M. Pluto, O. Rabaza, A. Ramón, R. Rebolo, P. Redondo, S. Reffert, S. Reinhardt, P. Rhode, H. W. Rix, F. Rodler, E. Rodríguez, C. Rodríguez-López, A. Rodríguez Trinidad, R. R. Rohloff, A. Rosich, S. Sadegi, E. Sánchez-Blanco, M. A. Sánchez Carrasco, A. Sánchez-López, J. Sanz-Forcada, P. Sarkis, L. F. Sarmiento, S. Schäfer, J. H. M. M. Schmitt, J. Schiller, A. Schweitzer, E. Solano, O. Stahl, J. B. P. Strachan, J. Stürmer, J. C. Suárez, H. M. Tabernero, M. Tala, T. Trifonov, S. M. Tulloch, R. G. Ulbrich, G. Veredas, J. I. Vico Linares, F. Vilardell, K. Wagner, J. Winkler, V. Wothoff, W. Xu, F. Yan, and M. R. Zapatero Osorio, “The CARMENES search for exoplanets around M dwarfs. High-resolution optical and near-infrared spectroscopy of 324 survey stars,” , vol. 612, p. A49, Apr 2018.
- [28] A. Seifahrt, H. U. Käufel, G. Zängl, J. L. Bean, M. J. Richter, and R. Siebenmorgen, “Synthesising, using, and correcting for telluric features in high-resolution astronomical spectra . A near-infrared case study using CRIRES,” , vol. 524, p. A11, Dec 2010.
- [29] T. Feger, “Searching for extrasolar planets with single-mode spectrographs,” Ph.D. dissertation, Sydney, Australia, 2016.
- [30] G. Anglada-Escudé, P. Plavchan, S. Mills, P. Gao, E. García-Berríos, N. S. Lewis, K. Sung, D. Ciardi, C. Beichman, C. Brinkworth, J. Johnson, C. Davison, R. White, and L. Prato, “Design and Construction of Absorption Cells for Precision Radial Velocities in the K Band Using Methane Isotopologues,” , vol. 124, p. 586, Jun. 2012.
- [31] P. P. Plavchan, G. Anglada-Escudé, R. White, P. Gao, C. Davison, S. Mills, C. Beichman, C. Brinkworth, J. Johnson, M. Bottom, D. Ciardi, K. Wallace, B. Mennesson, K. von Braun, G. Vasisht, L. Prato, S. Kane, A. Tanner, B. Walp, S. Crawford, and S. Lin, “Precision near-infrared radial velocity instrumentation I: absorption gas



- cells,” in *Techniques and Instrumentation for Detection of Exoplanets VI*, ser. , vol. 8864, Sep. 2013, p. 88641J.
- [32] J. T. Wright and J. D. Eastman, “Barycentric Corrections at  $1 \text{ cm s}^{-1}$  for Precise Doppler Velocities,” , vol. 126, p. 838, Sep. 2014.
- [33] R. Tronsgaard, L. Buchave, J. Wright, J. Eastman, and R. Blackman, “Photon-weighted barycentric correction and its importance for precise radial velocities,” , Aug 2019.
- [34] H. Sameshima, N. Matsunaga, N. Kobayashi, H. Kawakita, S. Hamano, Y. Ikeda, S. Kondo, K. Fukue, D. Taniguchi, M. Mizumoto, A. Arai, S. Otsubo, K. Takenaka, A. Watase, A. Asano, C. Yasui, N. Izumi, and T. Yoshikawa, “Correction of Near-infrared High-resolution Spectra for Telluric Absorption at  $0.90\text{-}1.35 \mu\text{m}$ ,” , vol. 130, no. 989, p. 074502, Jul 2018.
- [35] J. Choi, G. Marcy, and A. Howard, “A Doppler Search for Planets around Barnard’s Star,” in *American Astronomical Society Meeting Abstracts #219*, ser. American Astronomical Society Meeting Abstracts, vol. 219, Jan. 2012, p. 245.04.
- [36] I. Ribas, M. Tuomi, A. Reiners, R. P. Butler, J. C. Morales, M. Perger, S. Dreizler, C. Rodríguez-López, J. I. González Hernández, A. Rosich, F. Feng, T. Trifonov, S. S. Vogt, J. A. Caballero, A. Hatzes, E. Herrero, S. V. Jeffers, M. Lafarga, F. Murgas, R. P. Nelson, E. Rodríguez, J. B. P. Strachan, L. Tal-Or, J. Teske, B. Toledo-Padrón, M. Zechmeister, A. Quirrenbach, P. J. Amado, M. Azzaro, V. J. S. Béjar, J. R. Barnes, Z. M. Berdiñas, J. Burt, G. Coleman, M. Cortés-Contreras, J. Crane, S. G. Engle, E. F. Guinan, C. A. Haswell, T. Henning, B. Holden, J. Jenkins, H. R. A. Jones, A. Kaminski, M. Kiraga, M. Kürster, M. H. Lee, M. J. López-González, D. Montes, J. Morin, A. Ofir, E. Pallé, R. Rebolo, S. Reffert, A. Schweitzer, W. Seifert, S. A. Shectman, D. Staab, R. A. Street, A. Suárez Mascareño, Y. Tsapras, S. X. Wang,

- and G. Anglada-Escudé, “A candidate super-Earth planet orbiting near the snow line of Barnard’s star,” , vol. 563, pp. 365–368, Nov 2018.
- [37] A. W. Howard, G. W. Marcy, D. A. Fischer, H. Isaacson, P. S. Muirhead, G. W. Henry, T. S. Boyajian, K. von Braun, J. C. Becker, J. T. Wright, and J. A. Johnson, “The NASA-UC-UH ETA-Earth Program. IV. A Low-mass Planet Orbiting an M Dwarf 3.6 PC from Earth,” , vol. 794, p. 51, Oct. 2014.
- [38] J. S. Jenkins, L. W. Ramsey, H. R. A. Jones, Y. Pavlenko, J. Gallardo, J. R. Barnes, and D. J. Pinfield, “Rotational Velocities for M Dwarfs,” , vol. 704, pp. 975–988, Oct. 2009.
- [39] G. T. van Belle and K. von Braun, “Directly Determined Linear Radii and Effective Temperatures of Exoplanet Host Stars,” , vol. 694, pp. 1085–1098, Apr. 2009.
- [40] K. Horne, “An optimal extraction algorithm for CCD spectroscopy,” , vol. 98, pp. 609–617, Jun. 1986.
- [41] R. P. Butler, G. W. Marcy, E. Williams, C. McCarthy, P. Dosanji, and S. S. Vogt, “Attaining Doppler Precision of 3 M s<sup>-1</sup>,” , vol. 108, p. 500, Jun. 1996.
- [42] Z. Bajzer and I. Penzar, “simps,” 1999. [Online]. Available: <https://www.mathworks.com/matlabcentral/fileexchange/102-simps>
- [43] J. L. Bertaux, R. Lallement, S. Ferron, C. Boonne, and R. Bodichon, “TAPAS, a web-based service of atmospheric transmission computation for astronomy,” , vol. 564, p. A46, Apr. 2014.
- [44] H. F. Arfken G., Weber H., *Mathematical Methods for Physicists*. Academic press, 2012.
- [45] B. Cale, P. Plavchan, D. LeBrun, J. Gagné, P. Gao, A. Tanner, C. Beichman, S. Xuesong Wang, E. Gaidos, J. Teske, D. Ciardi, G. Vasisht, S. R. Kane, and K. von

- Braun, “Precise Radial Velocities of Cool Low-mass Stars with iSHELL,” , vol. 158, no. 5, p. 170, Nov. 2019.
- [46] T. D. Lipson S.G., Lipson H., *Optical Physics*. Cambridge, 1995.
- [47] C. H. Blake, D. Charbonneau, and R. J. White, “The NIRSPEC Ultracool Dwarf Radial Velocity Survey,” , vol. 723, pp. 684–706, Nov. 2010.
- [48] C. J. Crockett, N. I. Mahmud, L. Prato, C. M. Johns-Krull, D. T. Jaffe, and C. A. Beichman, “Precision Radial Velocities with CSHELL,” , vol. 735, p. 78, Jul. 2011.
- [49] I. Bailey, John I., R. J. White, C. H. Blake, D. Charbonneau, T. S. Barman, A. M. Tanner, and G. Torres, “Precise Infrared Radial Velocities from Keck/NIRSPEC and the Search for Young Planets,” , vol. 749, no. 1, p. 16, Apr. 2012.
- [50] F. Allard, T. Guillot, H.-G. Ludwig, P. H. Hauschildt, A. Schweitzer, D. R. Alexander, and J. W. Ferguson, “Model Atmospheres and Spectra: The Role of Dust,” in *Brown Dwarfs*, ser. IAU Symposium, E. Martín, Ed., vol. 211, Jun. 2003, p. 325.
- [51] F. Allard, D. Homeier, and B. Freytag, “Model Atmospheres From Very Low Mass Stars to Brown Dwarfs,” in *16th Cambridge Workshop on Cool Stars, Stellar Systems, and the Sun*, ser. Astronomical Society of the Pacific Conference Series, C. Johns-Krull, M. K. Browning, and A. A. West, Eds., vol. 448, Dec. 2011, p. 91.
- [52] B. Sato, E. Kambe, Y. Takeda, H. Izumiura, and H. Ando, “Development of Iodine Cells for the Subaru HDS and the Okayama HIDES: II. New Software for Precise Radial Velocity Measurements,” , vol. 54, pp. 873–882, Dec. 2002.
- [53] G. Kovács, G. Bakos, and R. W. Noyes, “A trend filtering algorithm for wide-field variability surveys,” , vol. 356, no. 2, pp. 557–567, Jan 2005.
- [54] S. Aigrain, H. Parviainen, S. Roberts, S. Reece, and T. Evans, “Robust, open-source removal of systematics in Kepler data,” , vol. 471, no. 1, pp. 759–769, Oct 2017.

- [55] M. Still and T. Barclay, “PyKE: Reduction and analysis of Kepler Simple Aperture Photometry data,” *Astrophysics Source Code Library*, Aug. 2012.
- [56] M. Bedell, D. W. Hogg, D. Foreman-Mackey, B. T. Montet, and R. Luger, “Wobble: a data-driven method for precision radial velocities,” *arXiv e-prints*, p. arXiv:1901.00503, Jan 2019.
- [57] G. Gopalan, P. Plavchan, J. van Eyken, D. Ciardi, K. von Braun, and S. R. Kane, “Application of the Trend Filtering Algorithm for Photometric Time Series Data,” , vol. 128, no. 966, p. 084504, Aug 2016.
- [58] F. Bouchy, F. Pepe, and D. Queloz, “Fundamental photon noise limit to radial velocity measurements,” , vol. 374, pp. 733–739, Aug. 2001.
- [59] R. Andrae, T. Schulze-Hartung, and P. Melchior, “Dos and don’ts of reduced chi-squared,” *arXiv e-prints*, p. arXiv:1012.3754, Dec 2010.
- [60] K. Pearson, “Note on Regression and Inheritance in the Case of Two Parents,” *Proceedings of the Royal Society of London Series I*, vol. 58, pp. 240–242, 1895.
- [61] I. S. McLean, E. E. Becklin, D. F. Figer, S. Larson, T. Liu, and J. Graham, “NIR-SPEC: a near-infrared cross-dispersed echelle spectrograph for the Keck II telescope,” in *Infrared Detectors and Instrumentation for Astronomy*, ser. , A. M. Fowler, Ed., vol. 2475, Jun. 1995, pp. 350–358.
- [62] H.-U. Kaeufl, P. Ballester, P. Biereichel, B. Delabre, R. Donaldson, R. Dorn, E. Fedrigo, G. Finger, G. Fischer, F. Franza, D. Gojak, G. Huster, Y. Jung, J.-L. Lizon, L. Mehrgan, M. Meyer, A. Moorwood, J.-F. Pirard, J. Paufigue, E. Pozna, R. Siebenmorgen, A. Silber, J. Stegmeier, and S. Wegerer, “CRIRES: a high-resolution infrared spectrograph for ESO’s VLT,” in *Ground-based Instrumentation for Astronomy*, ser. , A. F. M. Moorwood and M. Iye, Eds., vol. 5492, Sep. 2004, pp. 1218–1227.
- [63] L. Tal-Or, M. Zechmeister, A. Reiners, S. V. Jeffers, P. Schöfer, A. Quirrenbach, P. J.

- Amado, I. Ribas, J. A. Caballero, J. Aceituno, F. F. Bauer, V. J. S. Béjar, S. Czesla, S. Dreizler, B. Fuhrmeister, A. P. Hatzes, E. N. Johnson, M. Kürster, M. Lafarga, D. Montes, J. C. Morales, S. Reffert, S. Sadegi, W. Seifert, and D. Shulyak, “The CARMENES search for exoplanets around M dwarfs. Radial-velocity variations of active stars in visual-channel spectra,” , vol. 614, p. A122, Jun. 2018.
- [64] T. Barclay, J. Pepper, and E. V. Quintana, “A Revised Exoplanet Yield from the Transiting Exoplanet Survey Satellite (TESS),” , vol. 239, p. 2, Nov. 2018.
- [65] N. E. Batalha, T. Lewis, J. J. Fortney, N. M. Batalha, E. Kempton, N. K. Lewis, and M. R. Line, “The Precision of Mass Measurements Required for Robust Atmospheric Characterization of Transiting Exoplanets,” , vol. 885, no. 1, p. L25, Nov. 2019.
- [66] M. Desort, A. M. Lagrange, F. Galland, S. Udry, and M. Mayor, “Search for exoplanets with the radial-velocity technique: quantitative diagnostics of stellar activity,” , vol. 473, no. 3, pp. 983–993, Oct. 2007.
- [67] N. Meunier and A. M. Lagrange, “Using the Sun to estimate Earth-like planets detection capabilities. IV. Correcting for the convective component,” , vol. 551, p. A101, Mar. 2013.
- [68] X. Dumusque, I. Boisse, and N. C. Santos, “SOAP 2.0: A Tool to Estimate the Photometric and Radial Velocity Variations Induced by Stellar Spots and Plages,” , vol. 796, no. 2, p. 132, Dec. 2014.
- [69] X. Dumusque, “Measuring precise radial velocities on individual spectral lines. I. Validation of the method and application to mitigate stellar activity,” , vol. 620, p. A47, Nov. 2018.
- [70] A. W. Wise, S. E. Dodson-Robinson, K. Bevenour, and A. Provini, “New Methods for Finding Activity-sensitive Spectral Lines: Combined Visual Identification and an Automated Pipeline Find a Set of 40 Activity Indicators,” , vol. 156, no. 4, p. 180, Oct. 2018.

- [71] M. Cretignier, X. Dumusque, R. Allart, F. Pepe, and C. Lovis, “Measuring precise radial velocities on individual spectral lines. II. Dependence of stellar activity signal on line depth,” , vol. 633, p. A76, Jan. 2020.
- [72] R. D. Haywood, A. Collier Cameron, D. Queloz, S. C. C. Barros, M. Deleuil, R. Fares, M. Gillon, A. F. Lanza, C. Lovis, C. Moutou, F. Pepe, D. Pollacco, A. Santerne, D. Ségransan, and Y. C. Unruh, “Planets and stellar activity: hide and seek in the CoRoT-7 system,” , vol. 443, pp. 2517–2531, Sep. 2014.
- [73] S. K. Grunblatt, A. W. Howard, and R. D. Haywood, “Determining the Mass of Kepler-78b with Nonparametric Gaussian Process Estimation,” , vol. 808, no. 2, p. 127, Aug. 2015.
- [74] M. López-Morales, R. D. Haywood, J. L. Coughlin, L. Zeng, L. A. Buchhave, H. A. C. Giles, L. Affer, A. S. Bonomo, D. Charbonneau, A. Collier Cameron, R. Consentino, C. D. Dressing, X. Dumusque, P. Figueira, A. F. M. Fiorenzano, A. Harutyunyan, J. A. Johnson, D. W. Latham, E. D. Lopez, C. Lovis, L. Malavolta, M. Mayor, G. Micela, E. Molinari, A. Mortier, F. Motalebi, V. Nascimbeni, F. Pepe, D. F. Phillips, G. Piotto, D. Pollacco, D. Queloz, K. Rice, D. Sasselov, D. Segransan, A. Sozzetti, S. Udry, A. Vanderburg, and C. Watson, “Kepler-21b: A Rocky Planet Around a  $V = 8.25$  Magnitude Star,” , vol. 152, no. 6, p. 204, Dec. 2016.
- [75] B. Toledo-Adornier, A. Suárez Mascareño, J. I. González Hernández, R. Rebolo, M. Pinamonti, M. Perger, G. Scandariato, M. Damasso, A. Sozzetti, J. Maldonado, S. Desidera, I. Ribas, G. Micela, L. Affer, E. González-Alvarez, G. Leto, I. Pagano, R. Zanarín Sánchez, P. Giacobbe, E. Herrero, J. C. Morales, P. J. Amado, J. A. Caballero, A. Quirrenbach, A. Reiners, and M. Zechmeister, “A super-Earth on a close-in orbit around the M1V star GJ 740. A HADES and CARMENES collaboration,” *arXiv e-prints*, p. arXiv:2102.09441, Feb. 2021.
- [76] P. Robertson, G. Stefansson, S. Mahadevan, M. Endl, W. D. Cochran, C. Beard,

- C. F. Bender, S. A. Diddams, N. Duong, E. B. Ford, C. Fredrick, S. Halverson, F. Hearty, R. Holcomb, L. Juan, S. Kanodia, J. Lubin, A. J. Metcalf, A. Monson, J. P. Ninan, J. Palafoutas, L. W. Ramsey, A. Roy, C. Schwab, R. C. Terrien, and J. T. Wright, “Persistent starspot signals on m dwarfs: Multiwavelength doppler observations with the habitable-zone planet finder and keck/HIRES,” *The Astrophysical Journal*, vol. 897, no. 2, p. 125, jul 2020. [Online]. Available: <https://doi.org/10.3847/1538-4357/ab989f>
- [77] P. Plavchan, T. Barclay, J. Gagné, P. Gao, B. Cale, W. Matzko, D. Dragomir, S. Quinn, D. Feliz, K. Stassun, I. J. M. Crossfield, D. A. Berardo, D. W. Latham, B. Tieu, G. Anglada-Escudé, G. Ricker, R. Vanderspek, S. Seager, J. N. Winn, J. M. Jenkins, S. Rinehart, A. Krishnamurthy, S. Dynes, J. Doty, F. Adams, D. A. Afanasev, C. Beichman, M. Bottom, B. P. Bowler, C. Brinkworth, C. J. Brown, A. Cancino, D. R. Ciardi, M. Clampin, J. T. Clark, K. Collins, C. Davison, D. Foreman-Mackey, E. Furlan, E. J. Gaidos, C. Geneser, F. Giddens, E. Gilbert, R. Hall, C. Hellier, T. Henry, J. Horner, A. W. Howard, C. Huang, J. Huber, S. R. Kane, M. Kenworthy, J. Kielkopf, D. Kipping, C. Klenke, E. Kruse, N. Latouf, P. Lowrance, B. Mennesson, M. Mengel, S. M. Mills, T. Morton, N. Narita, E. Newton, A. Nishimoto, J. Okumura, E. Palle, J. Pepper, E. V. Quintana, A. Roberge, V. Roccataliata, J. E. Schlieder, A. Tanner, J. Teske, C. G. Tinney, A. Vanderburg, K. von Braun, B. Walp, J. Wang, S. X. Wang, D. Weigand, R. White, R. A. Wittenmyer, D. J. Wright, A. Youngblood, H. Zhang, and P. Zilberman, “A planet within the debris disk around the pre-main-sequence star AU Microscopii,” , vol. 582, no. 7813, pp. 497–500, Jun. 2020.
- [78] E. E. Mamajek and C. P. M. Bell, “On the age of the  $\beta$  Pictoris moving group,” , vol. 445, no. 3, pp. 2169–2180, Dec. 2014.
- [79] Gaia Collaboration, A. G. A. Brown, A. Vallenari, T. Prusti, J. H. J. de Bruijne, C. Babusiaux, C. A. L. Bailer-Jones, M. Biermann, D. W. Evans, L. Eyer, F. Jansen, C. Jordi, S. A. Klioner, U. Lammers, L. Lindegren, X. Luri, F. Mignard, C. Panem,

D. Pourbaix, S. Randich, P. Sartoretti, H. I. Siddiqui, C. Soubiran, F. van Leeuwen,  
 N. A. Walton, F. Arenou, U. Bastian, M. Cropper, R. Drimmel, D. Katz, M. G.  
 Lattanzi, J. Bakker, C. Cacciari, J. Castañeda, L. Chaoul, N. Cheek, F. De Angeli,  
 C. Fabricius, R. Guerra, B. Holl, E. Masana, R. Messineo, N. Mowlavi, K. Nienar-  
 towicz, P. Panuzzo, J. Portell, M. Riello, G. M. Seabroke, P. Tanga, F. Thévenin,  
 G. Gracia-Abril, G. Comoretto, M. Garcia-Reinaldos, D. Teyssier, M. Altmann,  
 R. Andrae, M. Audard, I. Bellas-Velidis, K. Benson, J. Berthier, R. Blomme,  
 P. Burgess, G. Busso, B. Carry, A. Cellino, G. Clementini, M. Clotet, O. Creevey,  
 M. Davidson, J. De Ridder, L. Delchambre, A. Dell’Oro, C. Ducourant, J. Fernández-  
 Hernández, M. Fouesneau, Y. Frémat, L. Galluccio, M. García-Torres, J. González-  
 Núñez, J. J. González-Vidal, E. Gosset, L. P. Guy, J. L. Halbwachs, N. C. Hambly,  
 D. L. Harrison, J. Hernández, D. Hestroffer, S. T. Hodgkin, A. Hutton, G. Jasiewicz,  
 A. Jean-Antoine-Piccolo, S. Jordan, A. J. Korn, A. Krone-Martins, A. C. Lanzafame,  
 T. Lebzelter, W. Löffler, M. Manteiga, P. M. Marrese, J. M. Martín-Fleitas, A. Moit-  
 inho, A. Mora, K. Muinonen, J. Osinde, E. Pancino, T. Pauwels, J. M. Petit, A. Recio-  
 Blanco, P. J. Richards, L. Rimoldini, A. C. Robin, L. M. Sarro, C. Siopis, M. Smith,  
 A. Sozzetti, M. Süveges, J. Torra, W. van Reeve, U. Abbas, A. Abreu Aramburu,  
 S. Accart, C. Aerts, G. Altavilla, M. A. Álvarez, R. Alvarez, J. Alves, R. I. Anderson,  
 A. H. Andrei, E. Anglada Varela, E. Antiche, T. Antoja, B. Arcay, T. L. Astraat-  
 madja, N. Bach, S. G. Baker, L. Balaguer-Núñez, P. Balm, C. Barache, C. Barata,  
 D. Barbato, F. Barblan, P. S. Barklem, D. Barrado, M. Barros, M. A. Barstow,  
 S. Bartholomé Muñoz, J. L. Bassilana, U. Becciani, M. Bellazzini, A. Berihuete,  
 S. Bertone, L. Bianchi, O. Bienaymé, S. Blanco-Cuaresma, T. Boch, C. Boeche,  
 A. Bombrun, R. Borrachero, D. Bossini, S. Bouquillon, G. Bourda, A. Bragaglia,  
 L. Bramante, M. A. Breddels, A. Bressan, N. Brouillet, T. Brüsemeister, E. Bru-  
 galetta, B. Bucciarelli, A. Burlacu, D. Busonero, A. G. Butkevich, R. Buzzi, E. Caf-  
 fau, R. Cancelliere, G. Cannizzaro, T. Cantat-Gaudin, R. Carballo, T. Carlucci, J. M.  
 Carrasco, L. Casamiquela, M. Castellani, A. Castro-Ginard, P. Charlot, L. Chemin,



A. Chiavassa, G. Coccozza, G. Costigan, S. Cowell, F. Crifo, M. Crosta, C. Crowley, J. Cuypers, C. Dafonte, Y. Damerdj, A. Dapergolas, P. David, M. David, P. de Laverny, F. De Luise, R. De March, D. de Martino, R. de Souza, A. de Torres, J. Debosscher, E. del Pozo, M. Delbo, A. Delgado, H. E. Delgado, P. Di Matteo, S. Diakite, C. Diener, E. Distefano, C. Dolding, P. Drazinos, J. Durán, B. Edvardsson, H. Enke, K. Eriksson, P. Esquej, G. Eynard Bontemps, C. Fabre, M. Fabrizio, S. Faigler, A. J. Falcão, M. Farràs Casas, L. Federici, G. Fedorets, P. Fernique, F. Figueras, F. Filippi, K. Findeisen, A. Fonti, E. Fraile, M. Fraser, B. Frézouls, M. Gai, S. Galleti, D. Garabato, F. García-Sedano, A. Garofalo, N. Garralda, A. Gavel, P. Gavras, J. Gerssen, R. Geyer, P. Giacobbe, G. Gilmore, S. Girona, G. Giuffrida, F. Glass, M. Gomes, M. Granvik, A. Gueguen, A. Guerrier, J. Guiraud, R. Gutiérrez-Sánchez, R. Haigron, D. Hatzidimitriou, M. Hauser, M. Haywood, U. Heiter, A. Helmi, J. Heu, T. Hilger, D. Hobbs, W. Hofmann, G. Holland, H. E. Huckle, A. Hypki, V. Icardi, K. Janßen, G. Jevardat de Fombelle, P. G. Jonker, Á. L. Juhász, F. Julbe, A. Karampelas, A. Kewley, J. Klar, A. Kochoska, R. Kohley, K. Kolenberg, M. Kontizas, E. Kontizas, S. E. Koposov, G. Kordopatis, Z. Kostrzewa-Rutkowska, P. Koubsky, S. Lambert, A. F. Lanza, Y. Lasne, J. B. Lavigne, Y. Le Fustec, C. Le Poncin-Lafitte, Y. Lebreton, S. Leccia, N. Leclerc, I. Lecoeur-Taibi, H. Lenhardt, F. Leroux, S. Liao, E. Licata, H. E. P. Lindstrøm, T. A. Lister, E. Livanou, A. Lobel, M. López, S. Managau, R. G. Mann, G. Mantelet, O. Marchal, J. M. Marchant, M. Marconi, S. Marinoni, G. Marschalkó, D. J. Marshall, M. Martino, G. Marton, N. Mary, D. Massari, G. Matijević, T. Mazeh, P. J. McMillan, S. Messina, D. Michalik, N. R. Millar, D. Molina, R. Molinaro, L. Molnár, P. Montegriffo, R. Mor, R. Morbidelli, T. Morel, D. Morris, A. F. Mulone, T. Muraveva, I. Musella, G. Nelemans, L. Nicastro, L. Noval, W. O'Mullane, C. Ordénovic, D. Ordóñez-Blanco, P. Osborne, C. Pagani, I. Pagano, F. Pailler, H. Palacin, L. Palaversa, A. Panahi, M. Pawlak, A. M. Piersimoni, F. X. Pineau, E. Plachy, G. Plum, E. Poggio, E. Poujoulet, A. Prša, L. Pulone, E. Racero, S. Ragaini, N. Rambaux, M. Ramos-Lerate, S. Regibo, C. Reyly, F. Riclet, V. Ripepi,

A. Riva, A. Rivard, G. Rixon, T. Roegiers, M. Roelens, M. Romero-Gómez, N. Rowell, F. Royer, L. Ruiz-Dern, G. Sadowski, T. Sagristà Sellés, J. Sahlmann, J. Salgado, E. Salguero, N. Sanna, T. Santana-Ros, M. Sarasso, H. Savietto, M. Schultheis, E. Sciacca, M. Segol, J. C. Segovia, D. Ségransan, I. C. Shih, L. Siltala, A. F. Silva, R. L. Smart, K. W. Smith, E. Solano, F. Solitro, R. Sordo, S. Soria Nieto, J. Souchay, A. Spagna, F. Spoto, U. Stampa, I. A. Steele, H. Steidelmüller, C. A. Stephenson, H. Stoev, F. F. Suess, J. Surdej, L. Szabados, E. Szegedi-Elek, D. Tapiador, F. Taris, G. Tauran, M. B. Taylor, R. Teixeira, D. Terrett, P. Teyssandier, W. Thuillot, A. Titarenko, F. Torra Clotet, C. Turon, A. Ulla, E. Utrilla, S. Uzzi, M. Vailant, G. Valentini, V. Valette, A. van Elteren, E. Van Hemelryck, M. van Leeuwen, M. Vaschetto, A. Vecchiato, J. Veljanoski, Y. Viala, D. Vicente, S. Vogt, C. von Essen, H. Voss, V. Votruba, S. Voutsinas, G. Walmsley, M. Weiler, O. Wertz, T. Wevers, L. Wyrzykowski, A. Yoldas, M. Žerjal, H. Ziaepour, J. Zorec, S. Zschocke, S. Zucker, C. Zurbach, and T. Zwitter, “Gaia Data Release 2. Summary of the contents and survey properties,” , vol. 616, p. A1, Aug. 2018.

- [80] M. J. Pecaut and E. E. Mamajek, “Intrinsic Colors, Temperatures, and Bolometric Corrections of Pre-main-sequence Stars,” , vol. 208, no. 1, p. 9, Sep. 2013.
- [81] G. R. Ricker, J. N. Winn, R. Vanderspek, D. W. Latham, G. Á. Bakos, J. L. Bean, Z. K. Berta-Thompson, T. M. Brown, L. Buchhave, N. R. Butler, R. P. Butler, W. J. Chaplin, D. Charbonneau, J. Christensen-Dalsgaard, M. Clampin, D. Deming, J. Doty, N. De Lee, C. Dressing, E. W. Dunham, M. Endl, F. Fressin, J. Ge, T. Henning, M. J. Holman, A. W. Howard, S. Ida, J. M. Jenkins, G. Jernigan, J. A. Johnson, L. Kaltenegger, N. Kawai, H. Kjeldsen, G. Laughlin, A. M. Levine, D. Lin, J. J. Lissauer, P. MacQueen, G. Marcy, P. R. McCullough, T. D. Morton, N. Narita, M. Paegert, E. Palles, F. Pepe, J. Pepper, A. Quirrenbach, S. A. Rinehart, D. Sasselov, B. Sato, S. Seager, A. Sozzetti, K. G. Stassun, P. Sullivan, A. Szentgyorgyi, G. Torres, S. Udry, and J. Villaseñor, “Transiting Exoplanet Survey Satellite (TESS),” *Journal*

*of Astronomical Telescopes, Instruments, and Systems*, vol. 1, p. 014003, Jan. 2015.

- [82] R. A. Wittenmyer, J. Horner, B. D. Carter, S. R. Kane, P. Plavchan, D. Ciardi, and t. MINERVA-Australis consortium, “Understanding Super-Earths with MINERVA-Australis at USQ’s Mount Kent Observatory,” *arXiv e-prints*, p. arXiv:1806.09282, Jun. 2018.
- [83] B. Addison, D. J. Wright, R. A. Wittenmyer, J. Horner, M. W. Mengel, D. Johns, C. Marti, B. Nicholson, J. Soutter, B. Bowler, I. Crossfield, S. R. Kane, J. Kielkopf, P. Plavchan, C. G. Tinney, H. Zhang, J. T. Clark, M. Clerte, J. D. Eastman, J. Swift, M. Bottom, P. Muirhead, N. McCrady, E. Herzig, K. Hogstrom, M. Wilson, D. Sliski, S. A. Johnson, J. T. Wright, J. A. Johnson, C. Blake, R. Riddle, B. Lin, M. Cornachione, T. R. Bedding, D. Stello, D. Huber, S. Marsden, and B. D. Carter, “Minerva-Australis. I. Design, Commissioning, and First Photometric Results,” , vol. 131, no. 1005, p. 115003, Nov. 2019.
- [84] B. C. Addison, D. J. Wright, B. A. Nicholson, B. Cale, T. Mocnik, D. Huber, P. Plavchan, R. A. Wittenmyer, A. Vanderburg, W. J. Chaplin, A. Chontos, J. T. Clark, J. D. Eastman, C. Ziegler, R. Brahm, B. D. Carter, M. Clerte, N. Espinoza, J. Horner, J. Bentley, A. Jordán, S. R. Kane, J. F. Kielkopf, E. Laychock, M. W. Mengel, J. Okumura, K. G. Stassun, T. R. Bedding, B. P. Bowler, A. Burnelis, S. Blanco-Cuaresma, M. Collins, I. Crossfield, A. B. Davis, D. Evensberger, A. Heitzmann, S. B. Howell, N. Law, A. W. Mann, S. C. Marsden, R. A. Matson, J. H. O’Connor, A. Shporer, C. Stevens, C. G. Tinney, C. Tylor, S. Wang, H. Zhang, T. Henning, D. Kossakowski, G. Ricker, P. Sarkis, M. Schlecker, P. Torres, R. Vanderspek, D. W. Latham, S. Seager, J. N. Winn, J. M. Jenkins, I. Mireles, P. Rowden, J. Pepper, T. Daylan, J. E. Schlieder, K. A. Collins, K. I. Collins, T.-G. Tan, W. H. Ball, S. Basu, D. L. Buzasi, T. L. Campante, E. Corsaro, L. González-Cuesta, G. R. Davies, L. de Almeida, J. do Nascimento, Jose-Dias, R. A. García, Z. Guo, R. Handberg, S. Hekker, D. R. Hey, T. Kallinger, S. D. Kawaler, C. Kayhan, J. S. Kuzlewicz, M. N. Lund,

- A. Lyttle, S. Mathur, A. Miglio, B. Mosser, M. B. Nielsen, A. M. Serenelli, V. S. Aguirre, and N. Themeßl, “TOI-257b (HD 19916b): a warm sub-saturn orbiting an evolved F-type star,” , vol. 502, no. 3, pp. 3704–3722, Apr. 2021.
- [85] S. I. Barnes, S. Gibson, K. Nield, and D. Cochrane, “KiwiSpec - an advanced spectrograph for high resolution spectroscopy: optical design and variations,” in *Ground-based and Airborne Instrumentation for Astronomy IV*, ser. Society of Photo-Optical Instrumentation Engineers (SPIE) Conference Series, I. S. McLean, S. K. Ramsay, and H. Takami, Eds., vol. 8446, Sep. 2012, p. 844688.
- [86] G. Anglada-Escudé and R. P. Butler, “The HARPS-TERRA Project. I. Description of the Algorithms, Performance, and New Measurements on a Few Remarkable Stars Observed by HARPS,” , vol. 200, no. 2, p. 15, Jun. 2012.
- [87] A. Quirrenbach, P. J. Amado, I. Ribas, A. Reiners, J. A. Caballero, W. Seifert, J. Aceituno, M. Azzaro, D. Baroch, D. Barrado, F. Bauer, S. Becerril, V. J. S. Bèjar, D. Benítez, M. Brinkmøller, C. Cardona Guillén, C. Cifuentes, J. Colomé, M. Cortés-Contreras, S. Czesla, S. Dreizler, K. Frölich, B. Fuhrmeister, D. Galadí-Enríquez, J. I. González Hernández, R. González Peinado, E. W. Guenther, E. de Guindos, H. J. Hagen, A. P. Hatzes, P. H. Hauschildt, J. Helmling, T. Henning, O. Herbort, L. Hernández Castaño, E. Herrero, D. Hintz, S. V. Jeffers, E. N. Johnson, E. de Juan, A. Kaminski, H. Klahr, M. Kürster, M. Lafarga, L. Sairam, M. Lampón, L. M. Lara, R. Launhardt, M. López del Fresno, M. López-Puertas, R. Luque, H. Mandel, E. G. Marfil, E. L. Martín, S. Martín-Ruiz, R. J. Mathar, D. Montes, J. C. Morales, E. Nagel, L. Nortmann, G. Nowak, E. Pallé, V. M. Passegger, A. Pavlov, S. Pedraz, D. Pérez-Medialdea, M. Perger, R. Rebolo, S. Reffert, E. Rodríguez, C. Rodríguez López, A. Rosich, S. Sabotta, S. Sadegi, M. Salz, A. Sánchez-López, J. Sanz-Forcada, P. Sarkis, S. Schäfer, J. Schiller, J. H. M. M. Schmitt, P. Schöfer, A. Schweitzer, D. Shulyak, E. Solano, O. Stahl, M. Tala Pinto, T. Trifonov, M. R. Zapatero Osorio, F. Yan, M. Zechmeister, F. J. Abellán, M. Abril, F. J. Alonso-Floriano,

M. Ammler-von Eiff, G. Anglada-Escudé, H. Anwand-Heerwart, B. Arroyo-Torres, Z. M. Berdiñas, G. Bergondy, M. Blümcke, C. del Burgo, J. Cano, J. Carro, M. C. Cárdenas, E. Casal, A. Claret, E. Díez-Alonso, M. Doellinger, R. Dorda, C. Feiz, M. Fernández, I. M. Ferro, G. Gaisné, I. Gallardo, M. C. Gálvez-Ortiz, A. García-Piquer, M. L. García-Vargas, R. Garrido, L. Gesa, V. Gómez Galera, E. González-Álvarez, L. González-Cuesta, S. Grohnert, U. Grözing, J. Guàrdia, A. Guijarro, R. P. Hedrosa, D. Hermann, I. Hermelo, R. Hernández Arabí, F. Hernández Hernández, D. Hidalgo, G. Holgado, A. Huber, K. Huber, P. Huke, M. Kehr, M. Kim, R. Klein, J. Klüter, A. Klutsch, F. Labarga, N. Labiche, A. Lamert, W. Laun, F. J. Lázaro, U. Lemke, R. Lenzen, M. Llamas, J. L. Lizon, N. Lodieu, M. J. López González, M. López-Morales, J. F. López Salas, J. López-Santiago, H. Magán Madinabeitia, U. Mall, L. Mancini, J. A. Marín Molina, H. Martínez-Rodríguez, D. Maroto Fernández, C. J. Marvin, E. Mirabet, M. E. Moreno-Raya, A. Moya, R. Mundt, V. Naranjo, J. Panduro, J. Pascual, A. Pérez-Calpena, M. A. C. Perryman, M. Pluto, A. Ramón, P. Redondo, S. Reinhart, P. Rhode, H. W. Rix, F. Rodler, R. R. Rohloff, E. Sánchez-Blanco, M. A. Sánchez Carrasco, L. F. Sarmiento, C. Schmidt, C. Storz, J. B. P. Strachan, J. Stürmer, J. C. Suárez, H. M. Tabernero, L. Tal-Or, S. M. Tulloch, R. G. Ulbrich, G. Veredas, J. L. Vico Linares, M. Vidal-Dasilva, F. Vilardell, K. Wagner, J. Winkler, V. Wolthoff, W. Xu, and Z. Zhao, “CARMENES: high-resolution spectra and precise radial velocities in the red and infrared,” in *Ground-based and Airborne Instrumentation for Astronomy VII*, ser. Society of Photo-Optical Instrumentation Engineers (SPIE) Conference Series, C. J. Evans, L. Simard, and H. Takami, Eds., vol. 10702, Jul. 2018, p. 107020W.

- [88] J. A. Caballero, J. Guàrdia, M. López del Fresno, M. Zechmeister, E. de Juan, F. J. Alonso-Floriano, P. J. Amado, J. Colomé, M. Cortés-Contreras, Á. García-Piquer, L. Gesa, E. de Guindos, H. J. Hagen, J. Helmling, L. Hernández Castaño, M. Kürster, J. López-Santiago, D. Montes, R. Morales Muñoz, A. Pavlov, A. Quirrenbach, A. Reiners, I. Ribas, W. Seifert, and E. Solano, “CARMENES: data flow,” in *Observatory*

*Operations: Strategies, Processes, and Systems VI*, ser. Society of Photo-Optical Instrumentation Engineers (SPIE) Conference Series, A. B. Peck, R. L. Seaman, and C. R. Benn, Eds., vol. 9910, Jul. 2016, p. 99100E.

- [89] M. Zechmeister, A. Reiners, P. J. Amado, M. Azzaro, F. F. Bauer, V. J. S. Béjar, J. A. Caballero, E. W. Guenther, H. J. Hagen, S. V. Jeffers, A. Kaminski, M. Kürster, R. Launhardt, D. Montes, J. C. Morales, A. Quirrenbach, S. Reffert, I. Ribas, W. Seifert, L. Tal-Or, and V. Wolthoff, “Spectrum radial velocity analyser (SERVAL). High-precision radial velocities and two alternative spectral indicators,” , vol. 609, p. A12, Jan. 2018.
- [90] T. Trifonov, M. Kürster, M. Zechmeister, L. Tal-Or, J. A. Caballero, A. Quirrenbach, P. J. Amado, I. Ribas, A. Reiners, S. Reffert, S. Dreizler, A. P. Hatzes, A. Kaminski, R. Launhardt, T. Henning, D. Montes, V. J. S. Béjar, R. Mundt, A. Pavlov, J. H. M. M. Schmitt, W. Seifert, J. C. Morales, G. Nowak, S. V. Jeffers, C. Rodríguez-López, C. del Burgo, G. Anglada-Escudé, J. López-Santiago, R. J. Mathar, M. Ammler-von Eiff, E. W. Guenther, D. Barrado, J. I. González Hernández, L. Mancini, J. Stürmer, M. Abril, J. Aceituno, F. J. Alonso-Floriano, R. Antona, H. Anwand-Heerwart, B. Arroyo-Torres, M. Azzaro, D. Baroch, F. F. Bauer, S. Becerril, D. Benítez, Z. M. Berdiñas, G. Bergond, M. Blümcke, M. Brinkmüller, J. Cano, M. C. Cárdenas Vázquez, E. Casal, C. Cifuentes, A. Claret, J. Colomé, M. Cortés-Contreras, S. Czesla, E. Díez-Alonso, C. Feiz, M. Fernández, I. M. Ferro, B. Fuhrmeister, D. Galadí-Enríquez, A. Garcia-Piquer, M. L. García Vargas, L. Gesa, V. Gómez Galera, R. González-Peinado, U. Grözing, S. Grohnert, J. Guàrdia, A. Guijarro, E. de Guindos, J. Gutiérrez-Soto, H. J. Hagen, P. H. Hauschildt, R. P. Hedrosa, J. Helmling, I. Hermelo, R. Hernández Arabí, L. Hernández Castaño, F. Hernández Hernando, E. Herrero, A. Huber, P. Huke, E. Johnson, E. de Juan, M. Kim, R. Klein, J. Klüter, A. Klutsch, M. Lafarga, M. Lampón, L. M. Lara, W. Laun, U. Lemke, R. Lenzen, M. López del Fresno, M. J. López-González, M. López-Puertas, J. F. López

Salas, R. Luque, H. Magán Madinabeitia, U. Mall, H. Mandel, E. Marfil, J. A. Marín Molina, D. Maroto Fernández, E. L. Martín, S. Martín-Ruiz, C. J. Marvin, E. Mirabet, A. Moya, M. E. Moreno-Raya, E. Nagel, V. Naranjo, L. Nortmann, A. Ofir, R. Oreiro, E. Pallé, J. Panduro, J. Pascual, V. M. Passegger, S. Pedraz, A. Pérez-Calpena, D. Pérez Medialdea, M. Perger, M. A. C. Perryman, M. Pluto, O. Rabaza, A. Ramón, R. Rebolo, P. Redondo, S. Reinhardt, P. Rhode, H. W. Rix, F. Rodler, E. Rodríguez, A. Rodríguez Trinidad, R. R. Rohloff, A. Rosich, S. Sadegi, E. Sánchez-Blanco, M. A. Sánchez Carrasco, A. Sánchez-López, J. Sanz-Forcada, P. Sarkis, L. F. Sarmiento, S. Schäfer, J. Schiller, P. Schöfer, A. Schweitzer, E. Solano, O. Stahl, J. B. P. Strachan, J. C. Suárez, H. M. Tabernero, M. Tala, S. M. Tulloch, G. Veredas, J. I. Vico Linares, F. Vilardell, K. Wagner, J. Winkler, V. Wolthoff, W. Xu, F. Yan, and M. R. Zapatero Osorio, “The CARMENES search for exoplanets around M dwarfs . First visual-channel radial-velocity measurements and orbital parameter updates of seven M-dwarf planetary systems,” , vol. 609, p. A117, Feb. 2018.

- [91] T. Kotani, M. Tamura, J. Nishikawa, A. Ueda, M. Kuzuhara, M. Omiya, J. Hashimoto, M. Ishizuka, T. Hirano, H. Suto, T. Kurokawa, T. Kokubo, T. Mori, Y. Tanaka, K. Kashiwagi, M. Konishi, T. Kudo, B. Sato, S. Jacobson, K. W. Hodapp, D. B. Hall, W. Aoki, T. Usuda, S. Nishiyama, T. Nakajima, Y. Ikeda, T. Yamamuro, J.-I. Morino, H. Baba, K. Hosokawa, H. Ishikawa, N. Narita, E. Kokubo, Y. Hayano, H. Izumiura, E. Kambe, N. Kusakabe, J. Kwon, M. Ikoma, Y. Hori, H. Genda, A. Fukui, Y. Fujii, H. Kawahara, G. Olivier, N. Jovanovic, H. Harakawa, M. Hayashi, M. Hidai, M. Machida, T. Matsuo, T. Nagata, M. Ogihara, H. Takami, N. Takato, H. Terada, and D. Oh, “The infrared Doppler (IRD) instrument for the Subaru telescope: instrument description and commissioning results,” in *Ground-based and Airborne Instrumentation for Astronomy VII*, ser. , vol. 10702, Jul 2018, p. 1070211.

- [92] T. Hirano, V. Krishnamurthy, E. Gaidos, H. Flewelling, A. W. Mann, N. Narita,

- P. Plavchan, T. Kotani, M. Tamura, H. Harakawa, K. Hodapp, M. Ishizuka, S. Jacobson, M. Konishi, T. Kudo, T. Kurokawa, M. Kuzuhara, J. Nishikawa, M. Omiya, T. Serizawa, A. Ueda, and S. Vievard, “Limits on the Spin-Orbit Angle and Atmospheric Escape for the 22 Myr Old Planet AU Mic b,” , vol. 899, no. 1, p. L13, Aug. 2020.
- [93] D. Tody, “IRAF in the Nineties,” in *Astronomical Data Analysis Software and Systems II*, ser. Astronomical Society of the Pacific Conference Series, R. J. Hanisch, R. J. V. Brissenden, and J. Barnes, Eds., vol. 52, Jan. 1993, p. 173.
- [94] T. Hirano, M. Kuzuhara, T. Kotani, M. Omiya, T. Kudo, H. Harakawa, S. Vievard, T. Kurokawa, J. Nishikawa, M. Tamura, K. Hodapp, M. Ishizuka, S. Jacobson, M. Konishi, T. Serizawa, A. Ueda, E. Gaidos, and B. Sato, “Precision radial velocity measurements by the forward-modeling technique in the near-infrared,” , vol. 72, no. 6, p. 93, Dec. 2020.
- [95] S. S. Vogt, S. L. Allen, B. C. Bigelow, L. Bresee, B. Brown, T. Cantrall, A. Conrad, M. Couture, C. Delaney, H. W. Epps, D. Hilyard, D. F. Hilyard, E. Horn, N. Jern, D. Kanto, M. J. Keane, R. I. Kibrick, J. W. Lewis, J. Osborne, G. H. Pardeilhan, T. Pfister, T. Ricketts, L. B. Robinson, R. J. Stover, D. Tucker, J. Ward, and M. Z. Wei, “HIRES: the high-resolution echelle spectrometer on the Keck 10-m Telescope,” in *Instrumentation in Astronomy VIII*, ser. Society of Photo-Optical Instrumentation Engineers (SPIE) Conference Series, D. L. Crawford and E. R. Craine, Eds., vol. 2198, Jun. 1994, p. 362.
- [96] A. W. Howard, J. A. Johnson, G. W. Marcy, D. A. Fischer, J. T. Wright, D. Bernat, G. W. Henry, K. M. G. Peek, H. Isaacson, K. Apps, M. Endl, W. D. Cochran, J. A. Valenti, J. Anderson, and N. E. Piskunov, “The California Planet Survey. I. Four New Giant Exoplanets,” , vol. 721, no. 2, pp. 1467–1481, Oct. 2010.



- [97] A. Szentgyorgyi, “Center for Astrophysics,” May 2002. [Online]. Available: <http://adsabs.harvard.edu/abs/2016SPIE.9908E..84R>
- [98] G. Fűrész, “TRES,” *PhD thesis, University of Szeged, Hungary*, 2008.
- [99] L. A. Buchhave, G. Á. Bakos, J. D. Hartman, G. Torres, G. Kovács, D. W. Latham, R. W. Noyes, G. A. Esquerdo, M. Everett, A. W. Howard, G. W. Marcy, D. A. Fischer, J. A. Johnson, J. Andersen, G. Fűrész, G. Perumpilly, D. D. Sasselov, R. P. Stefanik, B. Béky, J. Lázár, I. Papp, and P. Sári, “HAT-P-16b: A 4  $M_J$  Planet Transiting a Bright Star on an Eccentric Orbit,” , vol. 720, pp. 1118–1125, Sep. 2010.
- [100] S. N. Quinn, R. J. White, D. W. Latham, L. A. Buchhave, G. Torres, R. P. Stefanik, P. Berlind, A. Bieryla, M. C. Calkins, G. A. Esquerdo, G. Fűrész, J. C. Geary, and A. H. Szentgyorgyi, “HD 285507b: An Eccentric Hot Jupiter in the Hyades Open Cluster,” , vol. 787, no. 1, p. 27, May 2014.
- [101] J. Rayner, A. Tokunaga, D. Jaffe, M. Bonnet, G. Ching, M. Connelley, D. Kokubun, C. Lockhart, and E. Warmbier, “iSHELL: a construction, assembly and testing,” in *Ground-based and Airborne Instrumentation for Astronomy VI*, ser. , vol. 9908, Aug. 2016, p. 990884.
- [102] F. Allard, D. Homeier, and B. Freytag, “Models of very-low-mass stars, brown dwarfs and exoplanets,” *Philosophical Transactions of the Royal Society of London Series A*, vol. 370, no. 1968, pp. 2765–2777, Jun. 2012.
- [103] S. Czesla, S. Schröter, C. P. Schneider, K. F. Huber, F. Pfeifer, D. T. Andreasen, and M. Zechmeister, “PyA: Python astronomy-related packages,” p. ascl:1906.010, Jun 2019.
- [104] R. Tronsgaard, L. A. Buchhave, J. T. Wright, J. D. Eastman, and R. T. Blackman, “Photon-weighted barycentric correction and its importance for precise radial velocities,” , vol. 489, no. 2, pp. 2395–2402, Oct. 2019.

- [105] N. E. Piskunov and J. A. Valenti, “New algorithms for reducing cross-dispersed echelle spectra,” , vol. 385, pp. 1095–1106, Apr. 2002.
- [106] D. Swade, S. Fleming, J. M. Jenkins, D. W. Latham, E. Morgan, S. E. Mullally, W. Sparks, and R. Vanderspek, “The TESS science data archive,” in *Observatory Operations: Strategies, Processes, and Systems VII*, ser. Society of Photo-Optical Instrumentation Engineers (SPIE) Conference Series, vol. 10704, Jul. 2018, p. 1070415.
- [107] M. C. Stumpe, J. C. Smith, J. E. Van Cleve, J. D. Twicken, T. S. Barclay, M. N. Fanelli, F. R. Girouard, J. M. Jenkins, J. J. Kolodziejczak, S. D. McCauliff, and R. L. Morris, “Kepler Presearch Data Conditioning I—Architecture and Algorithms for Error Correction in Kepler Light Curves,” , vol. 124, no. 919, p. 985, Sep. 2012.
- [108] M. C. Stumpe, J. C. Smith, J. H. Catanzarite, J. E. Van Cleve, J. M. Jenkins, J. D. Twicken, and F. R. Girouard, “Multiscale Systematic Error Correction via Wavelet-Based Bandsplitting in Kepler Data,” , vol. 126, no. 935, p. 100, Jan. 2014.
- [109] J. C. Smith, M. C. Stumpe, J. E. Van Cleve, J. M. Jenkins, T. S. Barclay, M. N. Fanelli, F. R. Girouard, J. J. Kolodziejczak, S. D. McCauliff, R. L. Morris, and J. D. Twicken, “Kepler Presearch Data Conditioning II - A Bayesian Approach to Systematic Error Correction,” , vol. 124, no. 919, p. 1000, Sep. 2012.
- [110] T. Trifonov, M. Kürster, M. Zechmeister, L. Tal-Or, J. A. Caballero, A. Quirrenbach, P. J. Amado, I. Ribas, A. Reiners, S. Reffert, S. Dreizler, A. P. Hatzes, A. Kaminski, R. Launhardt, T. Henning, D. Montes, V. J. S. Béjar, R. Mundt, A. Pavlov, J. H. M. M. Schmitt, W. Seifert, J. C. Morales, G. Nowak, S. V. Jeffers, C. Rodríguez-López, C. del Burgo, G. Anglada-Escudé, J. López-Santiago, R. J. Mathar, M. Ammler-von Eiff, E. W. Guenther, D. Barrado, J. I. González Hernández, L. Mancini, J. Stürmer, M. Abril, J. Aceituno, F. J. Alonso-Floriano, R. Antona, H. Anwand-Heerwart, B. Arroyo-Torres, M. Azzaro, D. Baroch, F. F. Bauer, S. Becerril, D. Benítez, Z. M. Berdiñas, G. Bergond, M. Blümcke, M. Brinkmöller, J. Cano,

M. C. Cárdenas Vázquez, E. Casal, C. Cifuentes, A. Claret, J. Colomé, M. Cortés-Contreras, S. Czesla, E. Díez-Alonso, C. Feiz, M. Fernández, I. M. Ferro, B. Fuhrmeister, D. Galadí-Enríquez, A. Garcia-Piquer, M. L. García Vargas, L. Gesa, V. Gómez Galera, R. González-Peinado, U. Grözing, S. Grohnert, J. Guàrdia, A. Guijarro, E. de Guindos, J. Gutiérrez-Soto, H. J. Hagen, P. H. Hauschildt, R. P. Hedrosa, J. Helmling, I. Hermelo, R. Hernández Arabí, L. Hernández Castaño, F. Hernández Hernando, E. Herrero, A. Huber, P. Huke, E. Johnson, E. de Juan, M. Kim, R. Klein, J. Klüter, A. Klutsch, M. Lafarga, M. Lampón, L. M. Lara, W. Laun, U. Lemke, R. Lenzen, M. López del Fresno, M. J. López-González, M. López-Puertas, J. F. López Salas, R. Luque, H. Magán Madinabeitia, U. Mall, H. Mandel, E. Marfil, J. A. Marín Molina, D. Maroto Fernández, E. L. Martín, S. Martín-Ruiz, C. J. Marvin, E. Mirabet, A. Moya, M. E. Moreno-Raya, E. Nagel, V. Naranjo, L. Nortmann, A. Ofir, R. Oreiro, E. Pallé, J. Panduro, J. Pascual, V. M. Passegger, S. Pedraz, A. Pérez-Calpena, D. Pérez Medialdea, M. Perger, M. A. C. Perryman, M. Pluto, O. Rabaza, A. Ramón, R. Rebolo, P. Redondo, S. Reinhardt, P. Rhode, H. W. Rix, F. Rodler, E. Rodríguez, A. Rodríguez Trinidad, R. R. Rohloff, A. Rosich, S. Sadegi, E. Sánchez-Blanco, M. A. Sánchez Carrasco, A. Sánchez-López, J. Sanz-Forcada, P. Sarkis, L. F. Sarmiento, S. Schäfer, J. Schiller, P. Schöfer, A. Schweitzer, E. Solano, O. Stahl, J. B. P. Strachan, J. C. Suárez, H. M. Tabernero, M. Tala, S. M. Tulloch, G. Veredas, J. I. Vico Linares, F. Vilardell, K. Wagner, J. Winkler, V. Wolthoff, W. Xu, F. Yan, and M. R. Zapatero Osorio, “The CARMENES search for exoplanets around M dwarfs . First visual-channel radial-velocity measurements and orbital parameter updates of seven M-dwarf planetary systems,” , vol. 609, p. A117, Feb. 2018.

- [111] J.-F. Donati, D. Kouach, M. Lacombe, S. Baratchart, R. Doyon, X. Delfosse, É. Artigau, C. Moutou, G. Hébrard, F. Bouchy, J. Bouvier, S. Alencar, L. Saddlemyer, L. Parès, P. Rabou, Y. Micheau, F. Dolon, G. Barrick, O. Hernandez, S. Y. Wang, V. Reshetov, N. Striebig, Z. Challita, A. Carmona, S. Tibault, E. Martioli, P. Figueira,

- I. Boisse, and F. Pepe, *SPIRou: A NIR Spectropolarimeter/High-Precision Velocimeter for the CFHT*, 2018, p. 107.
- [112] G. Lo Curto, T. Beniflah, A. Burrows, E. Emsellem, K. Maguire, L. Pasquini, J. Pritchard, and M. Romaniello, “Availability of Reduction Software for HARPS Data at ESO Headquarters in Garching,” *The Messenger*, vol. 142, pp. 42–42, Dec. 2010.
- [113] M. Mayor, F. Pepe, D. Queloz, F. Bouchy, G. Rupprecht, G. Lo Curto, G. Avila, W. Benz, J. L. Bertaux, X. Bonfils, T. Dall, H. Dekker, B. Delabre, W. Eckert, M. Fleury, A. Gilliotte, D. Gojak, J. C. Guzman, D. Kohler, J. L. Lizon, A. Longinotti, C. Lovis, D. Megevand, L. Pasquini, J. Reyes, J. P. Sivan, D. Sosnowska, R. Soto, S. Udry, A. van Kesteren, L. Weber, and U. Weilenmann, “Setting New Standards with HARPS,” *The Messenger*, vol. 114, pp. 20–24, Dec. 2003.
- [114] N. E. Piskunov and J. A. Valenti, “New algorithms for reducing cross-dispersed echelle spectra,” , vol. 385, pp. 1095–1106, Apr. 2002.
- [115] A. Tokovinin, D. A. Fischer, M. Bonati, M. J. Giguere, P. Moore, C. Schwab, J. F. P. Spronck, and A. Szymkowiak, “CHIRON - A Fiber Fed Spectrometer for Precise Radial Velocities,” , vol. 125, pp. 1336–1347, Nov. 2013.
- [116] I. S. McLean, E. E. Becklin, O. Bendiksen, G. Brims, J. Canfield, D. F. Figer, J. R. Graham, J. Hare, F. Lacayanga, J. E. Larkin, S. B. Larson, N. Levenson, N. Magnone, H. Teplitz, and W. Wong, “Design and development of NIRSPEC: a near-infrared echelle spectrograph for the Keck II telescope,” in *Infrared Astronomical Instrumentation*, ser. Society of Photo-Optical Instrumentation Engineers (SPIE) Conference Series, A. M. Fowler, Ed., vol. 3354, Aug. 1998, pp. 566–578.
- [117] J. Gagné, P. Plavchan, P. Gao, G. Anglada-Escude, E. Furlan, C. Davison, A. Tanner, T. J. Henry, A. R. Riedel, C. Brinkworth, D. Latham, M. Bottom, R. White, S. Mills, C. Beichman, J. A. Johnson, D. R. Ciardi, K. Wallace, B. Mennesson, K. von

- Braun, G. Vasisht, L. Prato, S. R. Kane, E. E. Mamajek, B. Walp, T. J. Crawford, R. Rougeot, C. S. Geneser, and J. Catanzarite, “A High-precision Near-infrared Survey for Radial Velocity Variable Low-mass Stars Using CSHELL and a Methane Gas Cell,” , vol. 822, p. 40, May 2016.
- [118] P. Gao, P. Plavchan, J. Gagné, E. Furlan, M. Bottom, G. Anglada-Escudé, R. White, C. L. Davison, C. Beichman, C. Brinkworth, J. Johnson, D. Ciardi, K. Wallace, B. Mennesson, K. von Braun, G. Vasisht, L. Prato, S. R. Kane, A. Tanner, T. J. Crawford, D. Latham, R. Rougeot, C. S. Geneser, and J. Catanzarite, “Retrieval of Precise Radial Velocities from Near-infrared High-resolution Spectra of Low-mass Stars,” , vol. 128, no. 10, p. 104501, Oct. 2016.
- [119] T. P. Greene, A. T. Tokunaga, D. W. Toomey, and J. B. Carr, “CSHELL: a high spectral resolution 1-5 um cryogenic echelle spectrograph for the IRTF,” in *Infrared Detectors and Instrumentation*, ser. Society of Photo-Optical Instrumentation Engineers (SPIE) Conference Series, A. M. Fowler, Ed., vol. 1946, Oct. 1993, pp. 313–324.
- [120] R. D. Haywood, “Hide and seek: Radial-velocity searches for planets around active stars,” Ph.D. dissertation, University of St. Andrews, 2015.
- [121] C. E. Rasmussen and C. K. I. Williams, *Gaussian Processes for Machine Learning*, 2006.
- [122] B. J. Fulton, E. A. Petigura, S. Blunt, and E. Sinukoff, “RadVel: The Radial Velocity Modeling Toolkit,” , vol. 130, no. 4, p. 044504, Apr. 2018.
- [123] S. K. Lam, A. Pitrou, and S. Seibert, “Numba: A llvm-based python jit compiler,” Aug 2015.
- [124] D. Foreman-Mackey, D. W. Hogg, D. Lang, and J. Goodman, “emcee: The MCMC Hammer,” , vol. 125, no. 925, p. 306, Mar. 2013.
- [125] S. Aigrain, F. Pont, and S. Zucker, “A simple method to estimate radial velocity

- variations due to stellar activity using photometry,” , vol. 419, no. 4, pp. 3147–3158, Feb. 2012.
- [126] P. Virtanen, R. Gommers, T. E. Oliphant, M. Haberland, T. Reddy, D. Cournapeau, E. Burovski, P. Peterson, W. Weckesser, J. Bright, S. J. van der Walt, M. Brett, J. Wilson, K. J. Millman, N. Mayorov, A. R. J. Nelson, E. Jones, R. Kern, E. Larson, C. J. Carey, Í. Polat, Y. Feng, E. W. Moore, J. VanderPlas, D. Laxalde, J. Perktold, R. Cimrman, I. Henriksen, E. A. Quintero, C. R. Harris, A. M. Archibald, A. H. Ribeiro, F. Pedregosa, P. van Mulbregt, and SciPy 1.0 Contributors, “SciPy 1.0: Fundamental Algorithms for Scientific Computing in Python,” *Nature Methods*, vol. 17, pp. 261–272, 2020.
- [127] H. Jeffreys, “An Invariant Form for the Prior Probability in Estimation Problems,” *Proceedings of the Royal Society of London Series A*, vol. 186, no. 1007, pp. 453–461, Sep. 1946.
- [128] E. Jones, T. Oliphant, P. Peterson *et al.*, “SciPy: Open source scientific tools for Python,” 2001. [Online]. Available: <http://www.scipy.org/>
- [129] H. Akaike, “A New Look at the Statistical Model Identification,” *IEEE Transactions on Automatic Control*, vol. 19, pp. 716–723, Jan 1974.
- [130] K. P. Burnham and D. R. Anderson, *Model Selection and Multimodel Inference*. Springer, 2002.
- [131] M. Zechmeister and M. Kürster, “GLS: Generalized Lomb-Scargle periodogram,” p. ascl:1807.019, Jul. 2018.
- [132] M. Zechmeister, A. Reiners, P. J. Amado, M. Azzaro, F. F. Bauer, V. J. S. Béjar, J. A. Caballero, E. W. Guenther, H.-J. Hagen, S. V. Jeffers, A. Kaminski, M. Kürster, R. Launhardt, D. Montes, J. C. Morales, A. Quirrenbach, S. Reffert, I. Ribas,

- W. Seifert, L. Tal-Or, and V. Wolthoff, “Spectrum radial velocity analyser (SERVAL). High-precision radial velocities and two alternative spectral indicators,” , vol. 609, p. A12, Jan. 2018.
- [133] V. Rajpaul, S. Aigrain, M. A. Osborne, S. Reece, and S. Roberts, “A Gaussian process framework for modelling stellar activity signals in radial velocity data,” , vol. 452, pp. 2269–2291, Sep. 2015.
- [134] J. Choi, C. McCarthy, G. W. Marcy, A. W. Howard, D. A. Fischer, J. A. Johnson, H. Isaacson, and J. T. Wright, “Precise Doppler Monitoring of Barnard’s Star,” , vol. 764, no. 2, p. 131, Feb. 2013.
- [135] J. D. Hunter, “Matplotlib: A 2d graphics environment,” *Computing in Science Engineering*, vol. 9, no. 3, pp. 90–95, 2007.
- [136] C. R. Harris, K. J. Millman, S. J. van der Walt, R. Gommers, P. Virtanen, D. Cournapeau, E. Wieser, J. Taylor, S. Berg, N. J. Smith, R. Kern, M. Picus, S. Hoyer, M. H. van Kerkwijk, M. Brett, A. Haldane, J. Fernández del Río, M. Wiebe, P. Peterson, P. Gérard-Marchant, K. Sheppard, T. Reddy, W. Weckesser, H. Abbasi, C. Gohlke, and T. E. Oliphant, “Array programming with NumPy,” *Nature*, vol. 585, p. 357–362, 2020.
- [137] D. Foreman-Mackey, A. Price-Whelan, W. Vousden, G. Ryan, M. Pitkin, V. Zabalza, Jsheyl, A. Smith, G. Ashton, M. Smith, E. Rice, B. J. Brewer, B. Sipőcz, D. W. Hogg, E. Gentry, H. Rein, H. Madan, I. Czekala, J. Tocknell, K. Barbary, R. Prechelt, S. Hoyer, T. A. Caswell, W. Kerzendorf, and K. Cruz, “dfm/corner.py: corner.py v2.1.0.rc1,” Jul. 2020.
- [138] P. T. Inc. (2015) Collaborative data science. Montreal, QC. [Online]. Available: <https://plot.ly>
- Software:* pychell (45), optimize<sup>1</sup>, Matplotlib (135), SciPy (126), NumPy

---

<sup>1</sup><https://optimize.readthedocs.io/en/latest/>

(136), Numba (123), corner (137), plotly (138), Gadfly Matplotlib theme  
<https://gist.github.com/JonnyCBB/c464d302fefce4722fe6cf5f461114ea>, emcee, (124)



## Curriculum Vitae

Bryson Cale was born in Muscatine, Iowa, on September 24, 1993, to Jerald and Diana Cale. He graduated Valedictorian from Muscatine High School in 2012, and then Grinnell College in 2016 with his Bachelor of Arts, double majoring in physics and mathematics. In 2021, he then graduated from George Mason University with his Ph.D. in physics.